NEUTRON SCATTERING OF THE FRUSTRATED MAGNETS Ba_2YOsO_6 AND $Yb_2Ti_2O_7$

NEUTRON SCATTERING OF THE FRUSTRATED MAGNETS Ba_2YOsO_6 AND $Yb_2Ti_2O_7$

By DALINI D. MAHARAJ, H. B. SC.

A Thesis Submitted to the School of Graduate Studies in Partial Fulfilment of the Requirements for the Degree Master of Science

McMaster University MASTER OF SCIENCE (2014) Hamilton, Ontario (Physics and Astronomy)
TITLE: Neutron Scattering of the Frustrated Magnets Ba_2YOsO_6 and $Yb_2Ti_2O_7$
AUTHOR: Dalini D. Maharaj, H.B.Sc. (University of Toronto)
SUPERVISOR: Professor Bruce D. Gaulin
NUMBER OF PAGES: ix, 108

Abstract

First we shall consider the rare-earth titanate $Yb_2Ti_2O_7$ which has been extensively studied within the past two decades but is still not very well understood. There has been much debate over the nature of the magnetic ground state of this system with studies reporting the development of long-range order below 250mK to the absence of long-range order below 250mK. One culprit suspected of generating these differences in behaviour of the ground state is the effect of crystal growth on sample quality. In order to address this discrepancy, measurements of the crystal-field levels of $Yb_2Ti_2O_7$ were conducted on two powder samples of different composition since the exact ground state selection depends on size and anisotropy of the magnetic moment. The second focus of this thesis concerns the family of rock-salt ordered double perovskites of the form Ba_2YXO_6 in which X is either a 4d or 5d magnetic ion. The interplay between the strong spin orbit coupling expected for such heavy magnetic ions and frustration has been theoretically predicted to exhibit a variety of exotic phenomena. Neutron scattering is utilized to investigate the low temperature dynamics of the system Ba_2YOsO_6, to compare with that observed in the 4d analog, Ba_2YRuO_6.

Acknowledgements

During the course of my studies at McMaster University, I have been fortunate to work with many talented scientists. The work presented in this thesis would not have been made possible without their contributions. Above all, I would like to thank my supervisor, Dr. Bruce Gaulin who has provided me with the numerous opportunities which I have been presented with during my studies at McMaster. It has been exciting to be a part of Bruce's group as I have been exposed to a variety fascinating projects. Being a part of his group has been a pleasure and I am grateful for the guidance he has given me during the course of my degree.

As many of our experiments are conducted at neutron scattering facilities, the support provided by the instrument scientists is invaluable. I would like to thank Garrett Granroth, Sasha Kolesnikov, Matthew Stone and Lisa DeBeer-Schmitt for their help and insight during the experiments which were conducted at SEQUOIA, at the Spallation Neutron Source. Neutron scattering measurements which were conducted at the N5 spectrometer at the Canadian Neutron Beam Centre were performed with the help of Zahra Yamani.

I would also like to thank my colleagues in the Department of Physics and Astronomy at McMaster University. It has been a great pleasure to work with and exchange ideas with my colleagues, Edwin Kermarrec, Jonathan Gaudet, Jerod Wagman, Casey Marjerrison and Connor Buhariwalla.

I would like to thank Zachary Vernon, who has always provided his support and friendship. Last but not least, I would like to express gratitude to my family and in particular, my parents. This would not have been possible without your continued love, support and encouragement.

Co-Authorship

The work presented in Chapter 4 and Chapter 5 of this thesis have been part of collaborative research efforts. These studies were done under the guidance of my supervisor, B.D. Gaulin. Here, I will outline key collaborators and their contributions.

The inelastic neutron scattering measurements which are presented in Chapter 5 were conducted on two powder samples, $Yb_2Ti_2O_7$ and $Yb_2Ti_{2-x}Yb_xO_{7-\frac{x}{2}}$ (x=0.046). The sample preparation and characterization of these materials were done by K.A. Ross. The inelastic neutron scattering measurements which were performed at SEQUOIA at the Spallation Neutron Source (SNS) at Oak Ridge National Laboratory (ORNL) on these materials were done by myself and E. Kermarrec. A.I. Kolesnikov, G.E. Granroth, L. DeBeer-Schmitt, and A.T. Savici provided instrument support. The crystal-field calculations which are presented in this thesis were performed by J. Gaudet.

The elastic and inelastic neutron scattering studies which are presented in Chapter 5 on Ba_2YOsO_6 were submitted as part of a publication involving a number of collaborators. The elastic neutron scattering measurements performed at the N5 spectrometer were conducted by myself. The inelastic neutron scattering measurements reported here were conducted by myself and E. Kermarrec. The sample preparation and characterization were done by the J.E. Greedan group at the McMaster University. This group includes key contributors, C.A. Marjerrison and C.M. Thompson. The ^{89}Y NMR measurements were conducted by S. Kroeker and colleagues at the University of Manitoba. The inelastic neutron scattering measurements were performed at SEQUOIA, at the SNS at ORNL. Instrument support was provided by L. DeBeer-Schmitt and A.I. Kolesnikov. The elastic neutron scattering experiments were performed at the Canadian Neutron Beam Centre at the C2 and N5 spectrometers. Instrument support was provided by R. Flacau and Z. Yamani at C2 and N5, respectively.

Contents

List of Figures

Chapter 1

Magnetism in Crystals

1.1 Introduction to Magnetism

Magnetism in materials arises due to presence of ions containing unpaired electrons, which posses magnetic moments. An electron has a characteristic angular momentum, $\hbar s$, associated with its spin degree of freedom. The **spin magnetic moment** μ_s is given by

$$\mu_s = -g\mu_B \boldsymbol{s}. \tag{1.1}$$

The quantitites μ_B and g are the **Bohr magneton** and the **g-value** respectively. Therefore the magnetic moment for a given ion is governed by its electronic configuration. In addition to the spin magnetic moment, an electron posseses an **orbital magnetic moment** which arises from the orbital motion of the electron. It is given by μ_o,

$$\mu_o = \mu_B \boldsymbol{l}, \tag{1.2}$$

where $\mathbf{l}$ is the angular momentum divided by $\hbar$. Practically, crystalline systems and the collective behaviour among their constituent ions are investigated. The behaviour these systems are governed by the nature of the interactions. The following sections seek to systematically develop a description of these many-body systems by first addressing single-ion properties, interactions between ions and finally quantifying the collective

behaviour in these systems through the concept of the order parameter from statistical mechanics. With this foundation, frustration and novel properties of the systems investigated shall be discussed.

1.1.1 Ground State of Free Magnetic Ion

Friedrich Hund developed a set of rules, Hund's rules, which provide a framework within which to determine the single-ion properties and in particular the combination of angular momentum quantum numbers which ensure that the minimum energy configuration of electrons in the atom is adopted. They are manifested in three major principles and are listed in order of priority.

1. The electronic wavefunction should be arranged so as to maximize S since the Pauli exclusion principle dictates that electrons with parallel aligned spins are not in the sample place. This tends to minimize the Coloumb repulsion between electrons.

2. L should be maximized. This ensures the minimization of Coulomb repulsion and is based on the premise that electrons orbiting in the same direction are less likely to meet.

3. The third rules dictates the value of J. If the shell is less than half full then $J = |L - S|$ and if it is more than half full then $J = |L + S|$. This tends to minimize the spin-orbit energy.

The values of L, S and J can be utilized to evalute the effective magnetic moment of the individual free-ion $\mu_{eff} = g_J \mu_B \sqrt{J(J+1)}$ with g_J being the Landé g-factor given by $g_J = \frac{3}{2} + \frac{S(S+1)-L(L+1)}{2J(J+1)}$. It is important to keep in mind however that there are effects such as the crystal electric field (CEF) effects which tend to dominate the spin-orbit energy leading to a violation of Hund's third rule. This is realized in a particular material studied in this thesis Ba_2YOsO_6. Here, the strong crystal-field effects tend to split the degeneracy of the 5d orbitals of the Os^{5+} ion. This shall be considered in further detail in Chapter 2. We shall now turn our attention to the nature of the interactions between magnetic moments.

1.1.2 Interacting Magnetic Moments

The most basic interaction between magnetic moments is the **magnetic dipolar interaction**. If we consider two magnetic moments μ_1 and μ_2 which separated by a distance $\mathbf{r}$, the energy of this interaction is given by

$$E = \frac{\boldsymbol{\mu}_0}{4\pi r^3}[\boldsymbol{\mu}_1.\boldsymbol{\mu}_2 - \frac{3}{r^2}(\boldsymbol{\mu}_1.\mathbf{r})(\boldsymbol{\mu}_2.\mathbf{r})]. \tag{1.3}$$

This energy of this interaction depends on the degree of alignment between the moments. This magnetic dipolar energy is of the order $\sim$1K, which indicates that this is not responsible for the development of long-range order (LRO) in some systems since their magnetic transitions typically occur on the scale $\sim$100K.

Next we consider the **exchange interaction**, which is typically the starting point for the description of systems which develop LRO below some critical temperature T_C. Intuitively, the origin of this interaction lies in the fundamental principle that like charges tend to repel each other, and this decreases as a function of separation. From a more theoretical standpoint one need to only consider one of the most basic problems in quantum mechanics, the two-electron problem. If two electrons are located at $\mathbf{r}_1$ and $\mathbf{r}_2$ and anti-symmetric exchange is accounted for, the wave-functions describing the system are

$$\Psi_S = \frac{1}{\sqrt{2}}[\psi_a(\boldsymbol{r_1})\psi_b(\boldsymbol{r_2}) + \psi_a(\boldsymbol{r_2})\psi_b(\boldsymbol{r_1})]\chi_S, \tag{1.4}$$

$$\Psi_T = \frac{1}{\sqrt{2}}[\psi_a(\boldsymbol{r_1})\psi_b(\boldsymbol{r_2}) - \psi_a(\boldsymbol{r_2})\psi_b(\boldsymbol{r_1})]\chi_T, \tag{1.5}$$

where the spatial and spin parts of the wavefunction are included. The singlet state Ψ_S refers to the electron pair aligning anti-parallel whereas the triplet state Ψ_T refers to the pair aligning parallel. If we denote E_S and E_T as the energies of these two states respectively, the difference $E_S - E_T$ is given by

$$E_S - E_T = \int [\psi \star_a (\boldsymbol{r_1})\psi \star_b (\boldsymbol{r_2})\hat{H}\psi_a(\boldsymbol{r_2})\psi_b(\boldsymbol{r_1})]d\boldsymbol{r_1}d\boldsymbol{r_2}. \tag{1.6}$$

The singlet and triplet states can be parametrized by S_1 and S_2 yielding an expression for the full Hamiltonian,

$$\hat{H} = \frac{1}{4}(E_S + 3E_T) - (E_S - E_T)\boldsymbol{S_1}.\boldsymbol{S_2}. \tag{1.7}$$

The spin dependent term can be written as given by

$$\hat{H}^{spin} = -2J\boldsymbol{S_1}.\boldsymbol{S_2}. \tag{1.8}$$

J is the **exchange integral** such that $J = \frac{E_S - E_T}{2}$. In the case $J > 0$, $E_S > E_T$ and therefore the triplet state (S = 1) is favoured. The converse is true for $J < 0$ where the singlet state is favoured. Although it is not trivial to extend this solution of the two-electron problem to a many body system, the expression for the exchange interaction can be applied analagously as the sum of the pairwise interactions between spins in the system, where i and j are the i^{th} and j^{th} spins.

$$\hat{H} = \sum_{i>j} -2J_{ij}\boldsymbol{S_i}.\boldsymbol{S_j}. \tag{1.9}$$

The sign of J dictates the relative alignment of spins, for when J>0 the interactions are antiferromagnetic as spins align anti-parallel and when J<0, the interactions are termed ferromagnetic as spins align parallel. Since this interaction involves the direct overlap of atomic orbitals of neighbouring ions, this is a form of **direct exchange**. It is derived as the expectation value of the Coulomb interaction in the ground state of the localized electron system.

There is a similar effect which occurs in ionic solids and is termed **superexchange**. It is a second-order process and does not involve the direct overlap of orbitals of magnetic ions. Instead, the interactions between two non-neighbouring magnetic ions are mediated by non-magnetic ions which separate them. Superexchange tends to typically favour anti-ferromagnetic interactions, though ferromagnetism can be realized.

Indirect exchange can also occur in metals. Electrons within the conduction band are responsible for mediation of the interactions between magnetic ions in metals. A localized magnetic moment can spin-polarize these conduction electrons and

the resulting polarization, in turn, couples to another localized magnetic moment a distance **R** away. This type of interactions is referred to as the **RKKY interaction** or **itinerant exchange**, J_{RKKY}. **Double exchange** is another exchange mechanism which we shall not emphasize, but it is realized in materials with magnetic moments which show mixed valency. More details can be found in books by Yosida [1] and Blundell [2].

We now turn our attention to an interaction which is referred to as the **Dzyaloshinsky-Moriya interaction** or **DM interaction**, H_{DM}. It is the interaction between the excited state of one magnetic ion and the ground state of another magnetic ion with orbital and spin degrees of freedom given by (L_1, S_1) and (L_2, S_2), respectively. It is sizeable in systems for which spin-orbit effects are important since spin-orbit coupling is the mechanism driving the excited state. Since spin-orbit effects scale as $\sim Z^4$, where Z represents the atomic number of the magnetic ion, it is important in systems which contain heavy magnetic ions. Therefore, double perovskites containing 4d and 5d magnetic ions are examples of crystal in which this interaction is important. The form of the DM interaction, H_{DM}, is given in the following expression

$$H_{DM} = D \cdot (\boldsymbol{S_1} \times \boldsymbol{S_2}). \tag{1.10}$$

The vector **D** depends on the crystalline structure and in general, does not vanish. Closer inspection reveals that H_{DM} vanishes when the crystal field surrounding the magnetic ion has inversion symmetry with respect to the centre between the two magnetic ions.

1.2 Phase Transitions, Criticality and Universality

Crystals are comprised of a very large number of particles, N in which $N \sim 10^{23}$. In the previous section, pairwise interactions between nearest neighbouring magnetic ions were considered. However, in order to describe bulk properties of crystals, we must use an appropriate method to describe the behaviour of a large number of particles. In principle, one can proceed to write down an N-particle Schrödinger equation involving a large number of variables ($\sim 10^{23}$) as the time evolution of the state of each particle would need to be accounted for. It is impossible to compute a solution to this many body problem. Despite this however, a different approach can be taken which relies on probability statistics to describe these many body systems. This is the basis of statistical mechanics and its strength lies in its ability to predict values for observables of many body systems (e.g. specific heat, magnetic susceptibility) based on a few macroscopic properties (e.g. volume, pressure, temperature).

Here, a review of some basic concepts of equilibrium statistical mechanics is provided. We will assume that the state of a many body system can be described by a few macroscopic properties $(\zeta_1, ...\zeta_j)$. The number of states accessible to the system or microstates, $\Omega(\zeta_1, ...\zeta_j)$, depends on these macroscopic quantities. After a very long period of time, the system is assumed to be in equilibrium and has explored all accessible microstates. When a measurement of an observable quantity, G_{obs}, is performed, and denoting the probability or fraction of time spent in ν as P_ν, G_{obs} is given by

$$G_{obs} = \sum_\nu P_\nu G_{nu}. \tag{1.11}$$

At thermodynamic equilibrium however, it is assumed that the likelihood of the system being in a particular microstate ν is equally likely. Therefore, the probability of the system to be in a particular microstate is given by

$$P_\nu = \frac{1}{\Omega(\zeta_1, ...\zeta_j)}. \tag{1.12}$$

A definition for the entropy S and free energy F of the system in full thermodynamic equilibrium with internal energy E and temperature T are given by

$$S = k_B \ln \Omega, \tag{1.13}$$

$$F = E - TS. \tag{1.14}$$

It is from the entropy and free energy that values for bulk properties of the many body system can be determined and phase transitions can be characterized. We shall now consider transitions to ordered states in magnetic spin systems. Before proceeding, we shall first make a distinction between first and second order phase transitions. If there is a discontinuity in the first (second) derivative of the free energy, this transition is characterized as a first (second) order phase transition. We shall focus the discussion on second order magnetic phase transitions.

At thermodynamic equilibrium, a temperature, T, can be defined for a spin system. In spin systems, a cooperative effect known as **spontaneous magnetization** can be observed in the absence of an externally applied magnetic field. This occurs at a low enough temperature T, such that the corresponding energy scale $\sim k_B T$ is smaller than the energy scale of magnetic interactions of the spin system. That is, magnetic interactions dominate thermal fluctuations. The transition occurs below a critical temperature T_C or equivalently, Néel temperature, T_N, in the case of a spin-system which hosts anti-ferromagnetic exchange[1]. In this regime, a magnetic moment can influence the alignment of spins that are separated from the given spin by a macroscopic distance. To quantify this, a quantity known as the coherence length ζ is employed. In this case, we say that the spin system develops long-range order (LRO) below T_C (or T_N) and the coherence length is on a macroscopic length scale. Above the critical temperature, the coherence length is much smaller and the spin system is referred to as being in the **paramagnetic** phase. This is an example of a magnetic phase transition. In general, phase transitions occur due to the breaking of symmetries of the Hamiltonian describing the system. In the case of a system of spins which are in the paramagnetic phase ($T > T_C$), the spins can freely point in any direction, independent of the influence of the neighbouring spins. As the temperature falls below the critical temperature $T < T_C$, the full rotational symmetry of the spin-direction is reduced such

[1]For the remainder of the discussion, T_C is used to denote the transition temperature in general.

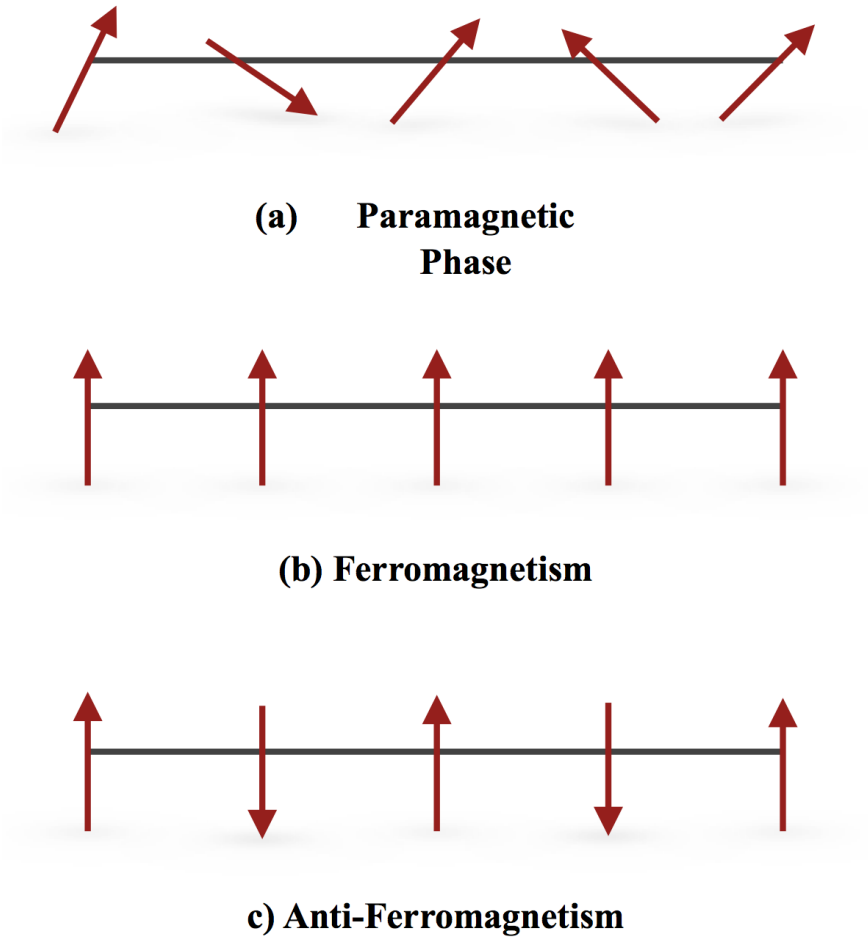

Figure 1.1: (a) Representation of disordered spins in the paramagnetic phase when $T > T_C$. (b) Representation of a ferromagnetic spin system ($T < T_C$). (c) Representation of an anti-ferromagnetic spin system ($T < T_C$).

that the spins develop an ordered spatial configuration. In order to quantify phase transitions in statistical mechanics, a quantity referred to as the **order parameter**, ψ, can be constructed with the following property

$$\begin{cases} \psi(T) = 0 \text{ if } T > T_C, \\ \psi(T) \neq 0 \text{ if } T < T_C. \end{cases} \tag{1.15}$$

Landau introduced the elegant concept of the order parameter for second order phase transitions in 1937 [3] in order to quantify spontaneous transitions of matter

in nature. Microscopically, the order parameter is related to the expectation value of a quantum operator. In the case of a 1D ferromagnet, ψ is represented by the magnetization which is defined by $m = \langle \sigma_z \rangle$ where σ. The order parameter here is the magnetization, m. It vanishes above T_C since the spins can point in any direction as depicted in Figure 1.1 (a). On the other hand, it is non-zero below the critical temperature since the spin system develops LRO and spins align along a common axis $\hat{z}$ as shown in Figure 1.1 (b). One interesting feature of phase transitions is universality. To explain this, we shall consider the ferromagnet in $d = 1, 2, 3$ dimensions. The magnetization m can be expressed as a function of temperature using the general form,

$$m \propto (T_C - T)^{\beta}. \tag{1.16}$$

β is referred to as a critical exponent and depends on the dimensionality of the system. d-dimensional spin systems tend to exhibit similar critical exponents, β, independent of the exact microscopic details of each system.

The notion that two different physical systems share the same critical exponents is termed **universality**. Universality is based on the following three major premises [4–6]. For a continuous phase transition the value of the critical exponent, β, depends on:

1. The dimensionality of the system d.
2. The dimensionality of the order parameter or the symmetry of the order parameter.
3. The range of the forces, whether the are short or long ranged.

In chapter 5 the topic of critical phenomena shall be revisited in relation to the rock-salt ordered double perovskite Ba_2YOsO_6. Now we shall consider the notion of frustration which tends to suppress ordering in magnetic systems.

1.3 Frustration

Frustration refers to the inability for a system to minimize its total classical energy by minimizing the energy of each pairwise interaction between interacting degrees of freedom [7]. The ground state of such a system is degenerate and no order is predicted in such systems down to T =0K. This however violates the third law of thermodynamics and the eventually the system must select a ground state. In this case, weaker interactions and defects tend to force the system to enter a unique state.

There are two basic classes of frustrated magnetic systems, geometric and random frustration. The former is generated by the geometry of the crystalline lattice which places constraints on the spin system, preventing the minimization of pairwise interactions between spins. A popular example of this situation is realized in the two dimensional triangular lattice with Ising spins with anti-ferromagnetic exchange interactions. In fact, one of the pioneering works in frustrated magnetism was in 1950 [8] in which frustration in the two dimensional triangular and honeycomb Ising nets were studied. Random frustration can be induced by two factors. The first emanates from competing interactions among the degrees of freedom in full thermodynamic equilibrium. The basic idea is that in such systems, one interaction does not govern the characteristic length scale of the system. In this case, the system resolves this underlying frustrationg by developing non-trivial spatial correlations, such as modulated structures [9]. A second form of random frustration arises when the randomness is quenched or *frozen in*. One key point to note is that the degrees of freedom which are frozen are not related by translational invariance. This form of frustration can be realized in systems for which impurity nonmagnetic ions sit on magnetic sites and induce the effect of disorder into the system, for example. This concept is deliberately utilized by experimentalists in the growth of crystals in order to investigate the phenomenon of disorder in frustrated systems [10]. In order to measure the degree of frustration in magnetic systems is the **frustration index, f**. It is defined by

$$f = \frac{|\Theta_{CW}|}{T^*}. \tag{1.17}$$

where Θ_{CW} is the Curie-Weiss temperature defined from the high temperature paramagnetic response of the system and T^* is the critical temperature. The systems

which are presented in this thesis are both geometrically frustrated. We shall therefore develop this concept further and consider how it is manifested in these lattices. Geometric frustration can be defined more rigorously for general lattices by considering the most basic unit of the lattice and its n faces referred to as *plaquettes*. Using the definition of the direct exchange interaction developed in the previous section and the definition of Toulouse [11], the plaquette is frustrated if the quantity P, given by

$$P = \prod_{\langle i,j \rangle} sign(J_{i,j}), \tag{1.18}$$

is negative. The product P is performed over all the $J_{i,j}$ on the plaquette. Examples of frustrated lattices are shown in Figure 1.2. The two illustrations correspond to the two-dimensional triangular lattice with Ising-like spins with anti-ferromagnetic exchange and the two-dimensional square lattice with three ferromagnetic exchanges and one anti-ferromagnetic exchange. The ground state of the former system is threefold degenerate while ground state of the square lattice is sixfold degenerate, not including the degeneracy associated with spin-flip. In real crystal systems, virtually infinite two and three-dimensional analogues of these lattices are realized, producing virtually infinite ground state degeneracy. Weaker interactions and defects for example, tend to stabilize a unique ground state out of the numerous possibilities. As a result frustrated magnetism has been an enticing field of research for the realization of many exotic states of matter such as spin glasses, classical spin-ices and quantum spin liquid phases.

One compound which is presented in this thesis is the quantum spin liquid candidate, $Yb_2Ti_2O_7$. Frustration is generated in this compound due to the arrangement of magnetic Yb^{3+} ions on a lattice of corner sharing tetrahedra as seen in Figure 1.3. The second compound studied in this thesis, Ba_2YOsO_6, belongs to family of rock-salt ordered double perovskites. The magnetic Os^{5+} ions decorate a face-centered cubic lattice (FCC) as shown in Figure 1.4. Of physical interest in this system is the effect of strong spin-orbit coupling induced due to the heavy 5d ion Os^{5+} and frustration in the selection of a unique ordered ground state. Chapter 2 shall address these two studies in further details.

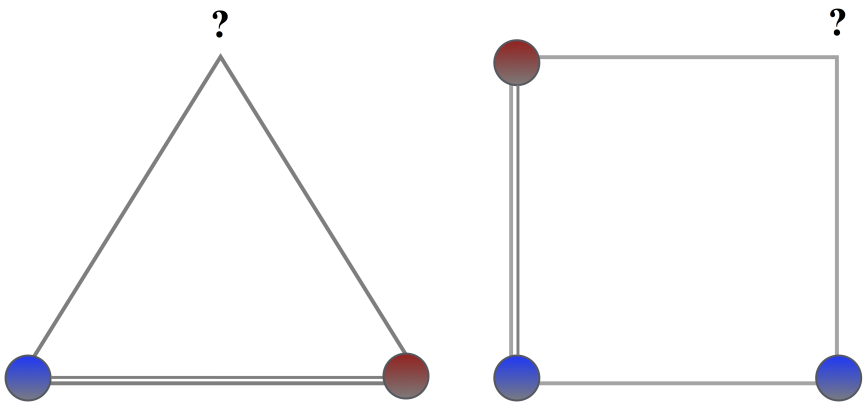

Figure 1.2: Representation of the frustrated triangular (left) and the frustrated square lattice (right). The red dots represent $\langle\uparrow|$ and blue dots represent $\langle\downarrow|$. The double gray bar represents $J > 0$ and single-bars represent $J < 0$. Adapted from Diep [7].

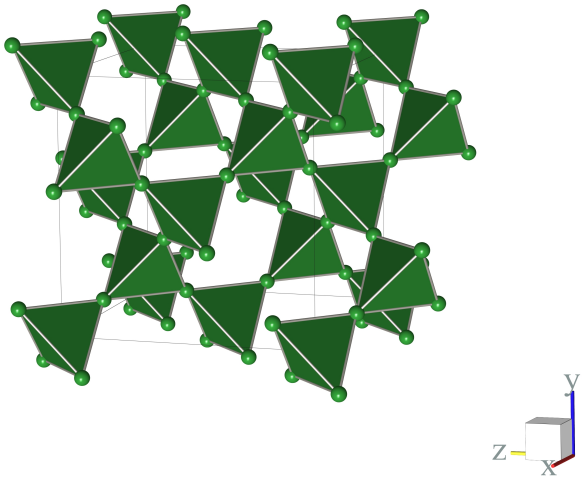

Figure 1.3: Representation of the frustrated network of corner sharing tetrahedra as realized in the rare-earth pyrochlore titanates.

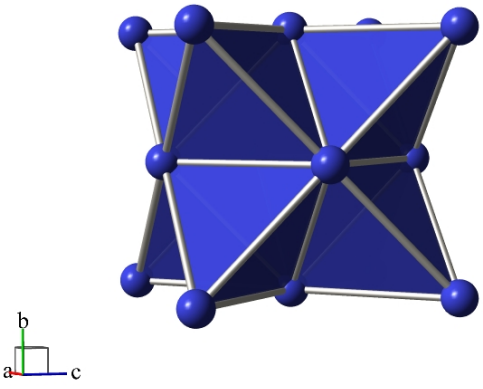

Figure 1.4: Representation of the frustrated fcc lattice as it occurs in Ba_2YOsO_6.

Bibliography

[1] K. Yosida. *Theory of Magnetism.* Springer-Verlag Berlin Heidelberg, 1996.

[2] S. Blundell. *Magnetism in Condensed Matter.* Oxford University Press Inc., 2001.

[3] L.D. Landau. *Phys. Z. Sowjun.*, 11(545), 1937.

[4] L.P Kadanoff. *Proc. 1970 Varenna Summer School on Critical Phenomena.* New York: Academic Press.

[5] R.B. Griffith. *Phys. Rev. Lett.*, 24(1479), 1970.

[6] R.B. Griffith and J.C. Wheeler. *Phys. Rev.*, A2(1047), 1970.

[7] H.T. Diep. *Frustrated Spin Systems: 2nd Edition.* World Scientific, 2013.

[8] G.H. Wannier. *Phys. Rev.*, 79(357), 1950.

[9] J.S. Gardner, M.J.P. Gingras, and J.E. Greedan. *Rev. Mod. Phys.*, 82(53), 2010.

[10] J.A. Quilliam, S. Meng, H.A. Craig, L.R. Corruccini, G. Balakrishnan, O.A. Petrenko, A. Gomez, S.W. Kycia, M.J.P. Gingras, and J.B. Kycia. *Phys. Rev. B*, 87(174421), 2013.

[11] G. Toulouse. *Commun. Phys.*, 2(115), 1977.

Chapter 2

Introduction to Crystal Systems Investigated

2.1 Quantum Spin-Ice Candidate $Yb_2Ti_2O_7$

This chapter is intended to highlight the importance of the study of crystal-field effects in $Yb_2Ti_2O_7$. In particular, background on the crystal structure and crystal-field effects in $Yb_2Ti_2O_7$ are provided. In addition, motivation for the study of the effects of sample variations on the low temperature behaviour of $Yb_2Ti_2O_7$ is provided.

2.1.1 The Rare-Earth Titanates

$Yb_2Ti_2O_7$ is a member of the family of rare-earth pyrochlore titanates (space group $Fd\bar{3}m$) of the form $A_2B_2O_6O'$. The A-site is occupied by a trivalent rare-earth ion while the non-magnetic Ti^{4+} ion is located on the B-site. A hallmark feature of the pyrochlore lattice is the network of edge-sharing tetrahedra created indepedently by A-site and B-site cations (see Figure 2.1). The network of magnetic rare-earth ions forces a geometric constraint, leaving the magnetic spin system frustrated. As mentioned previously, such a system is not expected to order down to absolute zero. However, defects and corrections to the isotropic nearest-neighbour exchange Hamiltonian such as, Dzyaloshinskii-Moriya exchange interactions enable the system the enter an ordered state. Therefore, it is of interest to investigate the exotic states which are stabilized due to the interplay of these effects. The ability for the pyrochlore titanate structure to host an array of rare-earth ions (from Sm to Lu) provides an interesting vehicle to

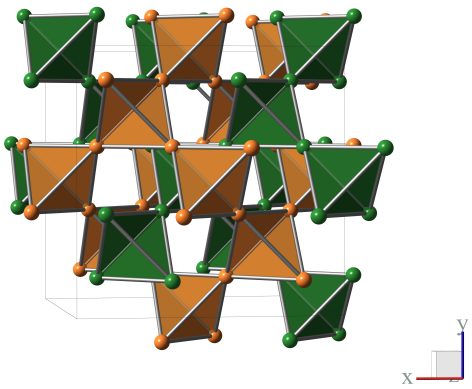

Figure 2.1: The network of corner sharing tetrahedra generated by the Yb^{3+} and Ti^{4+} ions respectively in the pyrochlore lattice.

realize a variety of phenomena since the nature of both dominant and weak magnetic interactions is different in each case [1]. As a result, there has been a great deal of attention given to the systematic study of the low temperature properties of these compounds.

2.1.2 Crystal-Field Effects in $Yb_2Ti_2O_7$

Yb^{3+} has an electronic configuration of $[Xe]4f^{13}$. In case of Yb^{3+} in $Yb_2Ti_2O_7$, the degree of splitting of the electronic levels produced by crystal fields is less than those produced by spin-orbit coupling [2]. This is a consequence of the relatively short spatial range of the 4f electrons around the Yb^{3+} ion. Therefore proper treatment of this problem involves accounting for the effect of the spin-orbit interaction prior to consideration of the crystal-field effect. Hence in accordance with Hund's rules the ground state can be described by ${}^2F_{\frac{7}{2}}$ (see Blundell [3] for notation).

The nature of the anisotropy of each rare-earth ion within the $A_2Ti_2O_7$ structure is one of the key ingredients which dictate the nature of the low temperature phenomena observed in these materials [4]. For example, $Yb_2Ti_2O_7$ shows different low temperature behaviour from $Ho_2Ti_2O_7$ and $Dy_2Ti_2O_7$ which are both classical spin-ices and have easy-axis anisotropy associated with the rare-earth ions [1]. On the other hand, Yb^{3+} spins have been shown to foster ferromagnetic exchange coupling [5–7] and the magnetic moments have easy-plane or XY anisotropy perpendicular to the [111] direction [8]. The exact nature of the anisotropy of the magnetic moments is determined by the crystal-field effects of the crystalline environment surrounding the A^{3+} ions. It is therefore important to conduct crystal-field investigations of $Yb_2Ti_2O_7$ in order to accurately determine the size and anisotropy of the ground state magnetic moment as well as the ground state wave function. This investigation is timely, since the nature of the low temperature behaviour of $Yb_2Ti_2O_7$ is debated (see Section 2.1.3 for more details). To begin with, a theoretical description of the crystal-field effects on the A^{3+} site in the rare-earth titanate structure will be introduced in general. This serves to familiarize the reader with important concepts involved in the description of crystal-field effects and to highlight the necessity of direct measurements of the crystal-field splittings in extracting all desired quantities.

The crystal field effect is treated as a small perturbation on the lowest lying multiplet which are eigenstates of $\mathbf{J}$, the total angular momentum. To obtain an expression for the perturbing potential, W_c, a point-charge approximation is utilized. This involves the evaluation of the electrostatic potential $V(r, \theta, \phi)$ due to the surrounding point charges at a point (r, θ, ϕ) near the origin at the magnetic ion. The perturbing potential, W_c is given by

$$\begin{cases} V(r,\theta,\phi) = \sum_j \dfrac{q_j}{|\boldsymbol{R_j} - \boldsymbol{r}|}, \\ W_c = \sum_i = \sum_i \sum_j \dfrac{q_i q_j}{|\boldsymbol{R_j} - \boldsymbol{r_i}|}, \end{cases} \tag{2.1}$$

where the position and charge of the ith Yb^{3+} ion are r_i and q_i respectively[1], and q_j is the charge at the jth neighbouring O^{2-} ion a distance R_j from the origin.

Once this perturbing potential is determined, one needs to calculate the respective matrix elements in the basis $|J, J_z\rangle$ and solve an eigenvalue problem since **J** is a good quantum number [9]. Tesseral harmonics[2] can be conveniently utilized to rewrite the crystalline potential energy [13]. Expressing the potential $V(r,\theta,\phi)$ as shown in Equation (2.2) is desired since a general form can be easily derived for many rare-earth ions and simplifying the calculation of matrix elements [13].

$$\begin{cases} V(r,\theta,\phi) = \sum_{n=0}^{\infty} \sum_{\alpha} r^n \gamma_{n\alpha} Z_{n\alpha}(\theta,\phi), \\ \gamma_{n\alpha} = \sum_{j=1}^{k} \dfrac{4\pi}{2n+1} q_j \dfrac{Z_{n\alpha}(\theta,\phi)}{R_j^{j+1}}. \end{cases} \tag{2.2}$$

Once the potential is expressed in terms of Tesseral harmonics, it can be written in terms of Cartesian co-ordinates which have a an immediate correspondence with Stevens' operator equivalents [2]. The number of harmonics appearing in the expansion for the potential is governed by this fact and two important consequences are the following [13].

1. If there is a centre of inversion at the ion site, there will be no odd-n terms
2. If the z-axis is an m-fold axis of symmetry the potential will contain terms Z_{nm}

In this case, the Yb^{3+} site has D_{3d} point symmetry. This symmetry arises due to the co-ordination of each Yb^{3+} ion with the eight nearest neighbouring oxygen ions (see Figure 2.2) which generate the crystal-electric field. The co-ordination geometry is dictated by the value of x for the oxygen atom in the $48f$ position [1]. In the case

[1]The sum over index i involves electrons in unfilled shells as closed shells are only affected in a higher order perturbation theory

[2]For further details on tesseral harmonics, refer to Jahnke [10], Margeneau [11] and Prather [12].

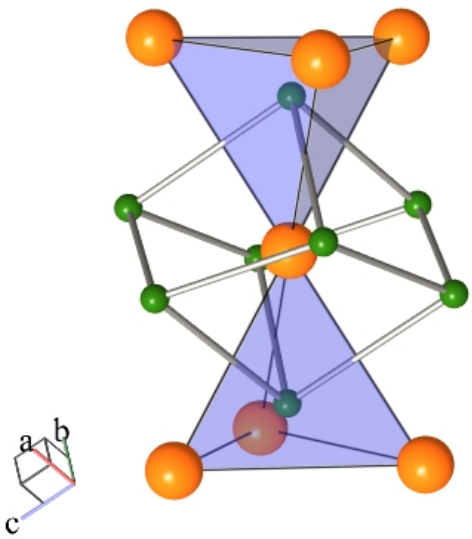

Figure 2.2: The local environment of the Yb^{3+} (in orange) at the intersection of two tetrahedra in the $Yb_2Ti_2O_7$ structure. Each Yb^{3+} is surrounded by eight O^{2-} ions (in green), forming a distorted cube.

where $x = 0.3125$, a perfect octahedron is formed and when $x = 0.375$ a perfect cube is formed. In reality, a distorted structure is realized for the rare-earth titanates and in the case of $Yb_2Ti_2O_7$, $x = 0.3309$ [14]. This produces a prominent axial symmetry about the Yb^{3+}-site, reducing the full O(3) symmetry with the unique axis being along a local $\langle 111 \rangle$ direction.

It can be shown that for a crystalline potential with D_{3d} trigonal symmetry [15, 16], the resulting crystal-field Hamiltonian $\mathcal{H}_{CF}$ can be expressed as a function of the Stevens' operators O_n^m and co-efficients D_n^m as given by

$$\mathcal{H}_{CF} = \alpha_J D_2^0 O_2^0 + \beta_J (D_4^0 O_4^0 + D_4^3 O_4^3) + \gamma_J (D_6^0 O_6^0 + D_6^3 O_6^3 + D_6^6 O_6^6). \tag{2.3}$$

The terms D_n^m are the crystal-field parameters which need to be determined and are impossible to find without experimental data which directly provide the size of the crystal-field splittings.[3] Previous attempts have been made to determine size and anisotropy of the magnetic moment and the ground state wave function through the use of Mössbauer spectroscopy [17] and optical spectroscopy [18], for example. One

[3]The crystal-field parameters D_n^m can also be expressed as B_n^m using $B_n^m = \theta_n D_n^m$ where θ_n is α_j (n=2), β_j (n=4), γ_J (n=6). For the Yb^{3+} ion in $Yb_2Ti_2O_7$, $\alpha_j = \frac{2}{3^2 \cdot 7}$, $\beta_j = -\frac{2}{3 \cdot 5 \cdot 7 \cdot 11}$ and $gamma_J = \frac{2^2}{3^2 \cdot 7 \cdot 11 \cdot 13}$.

direct way to probe the crystal-field levels is to utilize inelastic neutron scattering techniques. This is has never been done before for $Yb_2Ti_2O_7$, but has been successfully employed in other related compounds [19]. In this study, it is the technique which is employed to investigate the crystal-field excitations of the lowest lying multiplet in $Yb_2Ti_2O_7$. Up for discussion next is the effect of the crystal growth process on sample quality. This a detail which has been of concern since it is unclear how strongly the sample variability affects the low temperature behaviour of this system.

2.1.3 Stuffing in $Yb_2Ti_2O_7$

In the past decade, there have been numerous studies conducted on $Yb_2Ti_2O_7$. Independent studies report evidence for different behaviour at low temperature. Early heat capacity measurements conducted on powder samples of $Yb_2Ti_2O_7$ found evidence for the development of an ordered magnetic state below 0.2K [5]. On the other hand, a series of Mössbauer spectroscopic and muon spin relaxation (μSR) studies showed that $Yb_2Ti_2O_7$ fails to develop order in zero field [6, 8, 20]. In addition, there were a series of neutron scattering investigations which were conducted on single-crystals grown by the float-zone method. One gives evidence for a ferromagnetic transition at T_C =0.24K [21]. Other neutron scattering studies in contrast, report the existence of a disordered ground state down to 30mK with field induced order only with the application of modest fields ($\sim 0.5T$) along the $[1\bar{1}0]$ direction [22, 23].

In light of the variety of behaviour reported, attention has focussed a determination of the source of these inconsistencies which tends to push this apparent fragile ground state into different regimes. One factor which has been of concern regarding this effect is the quality of crystals grown via the optical floating zone method [24]. Powder samples tend to have a single, sharp specific heat anomaly which occur at $\sim$ 265mK [5, 23, 25, 26]. Single-crystal samples on the other hand, tend to have broad humps in specific heat which occur at lower temperatures $\sim$ 210mK [23, 26]. In general, specific heat anomalies tend to signal the occurrence of a phase transition. Since there is variation in the low temperature behaviour and specific heat results for this system, this highlights the need to investigate the effects of sample quality on the low temperature magnetic properties of this system.

To investigate whether there are structural differences between powder and single-crystal samples of $Yb_2Ti_2O_7$, a detailed neutron diffraction study on two samples was conducted in order to obtain high quality structural refinements [24]. One of

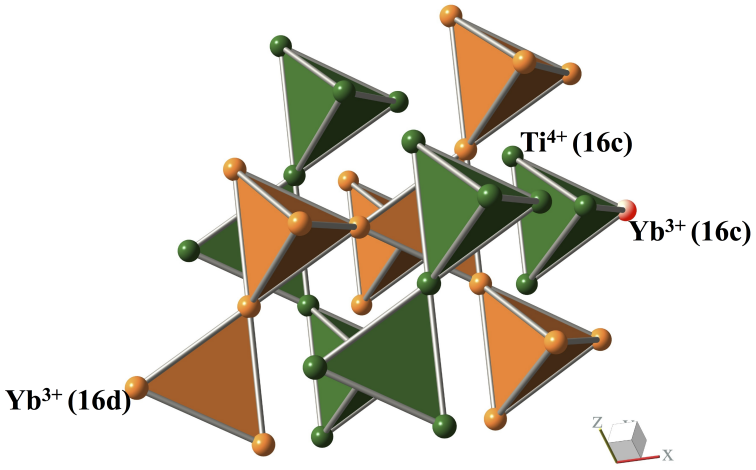

Figure 2.3: The rare-earth titanate pyrochlore structure showing only the cationic positions. The stuffed structure includes some rare-earth Yb^{3+} ions on the transition metal Ti^{+} site. The presence of the extra rare-earth ions is shown in yellow on the network of Ti^{+} tetrahedra.

the samples studied was a pulverised single-crystal and the second was a powder sample which was the starting material for the single-crystal growth. The parameter **x**, or **degree of stuffing** was introduced to summarize results from the structural refinements wherein the chemical composition of both samples were described by the formula, $Yb_2Ti_{2-x}Yb_xO_{7-\frac{x}{2}}$. Structural refinement of the powder sample yielded a perfect structure, or x =0 and in the case of the crushed single-crystal, x =0.046(4) [24]. The latter has been interpreted in terms of the presence of an excess of Yb^{3+} ions on vacant Ti^{4+} sites as depicted in Figure 2.3. This effect has been referred to as **stuffing**. Stuffing on the B-site introduces some chemical disorder into the system and magnetic exchange pathways are expected to be affected. Therefore, a comparative investigation of crystal-field excitations in both samples should reveal whether there are significant differences which affect the nature of the low temperature behaviour of this system.

2.2 The Frustrated Anti-Ferromagnet Ba_2YOsO_6

As seen in the previous section (Section 2.1), the rare-earth titanate $Yb_2Ti_2O_7$, has been extensively studied in the past decade. In general, much effort has been put into the investigation of the family of rare-earth titanates. In addition, other heavily studied frustrated systems are the kagomé lattice [27–29], hyperkagomé lattice [30, 31], triangular systems [32–35] and spinels. In contrast the family of rock-salt ordered double perovskites, Ba_2YXO_6, which host frustration on a face-centred cubic (FCC) lattice, have only been studied within recent years. The following chapter introduces general crystallographic and magnetic properties of this family of compounds. In addition, exotic phenomena exhibited by several members of this series is discussed. This seeks to provide inspiration for the study of Ba_2YOsO_6 as part of a more general, systematic study of the Ba_2YXO_6 series.

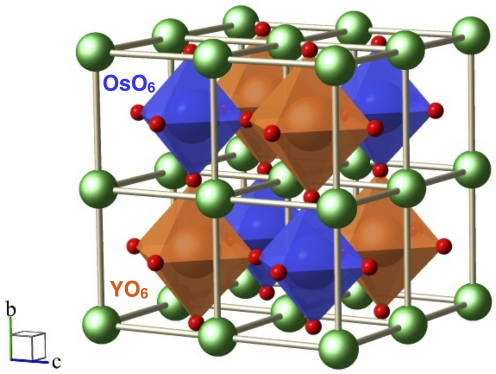

Figure 2.4: The rock-salt ordered double perovskite structure in the special case of Ba_2YXO_6. This shows the octahedral co-ordination of the Os^{5+} (in blue) and Y^{3+} ions (in orange) with surrounding O^{2-} ions (in red) with the Ba^{2+} ions in green.

Rock-salt ordered double perovskites are of the form $A_2BB'O_6$ with the A-site being occupied by a non-magnetic cation and the B-site being occupied a magnetic cation. Of particular interest in this study are systems which are described by the formula Ba_2YXO_6, with X being a magnetic ion. These compounds are highly symmetric and are described by the space group, $Fm\bar{3}m$. This is facilitated, because the octahedral holes between the BaO_3 layers are large enough to accommodate an ordered arrangement of the B and B′ cations [36]. One characteristic of the Ba_2YXO_6 compounds is the relatively low level of $\frac{B}{B'}$ inter-site mixing. For example, low levels of inter-site mixing

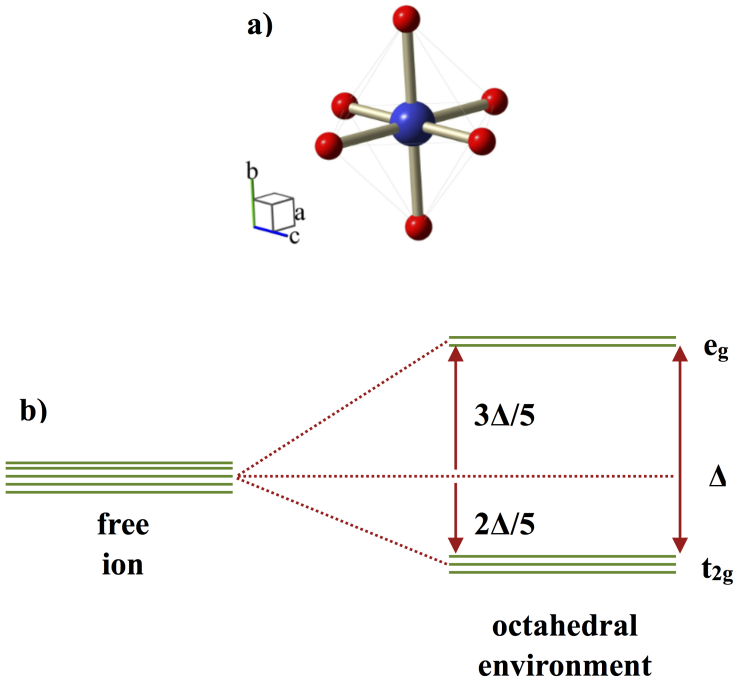

Figure 2.5: (a) The octahedral co-ordination of the magnetic ion (in blue) with the 6 nearest neighbouring oxygen atoms (in red). (b) The relative splitting of the 4d (or 5d) degenerate electronic levels into triply degenerate t_{2g} orbitals and doubly degenerate e_g orbitals. The quantity, Δ refers to the size of the energy gap.

were found to be 3%, 0.5% and 1%, in the cases where X = Ru, Mo and Re, respectively, from ^{89}Y NMR measurements [37–39]. This is a favourable characteristic of these compounds, since magnetic properties are not expected to be significantly influenced due to site disorder.

As eluded to in Chapter 1, the electronic configuration of the magnetic ion is an important starting point in the description of magnetism in materials. For now, we shall focus on the way in which the electronic levels are split in these compounds. Each magnetic ion in Ba_2YXO_6 is octahedrally co-ordinated to six oxygen ions. These generate a strong crystal-electric field, which is on the same energy scale as spin-orbit effects. Therefore the splitting of the electronic levels in the magnetic ion is determined first, by the crystal-field effects. The degenerate 4d (or 5d) electronic levels of the free-magnetic ion are split into triply degenerate t_{2g} and doubly degenerate e_g orbitals, as shown in Figure 2.5. A further description of the magnetic behaviour requires identification of the key effects at play in these systems. Though these systems are

frustrated (see Section 1.3 for more details), spin-orbit effects are dominant in the development of the exotic magnetism in these materials. As mentioned in Chapter 1, spin-orbit effects are sizeable in systems which contain heavy magnetic ions such as 4d or 5d magnetic cations.

The effect of strong spin-orbit coupling in the Ba_2YXO_6 series has already been explored by theorists, and their findings yield rich phase diagrams for these systems [40–42]. Recent experimental studies have also shown that, these compounds indeed exhibit an array of distinct ground states including spin-gapped, spin liquid, short-range ordered and spin-glass ground states [37–39, 42, 43]. The diversity of ground states realized in this series can be attributed to the fact that Ba_2YXO_6 can host a variety of 4d and 5d cations in the rock-salt structure. As a result, different scenarios are realized, from the extreme quantum case, wherein the spin-only moment is $S = \frac{1}{2}$, to the more classical cases for which $S = \frac{3}{2}$, for example [37].

There has been theoretical work on the $4d^1$ and $5d^1$ systems [42]. Such systems are $s = \frac{1}{2}$ systems and represent the extreme quantum limit. At the mean-field level, three main phases were predicted including an unusual antiferromagnet in which a quantum spin liquid phase may be favoured, a ferromagnetic phase with magnetization along the [110] direction and a non-magnetic but quadrupolar ordered phase [42]. One example of this system is Ba_2YMoO_6, which has been previously investigated [38, 43]. In the study by Aharen *et al.* [38], heat capacity, powder neutron diffraction and μSR measurements showed no evidence for the development of LRO down to 2K. In addition, ^{89}Y NMR measurements showed a remarkable local spin susceptibility behaviour with two components, one indicating a singlet state and the other a strongly fluctuating paramagnetic state. The time-of-flight inelastic neutron scattering study by Carlo *et al.*, also gave evidence for the existence of a singlet ground state [43].

A later theoretical study on $4d^2$ and $5d^2$ systems also predicted a diversity of ground states [41]. The $4d^2$ and $5d^2$ systems represent the $S = 1$ regime. In addition, there has been some experimental work performed on Ba_2YReO_6 (Re^{5+}, $5d^2$). Some studies reported evidence for spin order below 45K [39, 44, 45]. On the other hand, despite the anomalies observed in specific heat and susceptibility data, μSR and neutron diffraction studies have provided no evidence for LRO above 2K [39]. The available work on this compound reflects some intermediate behaviour between a long-range ordered anti-ferromagnetic state and a gapped singlet state.

Of interest in this work is the $5d^3$ system, Ba_2YOsO_6. This compound can be

directly compared with the 4d analogue, Ba_2YRuO_6, for which there is pre-existing experimental work [37, 46]. In the study by Carlo *et al.* [46], which reports inelastic neutron scattering measurements, an unexpectedly large gap at $\sim$5meV was observed below T_N =70K with a bandwidth of spin excitations extending up to 14meV [46]. In order to determine whether spin-orbit effects are key to the development of this large gap, a similar study on the 5d system, Ba_2YOsO_6 is key for comparison. Inelastic neutron scattering and triple-axis measurements techniques can be utilized so that a direct comparison of the low temperature behaviour in Ba_2YOsO_6 and Ba_2YRuO_6 could be made. If spin-orbit coupling is indeed the source of the unexpectedly large gap in Ba_2YOsO_6, a gap should be observed for Ba_2YOsO_6. As the spin-orbit effects are stronger in Ba_2YOsO_6 by virtue of the heavier magnetic 5d ion, any effect due to spin-orbit coupling should be enhanced. The subtleties of this problem and results are further discussed in relation to the results obtained by Carlo *et al.* [46] in Chapter 5.

Bibliography

[1] J.S. Gardner, M.J.P. Gingras, and J.E. Greedan. *Rev. Mod. Phys.*, 82(53), 2010.

[2] B. Bleaney and K.W.H. Stevens. *Rep. Prog. Phys.*, 16:108–155, 1953.

[3] S. Blundell. *Magnetism in Condensed Matter*. Oxford University Press Inc., 2001.

[4] B.C. den Hertog and M.J.P. Gingras. *Phys. Rev. Lett.*, 84(3430), 2000.

[5] H.W.J. Blöte, R.F. Wielinga, and W.J. Huiskamp. *Physica*, 43:549–568, 1968.

[6] J.A. Hodges, P. Bonville, A. Forget, M. Rams, and K. Królas. *J. Phys. Condens. Matter*, 13:9301–9310, 2001.

[7] S.T. Bramwell, M.N. Field, M.J. Harris, and I.P. Parkin. *J. Phys. Condens. Matter*, 12, 2000.

[8] J.A. Hodges, P. Bonville, A. Forget, A. Yaouanc, P. Dalmas de Réotier, G. Andre, M. Rams, K. Królas, C. Ritter, P.C.M. Gubbens, C.T. Kaiser, P.J.C King, and C. Baines. *Phys. Rev. Lett.*, 88(077204), 2002.

[9] Y.J. Kao, Enjalran M., A. Del Maestro, H.R. Molavian, and M.J.P. Gingras. *Phys. Rev. B*, 68(172407), 2003.

[10] E. Jahnke and F. Emde. *Tables of Functions*. Dover, New York, 4 edition, 1945.

[11] H. Margeneau and G.M. Murphy. *The Mathematics of Physics and Chemistry*. Van Nostrand, Princeton, New Jersey, 2 edition, 1956.

[12] J.L. Prather. *Atomic Energy Levels in Crystals*. National Bureau of Standards, 1961.

[13] M.T. Hutchings. *Solid State Physics, Advances in Research and Applications*, volume 16. 1964.

[14] L. Cai, A.L. Arias, and J.C. Nino. *J. Mater. Chem.*, 21:3611–3618, 2010.

[15] I. Mirebaeu, P. Bonville, and M. Hennion. *Phys. Rev. B*, 76(184436), 2007.

[16] M.J.P. Gingras, B.C. den Hertog, M. Faucher, J.S. Gardner, S.R. Dunsiger, L.J. Chang, B.D. Gaulin, N.P. Raju, and J.E. Greedan. *Phys. Rev. B*, 62(6496), 2000.

[17] A. Bertin, Y. Chapuis, P. Dalmas de Réotier, and Y. Yaouanc. *J. Phys.: Condens. Matter*, 24:256003, 2012.

[18] M.P. Zinkin, M.J. Harris, Z. Tun, R.A. Cowley, and B.M. Wanklyn. *J. Phys.: Condens. Matter*, 8:193–197, 1996.

[19] J. Zhang, K. Fritsch, Z. Hao, B.V. Bagheri, M.J.P. Gingras, G.E. Granroth, P. Jiramongkolchai, R.J. Cava, and B.D. Gaulin. *Phys. Rev. B*, 89(134410), 2014.

[20] A. Yaouanc, P. Dalmas de Réotier, P. Bonville, P.A. Hodges, P.C.M. Gubbens, C.T. Kaiser, and S. Sakarya. *Physica B*, 326(456-459), 2003.

[21] Y. Yasui, M. Soda, S. Iikubo, M. Ito, M. Sato, N. Hamaguchi, T. Matsushita, N. Wada, T. Takeuchi, N. Aso, and K. Kakurai. *J. Phys. Soc. Jpn.*, 72:3014–3015, 2003.

[22] K.A. Ross, J.P.C. Ruff, C.P. Adams, J.S. Gardner, H.A. Dabkowska, Y. Qiu, Copley J.R.D., and B.D. Gaulin. *Phys. Rev. Lett*, 103(227202), 2009.

[23] K.A. Ross, L.R. Yaraskavitch, M. Laver, J.S. Gardner, J.A. Quilliam, S. Meng, J.B. Kycia, Th. Proffen, H.A. Dabkowska, and B.D. Gaulin. *Phys. Rev. B*, 84(174442), 2011.

[24] K.A. Ross, Th. Proffen, H.A. Dabkowska, J.A. Quilliam, L.R. Yaraskavitch, J.B. Kycia, and B.D. Gaulin. *Phys. Rev. B*, 86(174424), 2012.

[25] P. Dalmas de Réotier, V. Glazkov, C. Marin, A. Yaouanc, P.C.M. Gubbens, S. Sakarya, P. Bonville, A. Amato, C. Baines, and P.J.C. King. *Physica B*, 374:145–147, 2006.

[26] A. Yaouanc, P. Dalmas de Réotier, C. Marin, and V. Glazkov. *Phys. Rev. B*, 84(172408), 2011.

[27] T.H. Han, J.S. Helton, S. Chu, D.G. Nocera, J.A. Rodriguez-Rivera, C. Broholm, and Y.S. Lee. *Nature*, 492(406), 2012.

[28] B. Fåk, E. Kermarrec, L. Messio, B. Bernu, C. Lhuillier, F. Bert, P. Mendels, B. Koteswararao, F. Boquet, J. Ollivier, A.D. Hillier, A. Amato, R.H. Colman, and A.S. Wills. *Phys. Rev. Lett.*, 109(037208), 2012.

[29] P. Mendels, F. Bert, M.A. de Vries, A. Olariu, A. Harrison, F. Due, J.C. Trombe, J.S. Lord, A. Amato, and C. Baines. *Phys. Rev. Lett.*, 98(077204), 2007.

[30] Y. Okamoto, M. Nohara, H. Aruga-Katori, and H. Takagi. *Phys. Rev. Lett.*, 99(137207), 2007.

[31] P. Dalmas de Réotier, A. Yaouanc, P.C.M. Gubbens, C.T. Kaiser, C. Baines, and P.J.C. King. *Phys. Rev. Lett.*, 91(16), 2003.

[32] M. Mourigal, W.T. Fuhrman, J.P. Scheckelton, A. Wartelle, J.A. Rodriguez-Rivera, D.L. Abernathy, T.M. McQueen, and C.L. Broholm. *Phys. Rev. Lett.*, 112(027202), 2014.

[33] A. Olariu, P. Mendels, F. Bert, B.G. Ueland, P. Schiffer, R.F. Berger, and R.J. Cava. *Phys. Rev. Lett.*, 97(167203), 2006.

[34] Y. Shimizu, K. Miyagawa, K. Kanoda, M. Maesato, and G. Saito. *Phys. Rev. Lett.*, 91(10), 2003.

[35] Y. Shimizu, H. Akimoto, H. Tsujii, A. Tajima, and R. Kato. *Phys. Rev. Lett.*, 99(256403), 2007.

[36] P.D. Battle and C.W. Jones. *J. Solid State Chem.*, 78:108–116, 1989.

[37] T. Aharen, J.E. Greedan, F. Ning, T. Imai, V.K. Michaelis, S. Kroeker, H. Zhou, C.R. Wiebe, and L.M.D. Cranswick. *Phys. Rev. B*, 80(134423), 2009.

[38] T. Aharen, J.E. Greedan, C.A Bridges, A.A. Aczel, J. Rodriguez, G. MacDougall, G.M. Luke, T. Imai, V.K. Michaelis, S. Kroeker, H. Zhou, C.R. Wiebe, and L.M.D. Cranswick. *Phys. Rev. B*, 81(224409), 2010.

[39] T. Aharen, J.E. Greedan, C.A Bridges, A.A. Aczel, J. Rodriguez, G. MacDougall, G.M. Luke, V.K. Michaelis, S. Kroeker, C.R. Wiebe, H. Zhou, and L.M.D. Cranswick. *Phys. Rev. B*, 81(064436), 2010.

[40] G. Chen and L. Balents. *Phys. Rev. B*, 78(094403), 2008.

[41] G. Chen and L. Balents. *Phys. Rev. B*, 84(094420), 2011.

[42] G. Chen, R. Pereira, and L. Balents. *Phys. Rev. B*, 82(174440), 2010.

[43] J.P. Carlo, J.P. Clancy, T. Aharen, Z. Yamani, J.P.C Ruff, J.J. Wagman, G.J. Van Gastel, H.M.L. Noad, G.E. Granroth, H.A. Dabkowska, and B.D. Gaulin. *Phys. Rev. B*, 84(100404), 2011.

[44] P. Schiffer and A.P. Ramirez. *Commun. Condens. Matter Phys.*, 10:21, 1996.

[45] Y. Sakaski, Y. Doi, and Y. Hinatsu. *J. Mater. Chem.*, 12:2361–2366, 2002.

[46] J.P. Carlo, J.P. Clancy, K. Fritsch, C.A. Marjerrison, G.E. Granroth, J.E. Greedan, H.A. Dabkowska, and B.D. Gaulin. *Phys. Rev. B*, 88(024418), 2013.

Chapter 3

Introduction to Neutron Scattering

Neutron scattering has been successfully applied to many fields of scientific research. Clifford Shull and Bertram Brockhouse were jointly awarded the Nobel Prize in physics in 1994, for pioneering contributions to the development of neutron scattering techniques of condensed matter. In particular, Shull developed the neutron diffraction technique while Brockhouse developed neutron spectroscopy.

Since then, there has been significant development of instrumentation and new techniques, such as time-of-flight neutron scattering. As a result, our ability to probe different length and energy scales has broadened, permitting the investigation of a great deal of phenomena. Most recent advances in neutron scattering technology permit the investigation of quantum phase transitions, critical behaviour and magnetic ordering in systems, as well as structural hierarchy and diffusive properties in biological membranes. This chapter is intended to give a brief introduction to the theory of neutron scattering. In addition, it provides insight into the suitability of employing time-of-flight and triple-axis techniques, in the investigation of the phenomena of interest. As this is intended as a concise introduction, further details and discussion can be found in the following texts by Shirane [1], Squires [2] and Collins [3].

3.1 Properties of Neutrons

The neutron was first discovered in 1932 by James Chadwick, who was consequently awarded the Nobel Prize in Physics in 1935. Some basic properties of neutrons are given in Table 3.1. Four years following its discovery, it was demonstrated that neutrons could be Bragg diffracted by solids [4]. Neutrons are produced at reactors and spallation neutron sources via fission or spallation of heavy nuclei. At these large neutron sources, neutrons are utilized in scattering experiments in the investigation structural and dynamic properties of materials.

Some properties, which make neutron scattering a powerful probe in the investigation of magnetism in condensed matter materials are summarized in the following points. The energy of thermal neutrons[1] are between $1 - 100$meV, the energy scale of many dynamical phenomena in condensed matter systems. Another factor which makes neutron scattering a powerful probe of magnetism is that neutrons have a **magnetic dipole moment**, μ_n. It is expressed in terms of γ, the gyromagnetic ratio, μ_N, the nuclear magneton and σ, the Pauli spin operator as given by

$$\mu_n = -\gamma \mu_N \sigma. \tag{3.1}$$

This moment can interact with unpaired electrons in magnetic atoms. The scattering of a neutron from nuclei from a sample is isotropic in nature and can be characterized by a single quantity termed the **scattering length**, b. This quantity is typically on the order $\sim 1 \times 10^{-12}$ cm. For thermal neutrons, the scattering length depends on the isotope of the element and the spin associated with the the nucleus. Unlike X-Ray scattering, there is no systematic Z-dependence of the coherent scattering length.

As the strength of the nuclear interaction is on the order of the magnetic interaction, a full description of neutron scattering relies on a description of both nuclear and magnetic contributions to scattering.

[1] Thermal neutrons are those coming from a moderator near room temperature.

Table 3.1: Basic properties of neutrons.

Quantity	Value
Rest Mass, m	1.675×10^{-27}kg
Spin	$\frac{1}{2}$
Charge	0
Magnetic Moment	$1.913\mu_{\mathrm{N}}$

3.2 Theory of Neutron Scattering

3.2.1 Definition of the Scattering Cross-Section

For a typical neutron scattering experiment, we shall consider the following parameters. The neutron beam has neutrons all characterized by energy E, incident on a target sample with incident wavevector, $\mathbf{k}$ (see Figure 3.1). After interacting with the sample, the neutrons are now characterized by a final energy $E' + dE'$ and momentum $\mathbf{k}'$. In general, the quantity which is regularly measured in such an experiment is the cross-section. We are interested in the quantity the **partial differential cross-section** which is defined as

$\frac{d^2\sigma}{d\Omega\, dE'}$ = (number of neutrons scattered per second into a small solid angle $d\Omega$ in the direction θ, ϕ with final energy between E' and $E' + dE'$) /($\Phi \cdot \mathrm{d}\Omega \cdot \mathrm{dE}'$).

Here, Φ is the flux of the incident neutrons or number of neutrons through unit area per second with the area being perpendicular to the direction of the neutron beam. The partial differential cross-section is comprised of two terms namely, the **coherent partial differential cross-section**, $\frac{d^2\sigma}{d\Omega\, dE'}\,|_{coh}$ and the **incoherent partial differential cross-section**, $\frac{d^2\sigma}{d\Omega\, dE'}\,|_{inc}$ as given by

$$\frac{d^2\sigma}{d\Omega\, dE'} = \frac{d^2\sigma}{d\Omega\, dE'}\,|_{coh} + \frac{d^2\sigma}{d\Omega\, dE'}\,|_{inc}\ . \tag{3.2}$$

The first term is associated with co-operative effects among different atoms such as elastic Bragg scattering and inelastic scattering by magnons and phonons. The incoherent term is related to the time correlation of an atom with itself and provides information on individual particle motion such as diffusion.

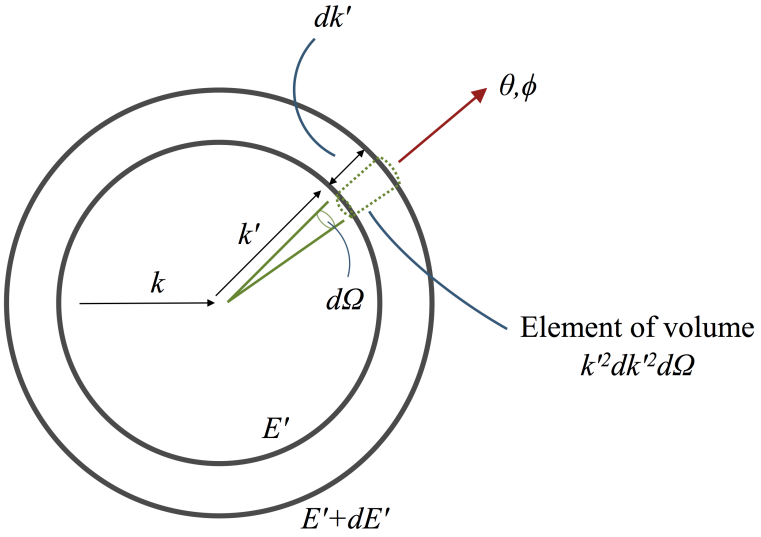

Figure 3.1: Pictoral representation of the differential scattering cross-section, $\frac{d\sigma}{d\Omega}$. Adapted from Squires [2]. The neutron beam is scattered by a small target into solid angle $d\Omega$ and is characterized by initial and final momenta, $\mathbf{k}$ and $\mathbf{k}'$. The spheres shown correspond to neutron energies E' and $E' + dE'$.

3.2.2 Nuclear Scattering

We shall now focus our attention to nuclear scattering by a general system of particles. For this problem, N scattering centres are considered and the origin is set at some arbitrary point in the scattering system. $\mathbf{R}_j$, $j = 1, 2...N$ refers to the location of the j^{th} nucleus and $\mathbf{r}$ denotes the location of the neutron. To develop an expression for the partial differential cross-section, Fermi's Golden Rule is employed since it relates the probability of a transition occurring from an initial state λ to a final state λ' in the scattering system when there is an interaction potential V between the neutron and surrounding N nuclei. This potential is given by,

$$\begin{cases} V = \sum_j V_j\,(\mathbf{r} - \mathbf{R}_j\,), \\ \boldsymbol{x}_j = \mathbf{r} - \mathbf{R}_j\,. \end{cases} \tag{3.3}$$

In the case of nuclear scattering, the spin-component of the neutron's state is ignored and only the momentum of the neutron is considered. Also, energy conservation dictates that the energy of the combined neutron and scattering system should be

constant. If E and E' are the initial and final energies of the neutrons and E_λ and $E_{\lambda'}$ are the initial and final energies of the scattering system, then

$$\begin{cases} E + E_\lambda \ = E' \ + E_{\lambda'} \ , \\ E_{\lambda\prime} - E_\lambda = \hbar\omega. \end{cases} \tag{3.4}$$

The resulting differential scattering cross-section can be expressed as

$$(\frac{d^2\sigma}{d\Omega\, dE'}\,)_{\lambda\to\lambda'} \ = \frac{\mathbf{k}'}{\mathbf{k}}\,(\frac{m}{2\pi\hbar^2})^2 \Big|\langle \mathbf{k}'\,\lambda' \,|\, \hat{V}\,|\mathbf{k}\,\lambda\,\rangle\Big|^2 \delta(\hbar\omega + E - E'\,), \tag{3.5}$$

wherein the incident and final momenta of the neutron is given by $\mathbf{k}$ and $\mathbf{k}'$. In order to evaluate the matrix element $\langle \mathbf{k}'\,\lambda' \,|\, \hat{V}\,|\mathbf{k}\,\lambda\,\rangle$, a superposition of the contributions from each scattering centre is taken. It is assumed that the potential due to each scattering site is a short ranged potential and that each site is localized. For the j^{th} scattering centre with scattering length b_j, the potential is of the form,

$$V_j\,(\mathbf{r}_j\,) = \frac{2\pi\hbar^2}{m} b_j\,\delta(\mathbf{r}_j\,). \tag{3.6}$$

This potential is known as the **Fermi pseudopotential**. The cross-section for individual processes involving a transition from $\lambda \ \to \lambda'$ is not measured. Instead, the total cross-section for all processes is measured in a scattering experiment. Therefore, an average over all initial states and the sum over the final states of the scattering system must be taken. The fact that the the probability p_λ, that the system is in a state λ, is weighted according to the Boltzmann distribution, must be accounted for. For simplicity, if it is assumed here that the scattering centers are identical. The resulting expression for the differential cross-section for the bulk system is then given by

$$\frac{d^2\sigma}{d\Omega\, dE'} \ = \frac{\mathbf{k}'}{\mathbf{k}} \ \Big|\sum_{\lambda,\lambda'} p(\lambda\,)\,\langle\lambda'\,|\,b\sum_j e^{(i\boldsymbol{Q}\cdot\boldsymbol{r}_j)}\,|\lambda\,\rangle\,\Big|^2\ \delta(\hbar\omega + E\ - E'\,). \tag{3.7}$$

Van Hove [5] showed that this could also be expressed in terms of the scattering function, $S(\mathbf{Q},\omega)$ and the atomic density operator, $\rho_{\boldsymbol{Q}}(t)$ as shown below,

$$\begin{cases} \dfrac{d^2\sigma}{d\Omega\, dE'} = N\dfrac{\mathbf{k}'}{\mathbf{k}}\, b^2 S(\mathbf{Q},\omega)\,, \\ S(\mathbf{Q},\omega) = \dfrac{1}{2\pi\hbar N} < \rho_{\boldsymbol{Q}}(0)\rho_{-\boldsymbol{Q}}(t) > e^{-i\omega t}dt, \\ \rho_{\boldsymbol{Q}}(t) = \sum_j e^{i\mathbf{Q}\cdot \boldsymbol{r}_j(t)}. \end{cases} \tag{3.8}$$

Writing the scattering function in this manner elegantly shows how $S(\mathbf{Q},\omega)$ is the temporal Fourier transform of the pair-correlation function between the position of j^{th} atom at time zero and the i^{th} atom at time t. One important physical aspect of the function $S(\mathbf{Q},\omega)$, is the **principle of detailed balance** which is depicted in Figure 3.2. This principle states that for a pair of states in the scattering system, the *a priori* probabilities that the neutron will bring about a transition in either direction are the same. It must be kept in mind however, that the probability for the scattering system to be in either of the two states is lower for the higher energy state as is determined by the factor, $exp(-\hbar\omega\beta)$ [2]. This principle can be summarized by

$$S(-\mathbf{Q},-\omega) = \exp(-\hbar\omega\beta) S(\mathbf{Q},\omega)\,. \tag{3.9}$$

One consequence of the principle of detailed balance is that the cross-section for neutron energy gain vanishes at T = 0K, since there are no thermally generated excitations present in the scattering system.

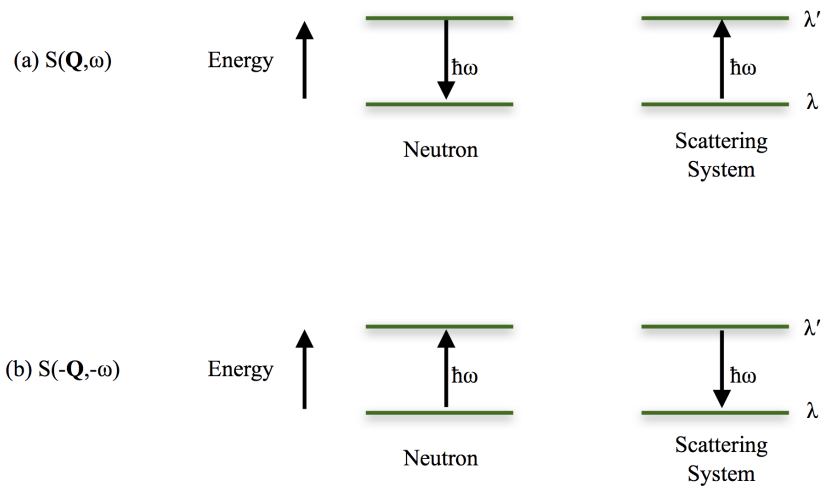

Figure 3.2: Principle of detailed balance diagram showing the transition for (a) $S(\mathbf{Q},\omega)$, where ω is positive, and (b) $S(-\mathbf{Q},-\omega)$, where ω is the same positive quantity. Adapted from Squires [2].

3.2.3 Magnetic Scattering

As discussed previously, neutrons have the ability to interact with a local magnetic field $\mathbf{B}$, since they have a magnetic moment. In neutron scattering, we are interested in the interaction between a neutron and unpaired electrons in magnetic ions. The local magnetic field generated by the electron at $\mathbf{R}$ with momentum $\mathbf{p}$ and magnetic moment μ_e can be described by

$$\boldsymbol{B} = \frac{\mu_0}{4\pi}[(\nabla \times \frac{\boldsymbol{\mu}_e \times \mathbf{R}}{|\mathbf{R}^3|}) - \frac{2\mu_B}{\hbar}\frac{\boldsymbol{p} \times \mathbf{R}}{|\mathbf{R}^3|}]. \tag{3.10}$$

The first term arises due to the electron's spin and the second is a consequence of the electron's orbital motion. With this result in mind, the interaction potential between the neutron and an electron is described by V_m, where

$$V_m = \boldsymbol{\mu}_n \cdot \boldsymbol{B}. \tag{3.11}$$

This potential can be applied to the general form for the scattering cross-section which was previously utilized in Equation (3.5). Since V_m is explicity dependent on the spin

operator, the spin state σ, of the neutron must be taken into consideration. The scattering cross-section is given by

$$\frac{d^2\sigma_s}{d\Omega\, dE'} \;|_{\lambda\,\sigma\to\lambda'\,\sigma'} = (\gamma r_0)^2 \frac{\mathbf{k}'}{\mathbf{k}} |\langle \mathbf{k}'\,\sigma'\,\lambda' \,|\, \boldsymbol{\sigma}\cdot\mathbf{K}_{\perp}\,|\mathbf{k}\,\sigma\,\lambda\,\rangle|^2, \tag{3.12}$$

where r_0 is the classical radius of the electron and $\mathbf{K}_{\perp}$ is the projection of vector $\mathbf{K}$, which is related to the Fourier transform of the magnetization density $\mathbf{M}(\mathbf{r})$ at $\mathbf{r}$. No polarization analysis will be considered in this discussion since the neutron beams utilized in the scattering experiments were unpolarized. In this regime, the initial neutron state $|\sigma\rangle$ is random and uncorrelated with $\mathbf{K}$ or with the initial state of the scattering system λ. The quantity **magnetic form factor** $f_j(\mathbf{Q})$ can be defined with $\mathbf{Q} = \mathbf{k}' - \mathbf{k}$ being the scattering vector, as given by

$$f_j(\mathbf{Q}) = \frac{\int \boldsymbol{M}(\mathbf{R}_j + \mathbf{r}_j)\exp(i\mathbf{Q}\cdot\mathbf{r}_j)d\mathbf{r}_j}{\int \boldsymbol{M}(\mathbf{R}_j + \mathbf{r}_j)d\mathbf{r}_j}. \tag{3.13}$$

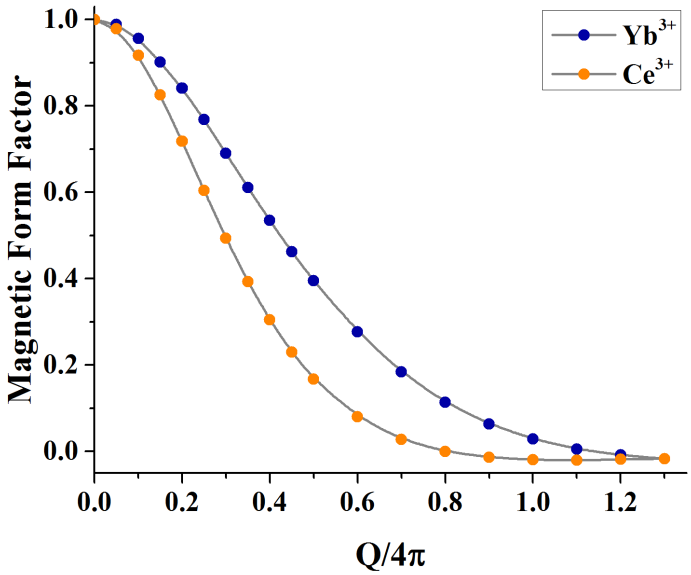

Figure 3.3: Magnetic form factor $\mathbf{Q}$ dependence for Yb^{3+} and Ce^{3+} with the results taken from [6, 7].

This is the Fourier transform of the magnetization density and typically drops off

rapidly as a function of $\mathbf{Q}$. Hence, the magnetic scattering cross-section becomes small for large $\mathbf{Q}$, as shown in Figure 3.3. Using this fact, the spin-only scattering from unpolarized neutrons can be expressed in an alternate form as given by

$$\begin{aligned}\frac{d^2\sigma_s}{d\Omega\, dE'} = (\gamma r_0)^2 \frac{\mathbf{k}'}{\mathbf{k}} \sum_{\alpha\beta}[(\delta_{\alpha\beta} - \hat{Q}_\alpha \hat{Q}_\beta) \sum_{ij} \exp(i\mathbf{Q} \cdot (\mathbf{R}_j - \mathbf{R}_i)) \\ \times \langle \lambda \,|\, S_{j\alpha} f_j(\mathbf{Q}) \,\rangle\, |\lambda'\rangle \,\langle \lambda' \,|\, S_{i\beta} f_i(\mathbf{Q}) \,|\lambda\,\rangle] \\ \times \delta(E_\lambda - E'_\lambda + \hbar\omega).\end{aligned} \tag{3.14}$$

Here, the magnetization $\mathbf{M}$, is expressed as a Fourier decomposition in terms of the magnetic form factor $f_j(\mathbf{Q})$ and $\mathbf{S}_{j\alpha}$. $S_{j\alpha}(t)$, generally expresses the resultant spin vector of the electron cloud of the j^{th} magnetic ion in the scattering system at time t. The indices α, β refer to the three rectangular co-ordinates x, y, z. Hence, $S_{j\alpha}(t)$ refers to a particular component of the spin vector of the j^{th} magnetic ion. In the same spirit as with the result for nuclear scattering, Van Hove [8] showed that the differential cross-section could be represented in terms of a magnetic scattering function, $S^{\alpha\beta}(\mathbf{Q}, \omega)$ as shown in the following equations,

$$\begin{cases} \dfrac{d^2\sigma}{d\Omega\, dE'} = (\gamma r_0)^2 \dfrac{\mathbf{k}'}{\mathbf{k}} \dfrac{N}{\hbar} |f(\mathbf{Q})|^2 \sum\limits_{\alpha\beta}[(\delta_{\alpha\beta} - \hat{Q}_\alpha \hat{Q}_\beta) S^{\alpha\beta}(\mathbf{Q}, \omega)\,, \\ S^{\alpha\beta}(\mathbf{Q}, \omega) = \dfrac{h}{N} \sum\limits_{ij} \displaystyle\int_{-\infty}^{\infty} \exp(i\omega t) dt \times \langle S_{j\alpha}(0) S_{i\beta}(t) \rangle\,, \\ S_{j\alpha}(t) = \exp(-i\mathbf{Q} \cdot \mathbf{R}_j\,(t)). \end{cases} \tag{3.15}$$

Notice that the magnetic scattering function $S^{\alpha\beta}(\mathbf{Q}, \omega)$, is a second-rank tensor. This reflects that it is only the magnetization in the plane perpendicular to $\mathbf{Q}$ that gives rise to neutron scattering [3]. In this case, the scattering function is represented in terms of the Fourier transform of the spin-correlation function, $\langle S_{j\alpha}(0) S_{i\beta}(t) \rangle$, between the i^{th} and j^{th} magnetic ions in the scattering system at different times. This result shall be considered further in Section 3.2.4.2.

3.2.4 Bragg Scattering

As pointed to in the previous sections, both the nuclear and magnetic differential cross-sections can be expressed in terms of a Fourier transform of a pair-correlation function and spin-correlation function respectively. In the former case, it is a Fourier transform in space and time between two atoms and in the latter, it is a Fourier transform in space and time between two spins. Here, a less theoretical approach is taken and the basic concept of crystal structure and diffraction shall be discussed and put into context of the pair-correlation and spin-correlation function. Detailed information involving crystal structure, crystallographic symmetry groups and structure determination via diffraction can be found in the following references [9–11].

3.2.4.1 Elastic Nuclear Scattering

Crystalline lattices have a special property in comparison to liquids, gases and glassy materials, in that they posses a periodic structure. $Yb_2Ti_2O_7$ and Ba_2YOsO_6 are examples of crystalline materials. In order to describe their three-dimensional structure, one needs a description of the **Bravais lattice**, which specifies the periodic array in which the repeated units of the crystal are arranged. The units need not necessarily be atoms, but can more generally be a group of atoms or molecules. The most important point to note is that in this definition, the Bravais lattice looks the same from any viewpoint of the lattice. The definition of the Bravais lattice lies in that fact that the positions of the units are related by translation on an infinite length scale. Hence, the unit is the most basic building block in generating the full crystal structure by translation symmetry. A more rigourous mathematical description involves defining three **real lattice vectors**, $\mathbf{a_1}$, $\mathbf{a_2}$ and $\mathbf{a_3}$. If these vectors are taken in an integral superposition $\mathbf{R}$, where $\mathbf{R} = n_1\mathbf{a_1} + n_2\mathbf{a_2} + n_3\mathbf{a_3}$ (n_i with $i = 1, 2, 3$ are all integers), $\mathbf{R}$ represents the position of the units in the crystal. The Fourier space of **real space** is termed **reciprocal space**. Reciprocal space is more convenient for the conceptualization of scattering experiments and in general, data is interpreted in this space. To describe reciprocal space, one requires three **reciprocal lattice vectors**, $\mathbf{b_1}$, $\mathbf{b_2}$ and $\mathbf{b_3}$. These vectors can be obtained from the real space vectors using the following relations,

$$\begin{cases} \boldsymbol{b}_1 = 2\pi \dfrac{\boldsymbol{a}_2 \times \boldsymbol{a}_3}{\boldsymbol{a}_1 \cdot (\boldsymbol{a}_2 \times \boldsymbol{a}_3)}, \\ \boldsymbol{b}_2 = 2\pi \dfrac{\boldsymbol{a}_3 \times \boldsymbol{a}_1}{\boldsymbol{a}_1 \cdot (\boldsymbol{a}_2 \times \boldsymbol{a}_3)}, \\ \boldsymbol{b}_3 = 2\pi \dfrac{\boldsymbol{a}_1 \times \boldsymbol{a}_2}{\boldsymbol{a}_1 \cdot (\boldsymbol{a}_2 \times \boldsymbol{a}_3)}. \end{cases} \tag{3.16}$$

The reciprocal lattice vector $\mathbf{G} = l_1\mathbf{b_1} + l_2\mathbf{b_2} + l_3\mathbf{b_3}$ physically corresponds to a vector which is perpendicular to a family of equally spaced planes of atoms referred to as a set of **Miller planes**. This situation is depicted in Figure 3.4. Bragg formulated a theory of diffraction, which describes the diffraction of rays with wavelength λ, in terms of the constructive interference of the specularly reflected rays from these planes. In a neutron scattering experiment, if the path difference between incident and scattered neutrons from a set of Miller planes is equal to an integral number of wavelengths, then the diffraction condition as given by Equation (3.17) is met, wherein d denotes the spacing between the planes.

$$n\lambda = 2d \sin\theta. \tag{3.17}$$

The diffraction condition can also be thought of in terms of the change in wavevector of the neutron. When the change in wavevector is a reciprocal lattice vector (i.e. $\mathbf{k}' - \mathbf{k} = \mathbf{G}$), then the diffraction condition is met. In order to visualize a typical single-crystal diffraction experiment, the **Ewald sphere** construction is highly useful. It involves considering a map of three-dimensional reciprocal space and drawing a sphere of radius $|\mathbf{k}|$ which is centred on the incident wavevector $\mathbf{k}$. The diffraction condition is met if there is some scattered wavevector $\mathbf{k}'$ for which a reciprocal lattice point lies on the edge of the circle.[2]

In the case of a powder sample, there are many small crystalline particles which are randomly oriented. This situation is equivalent to fixing the incident wavevector $\mathbf{k}$, and the Ewald sphere, and allowing reciprocal space to rotate through all angles about the origin. When each reciprocal lattice vector $\mathbf{G}$ is rotated through all orientations, this generates a sphere of radius $|\mathbf{G}|$ about the origin. This sphere will intersect the Ewald sphere provided that the condition

[2]For some $\mathbf{k}' \neq 0$.

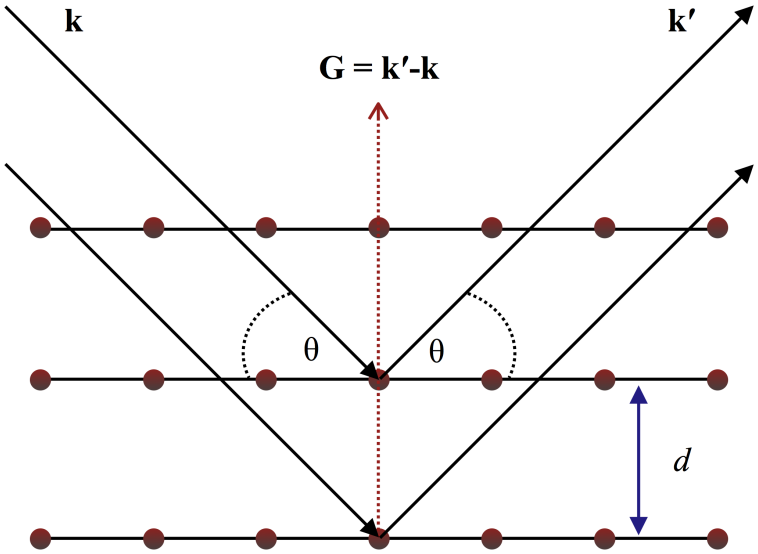

Figure 3.4: Development of Braggs Law through the constructive interference of neutrons from a family of Miller planes

$$|\mathbf{G}| < 2|\mathbf{k}|, \tag{3.18}$$

is met. The use of the Ewald sphere construct in illustrating powder diffraction is shown in Figure 3.5. Instead of having one individual point intersecting the Ewald sphere as is the case with single-crystals, rings are traced for each $\mathbf{G}$ satisfying the requirement in Equation (3.18). Hence a powder diffraction pattern is characterized by these rings.

The fact that the crystals have a periodic structure imply that there are correlations between atoms over infinite time and space. This generates the following term in the partial differential cross-section, $\delta(\omega)\sum_{g}\delta(\mathbf{Q}-\mathbf{G})$. The implication here is that, scattering is zero unless $\omega = 0$ and $\mathbf{Q} = \mathbf{G}$. These are precisely the conditions for Bragg diffraction outlined earlier. This type of scattering is termed **Bragg scattering** and can also be observed systems which exhibit magnetic order. This phenomenon will be considered more rigorously in the following section for magnetic Bragg scattering.

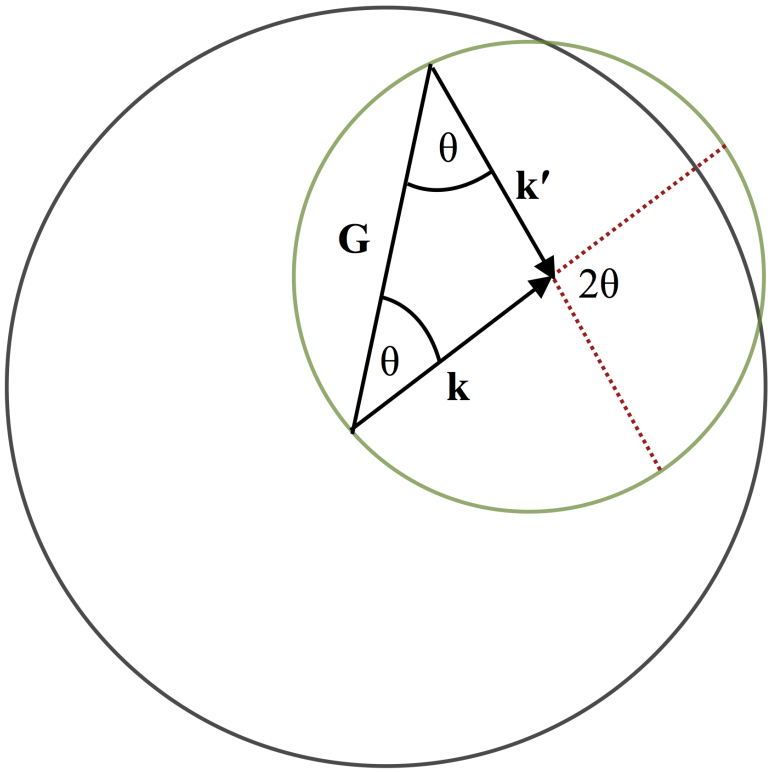

Figure 3.5: The Ewald construction for powder diffraction. The incident wavevector is $\mathbf{k}$ and the diffracted wavevector satisfying the diffraction condition is $\mathbf{k}'$. The Ewald sphere is the smaller sphere. It is centred on the tip of the incident wavevector $\mathbf{k}$ so that the origin is on its surface. The larger sphere is centred on the origin and has a radius $\mathbf{G}$. The two spheres intersect in a circle and Bragg reflections will occur for any wave vector $\mathbf{k}'$ connecting any point on the circle of intersection to the tip of the vector $\mathbf{k}$. Adapted from Mermin [9].

3.2.4.2 Elastic Magnetic Scattering

Consider the expression for magnetic scattering in Equation (3.15), involving the spin-correlation function $\langle S_{j\alpha}(0)S_{i\beta}(t)\rangle$. In the paramagnetic state, there are no spin correlations, C_{para}, where

$$\lim_{t\to\infty}\langle S_{\mathbf{0}\alpha}(0)S_{\mathbf{R}\,\beta}(t)\rangle = 0. \tag{3.19}$$

However, for a spin-system which orders below a particular T_C, there are finite spin-correlations, C_{ord} which exist for all $t \to \infty$ and for all $\mathbf{R}$. Hence,

$$\lim_{t\to\infty}\langle S_{\mathbf{0}\alpha}(0)S_{\mathbf{R}\,\beta}(t)\rangle \neq 0. \tag{3.20}$$

The spin-correlation function can be considered as the sum $C = C_{ord} + C_{para}$. If there are spin-correlations and the Fourier transform is computed for the ordered term alone, a similar situation is observed as was for the nuclear case wherein,

$$\int_{-\infty}^{\infty}\exp i\omega t\,\langle S_{\mathbf{0}\alpha}(0)S_{\mathbf{R}\,\beta}(t)\rangle\,dt = 2\pi\delta(\omega)\,\langle S_{\mathbf{0}\alpha}(0)S_{\mathbf{R}\,\beta}(t)\rangle\,. \tag{3.21}$$

That is, the scattering contribution from the ordered state is weighted by the Dirac distribution $\delta(\omega)$ at zero energy transfer. This implies that a neutron scattered in this case will neither gain nor lose energy, and this is precisely elastic scattering. Denoting the elastic contribution to scattering as $S_{el}^{\alpha\beta}(\mathbf{Q},\omega)$, the cross-section within the static approximation [3] is given by,

$$S_{el}^{\alpha\beta}(\mathbf{Q},\omega) \;= \delta(\omega)\sum_{\mathbf{R}}\langle\exp(i\mathbf{Q}\;\cdot\mathbf{R}\,)\,\langle S_{\mathbf{0}\alpha}(0)S_{\mathbf{R}\,\beta}(t)\rangle\rangle\,. \tag{3.22}$$

Magnetic ordering is of infinite spatial extent and a sum in $\mathbf{R}$ will give rise to delta distributions at specific scattering vectors $\mathbf{Q}$ in reciprocal space. These scattering vectors correspond to magnetic reciprocal lattice vectors. This implies that elastic magnetic scattering will only be observed at magnetic reciprocal lattice points.

3.3 Neutron Scattering Techniques

Time-of-flight and triple-axis neutron scattering techniques were utilized to make measurements on $Yb_2Ti_2O_7$ and Ba_2YOsO_6. The basic principles of these techniques will be described. In addition, their strengths and suitability in probing the phenomena of interest will be discussed.

3.3.1 Time-of-Flight Neutron Scattering

Time-of-flight neutron scattering is a technique, which utilizes pulses of neutrons, permitting the timing of individual neutron scattering events. In this method, information regarding the individual neutron momentum and energy transfer are measured. These measurements can be conducted at both pulsed neutron and reactor sources. The principle of this technique is outlined in the following discussion and Figure 3.6 provides an illustration.

In this technique, one controlled parameter is the initial energy E_i of the neutrons. The choice of E_i depends on the energy scales of the phenomena of interest. Monchromatization of the neutron pulse is generated with the use of Fermi choppers. The chopper settings are chosen so as to produce a well defined pulse of neutrons of initial velocity v_i, and incident energy E_i. The monochromatic pulse then interacts with the sample and each neutron gains, loses or exchanges energy with the sample. The scattering angle and time-of-flight of each neutron are recorded at the detectors. The distances x_{PS} and x_{SD} are fixed, permitting the ability to determine the final energy E_f and velocity v_f of the neutrons after they are scattered. These quantites can be determined from

$$t_{TOF} = \frac{x_{CS}}{v_i} + \frac{x_{SD}}{v_f}. \tag{3.23}$$

Armed with this information, the energy transfer ΔE, can be easily determined from $\Delta E = E_f - E_i$. As mentioned, the angle of deflection for each neutron is measured at the detectors. With these two ingredients, a map of $S(\mathbf{Q}, \omega)$ can be obtained.

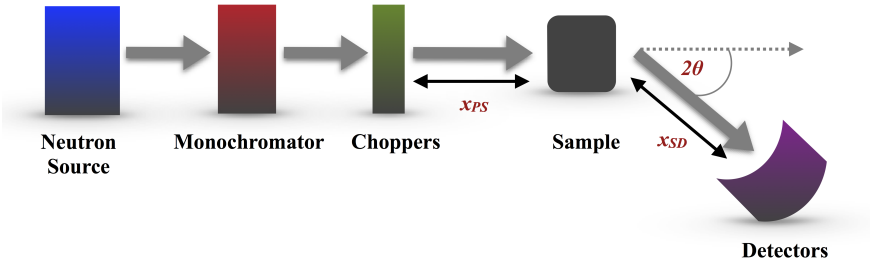

Figure 3.6: A simple schematic illustrating the time-of-flight technique.

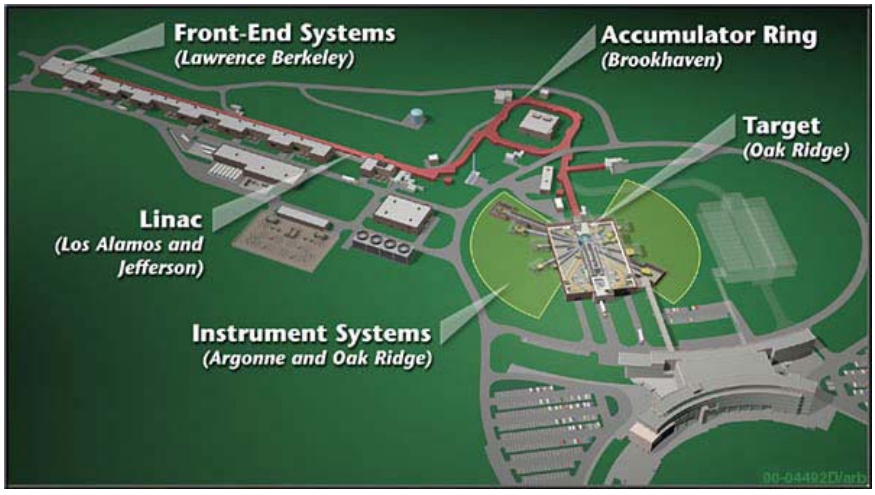

Figure 3.7: An illustration of the steps involved with neutron production and delivery at the Spallation Neutron Source, Oak Ridge [12].

3.3.1.1 SEQUOIA: The Fine Resolution Chopper Spectrometer

Measurements were conducted on the *fine resolution chopper spectrometer, SEQUOIA BL-17,* located at, the Spallation Neutron Source (SNS) at Oak Ridge National Laboratory. SEQUOIA is one of eighteen beam lines at SNS which are each optimized to investigate a variety of energy and length scales. There is a single target station which feeds each of these beam lines with neutrons and the schematic for neutron production and delivery can be seen in Figure 3.7.

At the front end building, there is an ion source which produces negatively charged hydrogen ions (H^-), which are formed into 1ms pulses with the use of electrostatic choppers. The pulses are also accelerated to an energy of 2.5MeV before being directed to the linear accelerator, or linac [13]. The linac accelerates the pulses further to an energy of 1GeV. The H^- ion bunches are then delivered to a proton accumulator ring, and a stripper foil extracts protons from these ions. These protons are then circulated through the ring to produce sharp and intense pulsed proton bunches. The proton bunches subsequently bombard a liquid mercury target, producing neutron bunches. A moderator which is beamline specific, is used after neutron production in order to slow the neutrons. The neutrons are then directed to the respective beam line. For SEQUOIA, decoupled ambient water is used as a moderator in order to produce room-temperature neutrons.

SEQUOIA is a direct geometry chopper spectrometer (DGCS) with fine energy transfer ω and $\mathbf{Q}$ resolution, and is one of four DGCSs at SNS. It is optimized to probe dynamical processes in materials such as novel magnetic excitations and fluctuations, as well as lattice vibrations [13]. The schematic in Figure 3.8 shows the key elements of the beam line. The neutron guide is designed to reduce the loss of neutron flux during the course of neutron flight to the sample. There are two sets of choppers, the two Fermi choppers F_{c1} and F_{c2} and the T_0 chopper. These choppers are utilized for specific purposes in order to produce clean and monochromatic neutron pulses. The vertical rotation axis T_0 chopper blocks fast neutrons[3] and is also used as a bandwidth limiting chopper, controlling the arrival of neutrons at the Fermi choppers. The Fermi choppers monochromate the neutron pulse. E_i can be set anywhere within the range, $4\text{meV} - 2\text{eV}$ and the energy resolution is dependent on the choice of E_i. Typically, the energy resolution is roughly $\sim$ 1-5% of E_i. The highest neutron flux is produced

[3]Fast neutrons are produced when the proton pulses strike the mercury target.

when $E_i \sim 100$meV [14]. The Fermi-chopper to sample distance is 2m and sample to detector distance is 5.3m to 6.3m. The large detector bank is comprised of ^{3}He linear position sensitive tube detectors (LPSDs) that are assembled into 8-packs in a cylindrical geometry. As this instrument is optimized to probe magnetic excitations, the detector bank is designed to cover a lower $\mathbf{Q}$ range. The SEQUOIA detector bank provides angular coverage between $-30°$ and $60°$.

The fact that SEQUOIA is designed to measure magnetic phenomena and $S(\mathbf{Q}, \omega)$ can be obtained over a broad $\mathbf{Q}$-range, makes it an ideal instrument for the measurement of both $Yb_2Ti_2O_7$ and Ba_2YOsO_6.

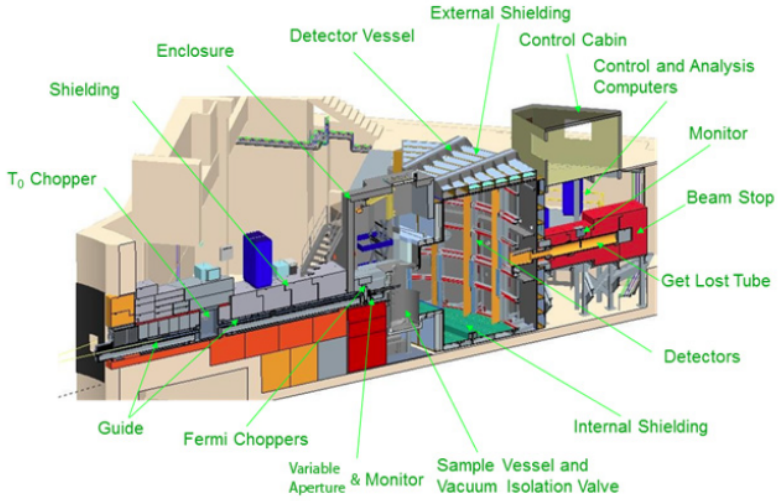

Figure 3.8: Layout and key components of SEQUOIA BL-17 at the Spallation Neutron Source sourced from M.B. Stone.

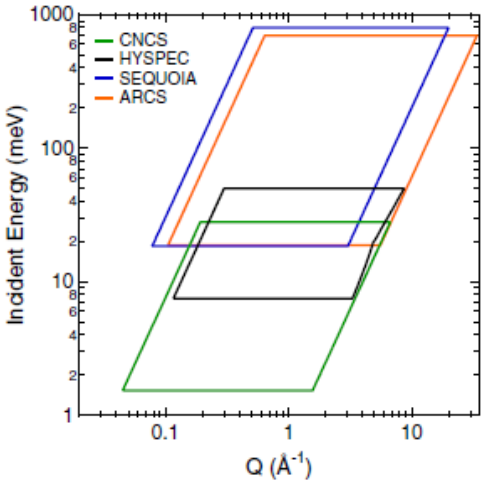

Figure 3.9: Comparison of energy and **Q** coverage capabilities of all direct geometry chopper spectrometers at Oak Ridge [13].

3.3.2 Triple-axis Spectrometer

The typical set-up for a triple-axis spectrometer is shown in Figure 3.10. As suggested by its name, in this technique neutrons are scattered about three parallel axes through the angles $2\Theta_M$, ϕ and $2\Theta_A$. In this configuration, a white neutron beam is set incident on a monochromating crystal which selects neutrons of a particular wavelength λ. The neutrons are reflected at an angle $2\Theta_M$ towards the sample of interest. The neutrons scattered from the sample are then incident on an analyzer crystal, which is located at an angle ϕ relative to this stream of neutrons. This crystal selects neutrons of wavelength λ'. The neutrons are then finally reflected at an angle $2\Theta_A$ towards the detector. By choosing the appropriate monochromator and analyzer crystals, the initial and final wavelength of the neutrons are chosen. Hence the energy transfer ΔE, is fixed and manipulated in the experiment.

In this set-up, one can virtually go to any position in $\mathbf{Q}$. As ΔE can also be freely chosen, this technique is especially effective when the position and energy scale of the phenomena of interest are known exactly. Since $\mathbf{Q}$ positions of the magnetic Bragg peaks for Ba_2YOsO_6 were determined from an earlier experiment at SNS, this provided the necessary information to conduct a fine measurement of the critical phenomena in Ba_2YOsO_6. These measurements were conducted at the N5 triple-axis spectrometer located at the Canadian Neutron Beam Center at Chalk River National Laboratories. The following section provides more details regarding the components of the triple-axis spectrometer.

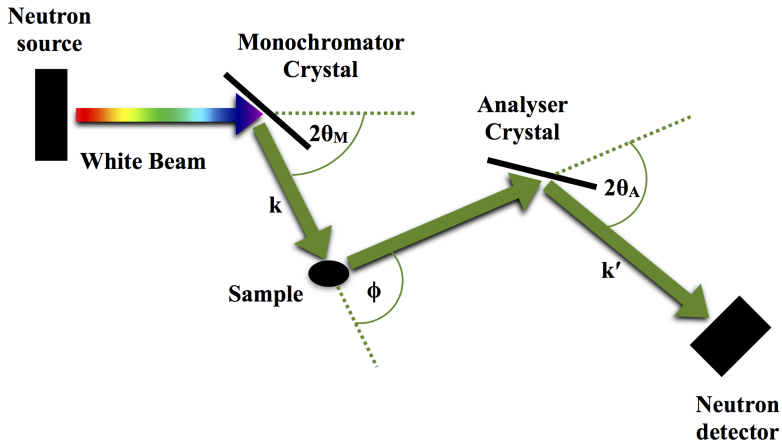

Figure 3.10: Basic elements of a triple-axis spectrometer adapted from [3].

3.3.2.1 Elements of the Triple-axis Spectrometer

There are several components in the set-up of a triple-axis spectrometer, which are important in defining the neutron beam profile which is delivered to the sample and detector. It is important to ensure for example, that the maximum possible neutron intensity is delivered to the sample. Other concerns involve the control of beam divergences and contamination of the neutron beam due to higher-order neutrons. The following discussion will describe the function and necessity of the monochromator crystal, analyzer crystal, collimators and filters in the triple-axis set-up. More detailed discussions regarding these components can be found in the text by Shirane [1]. Brief mention of the detector arrangement used at N5 spectrometer will also be made.

One of the most important components of the triple-axis instrument is the **monochromator** crystal. The monochromator crystal tends to constrain the angular divergence of the neutron beam and also determines the intensity of neutrons incident on the sample. A detailed description of the relationship governing the intensity of neutrons scattered from a monochromator can be obtained from work done by Bacon [15] and Bacon and Lowde [16]. Here, a brief discussion of the function and properties which should be considered in the choice of monochromators, are outlined. By definition, the monochromator selects the incident neutron wavelength from the white beam obtained from a reactor. This is achieved by orienting the monochromator crystal at an angle θ_B which satisfies the Bragg condition in Equation (3.24). Neutrons of a particular wavelength are selected by Bragg diffraction from a set of Miller planes with spacing d_{hkl} and index (hkl) as given by

$$\lambda = 2d_{hkl} \sin \theta_B. \tag{3.24}$$

The angular width of a Bragg diffracted beam from a perfect single-crystal monochromator is much smaller than the beam divergences with which one must work with in order to obtain acceptable beam intensities [1]. Instead, a low absorption mosaic crystal[4] or ideal imperfect crystal is better suited. The distribution of angles for a mosaic crystal can be expressed as a Gaussian function W of width η, as shown below,

[4] A mosaic crystal contains many small crystallites with small relative misorientation.

$$W(\Delta) = \frac{1}{\sqrt{2\pi}\eta} \exp\left(-\frac{\Delta^2}{2\eta^2}\right). \tag{3.25}$$

Here, the parameter Δ is used to assign the orientation of a crystallite in the mosaic relative to the average position of the crystallites constituting the mosaic. The quantity η refers to the mosaic width. In an experiment however, it is more convenient to characterize the distribution by the full-width half maximum (FWHM) which is related to η by

$$\eta(FWHM) = 2\sqrt{2\ln(2\eta)}. \tag{3.26}$$

The **peak reflectivity** R_θ, is a property of the monochromator which should be taken into consideration. It is an indicator of how well the neutron beam of wavelength λ, is transmitted after Bragg diffraction by the monochromator. Assuming that the monochromator has thickness t_0, an expression for the R_θ is given by

$$\begin{cases} R_\theta = 0.96 \left(\dfrac{Q_c\, t_0}{\eta \sin\theta_B}\right)^{\frac{1}{2}}, \\ Q_c \ = \dfrac{\lambda^3 F_N^2}{v_0^2\, 2\theta_B}, \\ F_N = \displaystyle\sum_j b_j\, e^{i\mathbf{Q}\cdot\mathbf{r}_j}\,. \end{cases} \tag{3.27}$$

R_θ is related to the crystallographic quantity Q_c and Q_c is related to the nuclear structure factor F_N and the unit-cell volume of the monochromator, v_0. In the expression for F_N, the quantities $\mathbf{r}_j$ and b_j have the same definition as provided in Section 3.1.

It is clear, that in order to have a large peak reflectivity, Q_c must be large. Therefore, crystals chosen as monochromators should have small unit-cell volumes and relatively large scattering lengths. In addition, the materials must have a relatively low absorption co-efficient. Some good choices for the monochromating crystal include beryllium, pyrolytic graphite (PG), silicon and copper. As the **analyzer** crystal selects the final wavelength of the neutrons by Bragg diffraction, this discussion also applies to the selection of an analyzer crystal. In fact, Equation (3.27) applies better to the situation

involving the analyzer, especially when elastic scattering on a triple-axis instrument is considered. More relevant to the monochromator is the integrated reflectivity as a function of wavelength R_λ , as given by

$$R_\lambda = R_\theta \lambda \cot\theta_B. \tag{3.28}$$

One difficulty encountered in the use of single-crystals as monochromators in particular, is a consequence of double Bragg scattering. This occurs when two Bragg planes simultaneously satisfy the Bragg condition given in Equation (3.24). This effect increases with the size of the unit cell and the illuminated volume. This effect also increases the background and also causes variations in the measured values of R_λ since the conditions for multiple scattering vary as λ varies. The reflectivity is also sensitive to the rotation of the crystal about the scattering vector $\mathbf{Q}$, and will cause reflections competing with the desired one to move into or out of the scattering. The PG filter is an ideal filter since the effects described above are avoided. PG has highly preferred orientation of the $(00l)$ planes, but the other (hkl) planes are aligned at random. A good PG filter would be characterized by a mosaic width of $\lesssim 0.5°$.

Now we shall turn our attention to neutron filters. To highlight the importance of their usage, we must consider the process of Bragg diffraction which occurs at the monochromator (or analyzer). For the remainder of this discussion, any statement made about the monochromator equivalently applies to the analyzer crystal. As mentioned previously, if the monochromator is oriented at the correct angle θ_B, the neutron beam will be Bragg diffracted by a family of Miller planes indexed by (hkl), with plane separation of d_{hkl}. If the symmetry of the monochromator crystal is such that, (nh, nk, nl) reflections are also allowed, then at the same θ_B, neutrons of wavelength $\frac{\lambda}{n}$ are also diffracted. The neutrons which are diffracted and have wavelength $\frac{\lambda}{n}$ are referred to as, higher-order neutrons. If these higher-order neutrons are not masked, experimental results can be wrongly interpreted. Therefore, suitable masks are used in order to block these higher-order neutrons. Some example of filters which attenuate these higher-order neutrons are PG and beryllium filters. The PG filter is one of the most useful filters when the higher-order neutrons are in the thermal energy regime [1].

Collimators are also key elements in the triple-axis set-up. We shall consider Soller collimators which are used to control beam divergence within the horizontal scattering

plane. A Soller slit consists of parallel plates which are coated in neutron absorbing materials and are separated by a distance. These collimators are placed at different points in the three-axis instrument. For example, it is possible to add collimators before and after the monochromator. Therefore, the angular divergence of the beam can be controlled at every point of experimental the set-up. Typical values for the horizontal divergence from the Soller slits are in the range $0.1° \lesssim \alpha \lesssim 1.5°$. It must be kept in mind however, that collimators are not the only limiting factor on angular divergences. Other factors which may limit the divergence include the sample size, size of monochromator, as well as any beam defining masks. It is important to account for these angular divergences as they are key parameters in calculating the resolution function of the spectrometer.

One final element for consideration in the set-up is the detector. At N5, a 32-wire ^3He position sensitive detector is utilized. The wires are spaced by 2mm and are capable of detecting neutrons at the corresponding angular position.

Bibliography

[1] G. Shirane, S.M. Shapiro, and J.M. Tranquada. *Neutron Scattering with a Triple-Axis Spectrometer Basic Techniques*. Cambridge University Press, 2002.

[2] G.L. Squires. *Introduction to the theory of thermal neutron scattering*. Dover Publications Inc., 1978.

[3] M.F. Collins. *Magnetic Critical Scattering*. Oxford University Press, 1989.

[4] G.E. Bacon. *Fifty Years of Neutron Diffraction: The Advent of Neutron Scattering*. Adam Hilger, Bristol, 1986.

[5] L. Van Hove. *Phys. Rev.*, 95(249), 1954.

[6] M. Blume, A.J. Freeman, and R.E. Watson. 37:1245–1253, 1962.

[7] M. Blume, A.J. Freeman, and R.E. Watson. 41:1878, 1964.

[8] L. Van Hove. *Phys. Rev.*, 95(1374), 1954.

[9] N.W. Aschcroft and N.D. Mermin. *Solid State Physics*. Harcourt College Publishers, 1976.

[10] V.K. Pecharsky and P.Y. Zavalij. *Fundamanetals of Powder Diffraction and Structural Characterization of Materials*. Springer, 2005.

[11] C. Hammond. *The Basics of Crystallography and Diffraction*. Oxford University Press, 2009.

[12] SNS, Oak Ridge National Laboratory. `http://neutrons.ornl.gov/facilities/SNS/works.shtml`. Accessed: 2014-08-22.

[13] M.B. Stone, J.L. Niedziela, D.L. Abernathy, L. DeBeer-Schmitt, G. Ehlers, O. Garlea, G.E. Granroth, M. Graves-Brook, A.I. Kolesnikov, A. Podlesnyak, and B. Winn. *Rev. Sci. Instrum.*, 85(045113), 2014.

[14] E.B. Iverson, P.D. Ferguson, F.X. Gallmeier, and I.I. Popova. *Detailed SNS Neutronics Calculations for Scattering Instrument Design: SCT Configuration*. Spallation Neutron Source Report, 2002.

[15] G.E. Bacon. *Neutron Diffraction.* Clarendon Press, Oxford, 1975.

[16] G.E. Bacon and R.D. Lowde. *Acta. Cryst.*, 1, 1948.

Chapter 4

The Effect of Stuffing on the Fragile Ground State of $Yb_2Ti_{2-x}Yb_xO_{7-x/2}$

4.1 Background

In this study, the crystal-field (CF) splittings of the Yb^{3+} ion in $Yb_2Ti_2O_7$ are measured with the use of the time-of-flight (TOF) inelastic neutron (INS) technique. By obtaining this information, it is possible to determine of the CF parameters which describe the CF Hamiltonian $\mathcal{H}_{CF}$[1]. If the CF Hamiltonian is known, the ground state wave function and components of the g-tensor of the Yb^{3+} ion in $Yb_2Ti_2O_7$ can be deduced. As discussed in Section 2.1, knowledge of the size and anisotropy of the magnetic moment is key to a full description of the low temperature properties of $Yb_2Ti_2O_7$.

It has been proposed that the low temperature phase of $Yb_2Ti_2O_7$ in zero field lies near to a phase boundary which separates a variety of states including, the quantum spin liquid (QSL), Coulomb ferromagnet (CFM), standard ferromagnet (FM) and standard anti-ferromagnet (AFM) phases [1]. Since numerous studies on $Yb_2Ti_2O_7$ report different low temperature behaviour of $Yb_2Ti_2O_7$ in zero field, there has been question as to whether these differences are manifested as a result of sample defects. Powder neutron diffraction studies conducted on a pulverised single-crystal grown by the float-zone method reveal the presence of an excess of Yb^{3+} ions on Ti^{4+} sites [2]. It has been suspected that the disorder induced as a result of this excess of Yb^{3+} ions modifies the zero-field ground state, permitting the realization of the

[1]See Section 2.1 for a description of the crystal-field Hamiltonian $\mathcal{H}_{CF}$.

different phases reported in $Yb_2Ti_2O_7$ [1]. To consider this effect which is referred to as stuffing, INS measurements are conducted on a pulverised single-crystal sample which is chemically described by the formula, $Yb_2Ti_{2-x}Yb_xO_{7-\frac{x}{2}}$ (x = 0.046). These results are compared with those obtained for a powder sample, which is described by a stoichiometric chemical formula, $Yb_2Ti_2O_7$.

The theoretical framework according to Hutchings [3] facilitates the determination of the CF Hamiltonian for rare-earth compounds (see Section 2.1). The CF Hamiltonian which is determined from this approach (see Equation (2.3)) is defined only within the space of the ground state multiplet. Information regarding the relative magnetic dipole transition intensities between CF levels are necessary in the determination of the CF parameters. Inelastic neutron scattering techniques which can provide this information make it possible to determine these CF parameters. This procedure can be utilized since the first excited doublet within the ground state multiplet is well separated from the ground state doublet. One advantage to this procedure is that the excited multiplets can be ignored since the first excited multiplet for each of the ions in the rare-earth series is located at a temperature equal to or larger than 4750K, with the exception of Tb^{3+} [4][2].

This procedure has been effectively applied to two Tb $^{3+}$ based pyrochlore compounds, $Tb_2Ti_2O_7$ and $Tb_2Sn_2O_7$, in a study by Zhang *et al.* [6]. Many attempts have been made through a variety of experimental techniques to determine the CF parameters, components of the g-tensor and ground state wave function for a variety of rare-earth ions in the $A_2B_2O_7$ pyrochlore series [7–14, 6, 15]. We shall restrict our attention however, to the previous work that has been done in the case of the Yb^{3+} ion in $Yb_2Ti_2O_7$.

One of the early CF studies conducted by Sengupta *et al.*[15] has shown much disagreement with later studies conducted on $Yb_2Ti_2O_7$ because it was assumed that the Yb^{3+} magnetic moments host easy-axis magnetic anisotropy [15]. Later experimental and theoretical results however, have established that Yb^{3+} magnetic moments have local easy plane or XY anisotropy with overall ferromagnetic exchange [13, 12, 16].

The study by Bertin *et al.*[7] involved the investigation of the CF splitting schemes for six rare-earth ions in the $R_2Ti_2O_7$ series (where R = Tb, Dy, Ho, Yb, Er and Tm). This study utilized neutron scattering data from other sources [9, 10, 13] in the

[2]The energetic splittings between the ground state multiplet and first excited multiplet for numerous rare-earth ions were originally determined from optical spectroscopy by Dieke [5].

determination of the CF parameters A_m^n for some of the rare-earth compounds studied. As there was no experimental data available in the case of Yb^{3+}, the CF parameters were determined with the the use of a scaling law[3]. The calculated values of $g_\parallel$ and $g_\perp$ for $Yb_2Ti_2O_7$ reported in this study lie between those determined by Hodges *et al.*[12] and Cao *et al.*[17]. The former utilized results from ^{170}Yb Mössbauer spectroscopic, ^{172}Yb perturbed angular correlation, magnetization and susceptibility measurements, in order to determine the ground state wave function and g-tensor of the Yb^{3+} ion. The latter study utilized the CF parameters deduced for $Ho_2Ti_2O_7$ by Rosenkranz *et al.*[13] and a scaling law in order to obtain CF parameters for $Yb_2Ti_2O_7$.

A study by Malkin *et al.*[14] utilized optical spectroscopy to directly probe the CF excitations in $Yb_2Ti_2O_7$. As CF levels within the ground state multiplet and excited multiplets of the Yb^{3+} ion in $Yb_2Ti_2O_7$ were measured, the *exchange charge model* or ECM [18] was utilized to formulate the CF Hamiltonian $\mathcal{H}_{CF}$. A reasonable set of initial CF parameters were chosen and varied in order to obtain CF energies and wave functions which were consistent with measured frequencies of optical zero-phonon transitions, components of the g-tensor in the ground state and the relative thermal variation of the canonical average of the electronic quadrupolar moment [14]. These calculated CF energies were compared with the experimentally observed CF energies from their optical spectroscopy measurements. However, the final reported ECM parameters underestimated one of the CF sub-levels in the first excited multiplet.

Considering the above discussion, numerous attempts have been made to determine the ground state wave function, g-tensor and an CF appropriate set of CF parameters which describe the CF Hamiltonian of $Yb_2Ti_2O_7$. However, INS measurements are invaluable in a direct determination of these desired quantities. To our best knowledge, INS techniques have never been utilized to unambiguously determine an appropriate set of CF parameters for $Yb_2Ti_2O_7$ from measured relative neutron scattering intensities and CF energies. SEQUOIA is an appropriate instrument with which these measurements can be conducted because the energy scale of the CF energies in $Yb_2Ti_2O_7$ are well within instrumental capabilities. As discussed in Chapter 3, the incident energy (or E_i) is selected in a TOF INS experiment. Hence, the incident energy of the neutrons is chosen on an energy scale corresponding to the energies of the CF excitations. Therefore, information on the scattering function, $S(|\mathbf{Q}|, \omega)$, can be obtained for a range of energy transfers up to the chosen E_i. The large array of detector

[3]See [3].

banks available at SEQUOIA also make it possible to measure $S(|\mathbf{Q}|, \omega)$ over a large range in reciprocal space. As the nature of the ground state in $Yb_2Ti_2O_7$ is still highly debated, the exact determination of the ground state wave function and the anistropy associated with the Yb^{3+} ion in $Yb_2Ti_2O_7$ is important. Also, an investigation of the differences in the INS spectra obtained for the stuffed and stoichiometric samples are important in determining the degree of the effect of stuffing on the low temperature properties exhibited by this system.

4.2 Background on Theoretical Calculation and Fits

This section highlights the procedure in determining the CF parameters from the experimental results obtained from INS measurements conducted on $Yb_2Ti_2O_7$. First, a theoretical description of the CF Hamilton of $Yb_2Ti_2O_7$ is required and can be obtained from the framework according to Hutchings [3]. The appropriate $\mathcal{H}_{CF}$ relevant to $Yb_2Ti_2O_7$ is given by

$$\mathcal{H}_{CF} = \alpha_J D_2^0 O_2^0 + \beta_J (D_4^0 O_4^0 + D_4^3 O_4^3) + \gamma_J (D_6^0 O_6^0 + D_6^3 O_6^3 + D_6^3 O_6^3). \tag{4.1}$$

The quantities D_n^m are the CF parameters which need to be determined and the O_n^m terms are the Stevens' operators which are functions of the total angular momentum operators. Previously discussed in Section 2.1.2, were the properties of the Stevens' operators which simplify the expression of the CF Hamiltonian. Taking these properties into consideration, the CF Hamiltonian can be written in a simplified block diagonal form,

$$\mathcal{H}_{CF} = \begin{pmatrix} H_{1,1} & 0 & 0 & H_{1,4} & 0 & 0 & H_{1,7} & 0 \\ 0 & H_{2,2} & 0 & 0 & H_{2,5} & 0 & 0 & H_{2,8} \\ 0 & 0 & H_{3,3} & 0 & 0 & H_{3,6} & 0 & 0 \\ H_{4,1} & 0 & 0 & H_{4,4} & 0 & 0 & H_{4,7} & 0 \\ 0 & H_{5,2} & 0 & 0 & H_{5,5} & 0 & 0 & H_{5,8} \\ H_{7,1} & 0 & 0 & H_{7,4} & 0 & 0 & H_{7,7} & 0 \\ 0 & H_{8,2} & 0 & 0 & H_{8,5} & 0 & 0 & H_{8,8} \end{pmatrix}.$$

By diagonalizing $\mathcal{H}_{CF}$, the energy eigenvalues and eigenfunctions of the CF levels can be deduced. The results for the CF eigenfunctions are linear combinations of the (2J+1) states in the $|J, J_z\rangle$ basis with $J_z = \pm\frac{7}{2}, \pm\frac{5}{2} \pm \frac{3}{2} \pm \frac{1}{2}$. It is impossible to obtain the CF parameters if a purely theoretical approach is taken. Additional information regarding the relative intensities of the transitions between the CF levels is needed for the determination the CF parameters. The results from INS measurements conducted on $Yb_2Ti_2O_7$ are utilized in this study to provide this information. In order to fit the relative transition intensities between the CF levels, a special form of the scattering function, $S(\mathbf{Q}, \omega)$, will be considered. For a set of CF transitions from $i' \rightarrow i''$ at a particular temperature T, $S(\mathbf{Q}, \omega)$ can be rewritten for polycrystalline samples within the **dipole approximation** [19] as given by,

$$\begin{cases} \dfrac{d^2\sigma}{d\Omega\, dE'} = C\dfrac{\mathbf{k}'}{\mathbf{k}}\, S(\mathbf{Q},\omega)\,, \\ S(\mathbf{Q},\omega) = I_0 \displaystyle\sum_{i',i''} \dfrac{\left(\displaystyle\sum_{\alpha=x,y,z} |\langle i' \mid J_\alpha \mid i'' \rangle|^2\right) \exp\left[-\mathrm{E}_{\mathrm{i}'}/(k_B T)\right]}{\displaystyle\sum_j \exp\left[-E_j/(k_B T)\right]} \times \mathrm{F}(\mathrm{E}_{\mathrm{i}'} - \mathrm{E}_{\mathrm{i}''} + \hbar\omega). \end{cases} \tag{4.2}$$

In this expression, I_0 is a constant and $\sum_{\alpha=x,y,z} |\langle i' \mid J_\alpha \mid i'' \rangle|^2$ is the sum of the square moduli of the transition matrix elements between the levels i' and i''. The function $\mathrm{F}(\mathrm{E}_{\mathrm{i}'} - \mathrm{E}_{\mathrm{i}''} + \hbar\omega)$ describes the CF transition $i' \rightarrow i''$, wherein a neutron transfers energy of $\hbar\omega$. $\mathrm{E}_{\mathrm{i}'}$ and $\mathrm{E}_{\mathrm{i}''}$ are the energy eigenvalues of the CF eigenstates $|i'\rangle$ and $|i''\rangle$, respectively. In an INS experiment, the function $\mathrm{F}(\mathrm{E}_{\mathrm{i}'} - \mathrm{E}_{\mathrm{i}''} + \hbar\omega)$ is a convolution between a Gaussian and a Lorentzian function, $\mathrm{L}_{i' \rightarrow i''}$. The former is dictated by the resolution of the spectrometer, and the latter is a function of the lifetime ($\Gamma_{i' \rightarrow i''}$) of the of the i' and i'' CF levels. One remarkable feature of the Hamiltonian $\mathcal{H}_{CF}$, is that interchanging the signs of D_4^3 and D_6^3 has no influence on the relative transition intensities or energy eigenvalues of $\mathcal{H}_{CF}$. As a result, when the transition intensities are fit to Equation (4.2) and the CF parameters are being calculated, the numerical effort is reduced two-fold.

Finally, we shall briefly discuss the signatures of CF excitations in neutron scattering spectra. CF excitations manifest themselves as dispersionless features with long lifetimes. As a result, the CF levels are typically determined by the resolution of the instrument E_r, which is related to the incident energy $E_i$by $\mathrm{E}_\mathrm{r} \sim 3\% E_i$. In addition, as CF excitations are magnetic in nature, the scattering intensity decreases as a function of $|\mathbf{Q}|$ as dictated by the magnetic form factor.

4.3 Materials Preparation and Characterization

This section is intended to provide a brief outline of the steps involved in the preparation of the two samples which were investigated. In addition, results obtained from specific heat and magnetization measurements which were conducted on these two materials are briefly discussed. One sample was prepared by solid state reactions between pressed powders of Yb_2O_3 and TiO_2. These materials were sintered at 1200° C for 24 hours, with warming and cooling rates of 100° C/hr. A second batch of pressed powder material was prepared in this manner and was used as the starting material for the single-crystal growth by the optical floating zone (OFZ) method. The details of the crystal growth process using the OFZ method are described in other literature [20–22]. The crystal growth rate was 6mm/hr and a counter-rotation of the seed and feed rods was chosen to be 30 rpm to ensure thorough mixing of the molten zone. The crystal growth was also performed under 4 atm of oxygen pressure. The powder and single-crystal samples were then each pulverized with the use of a Pulverisette 2 mortar grinder for 20 minutes. The two samples will be referred to henceforth, as the powder sample and the crushed single crystal (CSC) sample.

Collaborators Ross *et al.* conducted a structural study of these samples using the neutron powder diffraction technique. The measurements were made at the NPDF instrument at the Lujan Neutron Scattering Center at Los Alamos National Laboratory. A Rietveld refinement of their powder diffraction results showed that the CSC sample could be chemically described by the formula $Yb_2Ti_{2-x}Yb_xO_{7-\frac{x}{2}}$ with x=0.046. The structural refinement performed on the powder sample yielded a perfect or stoichiometric composition, $Yb_2Ti_2O_7$.

Consistent with specific heat measurements conducted on other powder samples of $Yb_2Ti_2O_7$, the powder sample investigated in this study shows one sharp anomaly at T = 265mK [2]. The single-crystal also showed qualitatively similar specific heat features that have been reported in other single-crystals of $Yb_2Ti_2O_7$. The CSC was found to exhibit two relatively broad anomalies. In addition, magnetization measurements were conducted on the two samples [23]. In the case of the powder sample, an effective moment of $\mu_{\text{eff}} = 3.14\mu_{\text{B}}$ was extracted and the Curie-Weiss temperature was found to be $\Theta_{\text{CW}} = 490\text{mK}$. The CSC sample exhibited a stronger effective moment, $\mu_{\text{eff}} = 3.43\mu_{\text{B}}$ by virtue of the presence of excess Yb^{3+} ions and the Curie-Weiss temperature was determined to be $\Theta_{\text{CW}} = 152\text{mK}$. In both cases, the

Curie-Weiss fits to the magnetization data were performed in the temperature range, 2K to 30K. One interesting point to note is that the Curie-Weiss temperature is positive in both cases, implying that there are overall ferromagnetic interactions. The lower Θ_{CW} found for the CSC sample however, implies that the disorder introduced due to the presence of excess Yb^{3+} ions generates behaviour that is more anti-ferromagnetic in nature. For further details on the analysis conducted on these two samples, please refer to the work conducted by Ross *et al.*[23].

4.4 Experiment Details

The inelastic neutron scattering (INS) measurements were employed at the fine resolution chopper spectrometer, SEQUOIA, at the Spallation Neutron Source at Oak Ridge National Laboratory. Roughly 12g of each of the CSC and powder samples of $Yb_2Ti_{2-x}Yb_xO_{7-\frac{x}{2}}$ were packed into aluminium cans of identical, flat-cell geometry with dimensions 50mm × 50mm × 1mm. The sample cans were sealed in a glove box that was filled with He atmosphere. An extra empty can with identical geometry and dimensions was used to obtain empty can datasets for background subtraction. The three cans were then mounted onto a rotating, three sample changer and placed into a 4K closed-cycle refrigerator. The positions of the empty can, CSC sample and powder sample were 11°, 131° and 251°, respectively. This sample holder permits easy sample changes during the experiment. When the angle corresponding to the desired sample is chosen, the sample holder rotates this sample into the ín-beampósition.

As crystal-field (CF) excitation energies of up to 70meV were expected for the powder sample, an incident energy of E_i=120meV was initially chosen. This setting has an advanatage of simultaneously yielding low resolution E_i=22meV data, permitting a simultaneous, rough view of the low energy dynamics. Following a measurement of the two samples, a higher energy scale was investigated. An instrument configuration with E_i=300meV was investigated for the possibility of additional levels occurring due the excess of Yb^{3+} ions on the B-site. Since CF levels were detected up to 116meV, an incident energy of E_i=150meV was selected. For all of the incident energies investigated, measurements were conducted on the empty can and the power and CSC samples. The settings which were used for Fermi chopper 1 (FC_1), Fermi chopper 2 (FC_2) and the (T_0) chopper, to produce neutrons of initial energy E_i=120meV, 150meV and 300meV are shown in Table 4.1.

Table 4.1: Chopper settings used in the experiment conducted on $Yb_2Ti_{2-x}Yb_xO_{7-\frac{x}{2}}$ (x=0 and x=0.046) at SEQUOIA at the Spallation Neutron Source

E_i (meV)	T_0(Hz)	FC_1(Hz)	FC_2(Hz)
120	180	300	60
150	180	60	600
300	120	300	60

4.5 Results and Discussion

4.5.1 Description of the Ground State of Yb^{3+} in $Yb_2Ti_2O_7$

This section presents the INS results obtained at SEQUOIA for the powder sample, which were used in the determination of a set of CF parameters for $Yb_2Ti_2O_7$. The results for the calculated CF parameters, ground-state wave function and components of the g-tensor of Yb^{3+} in $Yb_2Ti_2O_7$ are presented. Finally, these results are compared with the findings in earlier studies by Hodges *et al.*[12], Bertin *et al.*[7] and Malkin *et al.*[14].

The E_i=150meV INS data sets are presented in this chapter because the full set of CF excitations observed in $Yb_2Ti_2O_7$ are clearly viewable in this configuration. Figure 4.1 shows the $S(\mathbf{Q},\omega)$ contour maps obtained at T=5K and T=300K for the powder sample of $Yb_2Ti_2O_7$. In each data set presented, the appropriate empty can data sets were subtracted. In these contour plots, a strong (red) band centred at 0meV is observed. This feature corresponds to strong coherent and incoherent elastic scattering of neutrons from the sample. At higher $|\mathbf{Q}|$ positions and at energies below $\sim$ 60meV, there are dispersive excitations. These features are identified as phonons since the intensity of neutrons scattered from these features increase as a function of $|\mathbf{Q}|$.

The result obtained at T=5K shows two strong, dispersionless excitations located at $\sim$ 80meV and a third weak, dispersionless excitation located at $\sim$ 115meV. These excitations correspond to the three excited doublets expected for the Yb^{3+} ion in $Yb_2Ti_2O_7$. One feature of these excitation modes which point to their magnetic nature is the decrease of the neutron scattering intensity as a function of $|\mathbf{Q}|$. This behaviour reflects the $|\mathbf{Q}|$ dependence of the magnetic form factor. At T=300K, although these CF excitations are still visible, the population of each these CF levels is lower in comparison to their population at T=5K. This is behaviour is expected at 300K since the ground-state is less populated and the transition probability between the ground-state to any of the excited doublets will consequently decrease. As the neutron scattering intensity is directly related to the transition probability between the CF

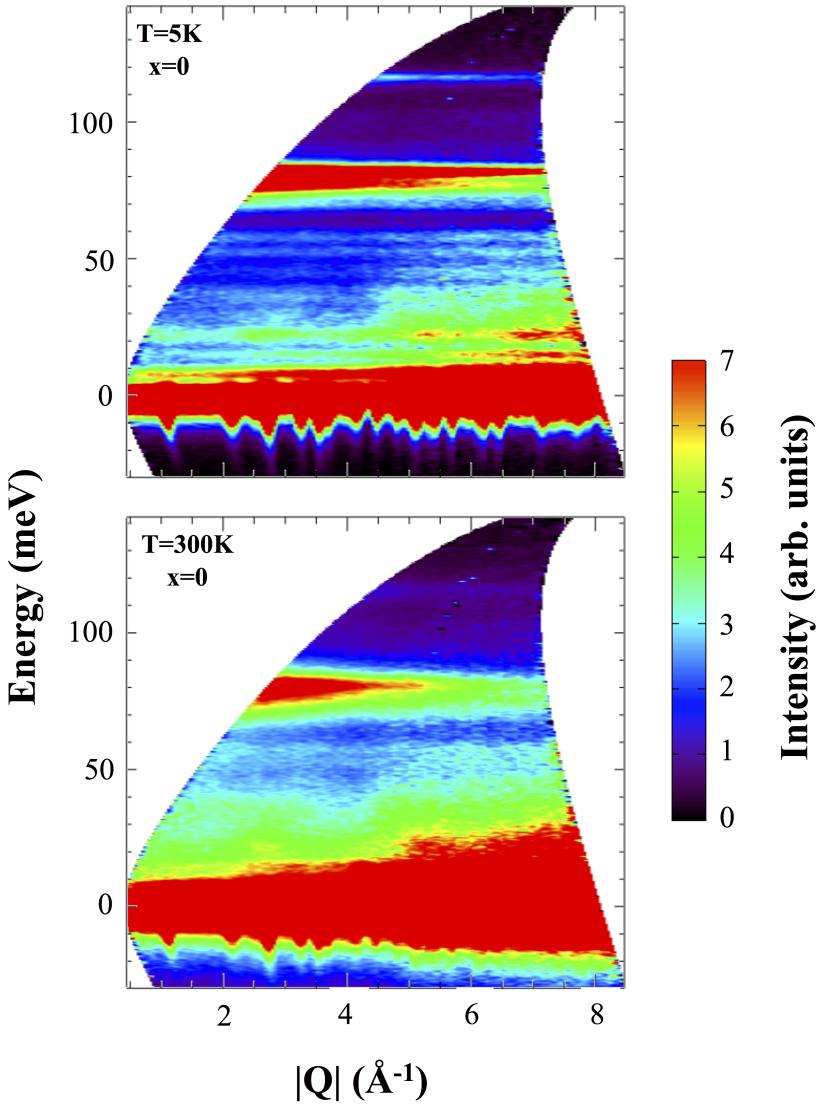

Figure 4.1: (a)$S(\mathbf{Q},\omega)$ contour maps obtained at E_i=150meV for the powder sample of $Yb_2Ti_2O_7$ at 5K. (b)$S(\mathbf{Q},\omega)$ contour maps obtained at E_i=150meV for the powder sample of $Yb_2Ti_2O_7$ at 300K.

levels, this temperature dependence should be expected.

As mentioned earlier, the first two excited doublets are near 80meV. In order to fully resolve these separate excitations, $|\mathbf{Q}|$ integrated cuts were taken in the range $|\mathbf{Q}| = [4.48, 5.28]\text{Å}^{-1}$, as shown in Figure 4.2. The temperature and sample dependence of the $|\mathbf{Q}|$ integrated cuts are shown in panels (a)-(d). As equal masses of the powder and CSC samples were utilized, the results obtained for both samples can be directly compared. In order to permit comparisons between the relative intensities of the excitations in the powder and CSC samples, the neutron scattering intensities measured for both samples were scaled by the maximum intensity observed in all of the data sets. As the range of integration captures all three CF levels, these cuts were also utilized in the fits of the relative transition intensities for the determination of the CF parameters. The results which are presented in Figure 4.2 also show the fits (in solid lines) to the neutron scattering intensities at 5K and 300K for the powder and CSC samples.

Before discussing the fit procedure and results, some striking differences between the observed intensities in the energy cuts for the two samples at 5K and 300K are highlighted. In Figure 4.2, panels (a)-(b) illustrate the effect of sample stuffing at 5K. The CF excitations from the powder sample are manifested as sharper features compared with the CF levels measured in the CSC sample. The 300K data sets which are presented in panels (c)-(d), reveal the strong temperature dependence of the CF excitations in the powder and CSC samples. The overall peak intensity in both samples decrease dramatically by a factor of ~ 0.6. In addition, the CF excitations are broadened as a function of temperature and the position of the maximum intensity shifts by ~ 0.6meV.

Now we shall turn our attention to the details of the fitting procedure. The fit was conducted first, on the T=5K energy cut of the powder sample presented in panel (a) in Figure 4.2. The lifetime Γ of the CF excitations were initially set to roughly 3% of E_i=150meV in the fitting algorithm. The six CF parameters were then fit to match to neutron scattering intensities measured for the powder sample at T=5K. Once the CF parameters were optimized, these values were set in the fitting algorithm and the value of Γ was subsequently optimized. The fit results yielded the set of CF parameters which are shown in Table 4.2 and the lifetime of the CF excitations were determined to be $\Gamma = 3.9$meV for the powder sample at 5K.

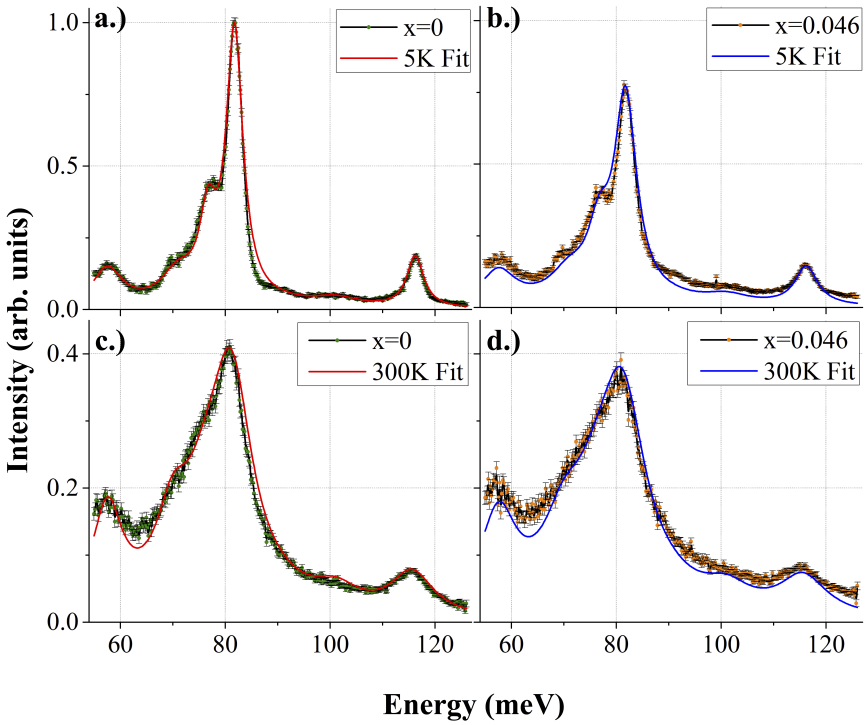

Figure 4.2: Energy cuts taken from the 150meV data sets on the samples $Yb_2Ti_2O_7$ and $Yb_2Ti_{2-x}Yb_xO_{7-\frac{x}{2}}$ (x=0.046) samples at T=5K and T=300K. The integration was performed over the range $|\mathbf{Q}| = [4.48, 5.28]\text{Å}^{-1}$. The intensities shown in the energy cuts are normalized to the peak intensity observed in the powder sample at 5K within the range of energy transfer shown.

The optimized CF parameters (given in Table 4.2) were fixed for the fits performed on the energy cuts of the the T=300K powder data sets and the T=5K and T=300K CSC data sets. When the fits to the T=300K energy cuts were conducted, the positions of the CF levels were shifted by ~ 0.6meV in order to match the position of the maximum transition intensity which was observed. As can be seen in panels (a)-(d), the fit parameters provide an excellent description of the observed transition intensities. The lifetime Γ, obtained for the powder sample at 300K was found to be 9.9meV. The lifetimes obtained from the fit to the T=5K and T=300K data sets of the CSC sample were 5.2meV and 11meV, respectively.

As the CF parameters for Yb^{3+} in $Yb_2Ti_2O_7$ were determined in the previous step, the energy eigenfunctions and corresponding energy eigenvalues can be found by diagonalizing the CF Hamiltonian, $\mathcal{H}_{CF}$. These results are summarized in Table 4.3 and compared with the results which were obtained from other studies. The first

column of Table 4.3 comprises the energy eigenvalues, and the subsequent columns show the contributions from each $|J_z\rangle$ state. Of particular interest in this study, is the description of the ground state wave function of Yb^{3+} in $Yb_2Ti_2O_7$. The ground state wave function $\phi^{\pm}$, can be described by the superposition of the $|J_z\rangle$ states as shown below.

$$\begin{aligned}\left|\phi^{\pm}\right\rangle = \pm 0.022\left|\mp\frac{7}{2}\right\rangle - 0.086\left|\mp\frac{5}{2}\right\rangle - 0.056\left|\mp\frac{1}{2}\right\rangle \\ \mp 0.923\left|\pm\frac{1}{2}\right\rangle \pm 0.005\left|\pm\frac{5}{2}\right\rangle - 0.361\left|\pm\frac{7}{2}\right\rangle .\end{aligned} \tag{4.3}$$

As expected, the $\left|J_z = \pm\frac{1}{2}\right\rangle$ state predominantly contributes to the ground state wave function, $\phi^{\pm}$. This result is comparable with those which were obtained in earlier studies [7, 12], wherein the dominant contribution to the ground state was from the state, $\left|J_z = \pm\frac{1}{2}\right\rangle$. Table 4.3 also shows that the eigenfunction corresponding to the 81.76meV excitation, is the most pure state. This eigenfunction is heavily weighted by the $\left|J_z = \pm\frac{3}{2}\right\rangle$ state. It is correspondingly, the strongest CF excitation which was measured in the study.

Table 4.2: A comparison of crystal-field parameters obtained for $Yb_2Ti_2O_7$ in this study with parameters obtained in other work.

	D_2^0(meV)	D_4^0meV	D_4^3	D_6^0(meV)	D_6^3(meV)	D_6^6(meV)
This work	35.75	35.51	181.91	7.29	-250.00	33.45
Bertin *et al.* [7]	27.41	27.72	248.33	4.46	-73.65	60.54
Hodges *et al.* [12]	33.64	8.84	338.42	4.08	-27.25	31.31

Table 4.3: The calculated energy eigenvalues and eigenfunctions for $Yb_2Ti_2O_7$ are shown. The eigenstates are given in terms of the J_z basis states with $\boldsymbol{J} = \frac{7}{2}$

Energy (meV)	$\left\|-\frac{7}{2}\right\rangle$	$\left\|-\frac{5}{2}\right\rangle$	$\left\|-\frac{3}{2}\right\rangle$	$\left\|-\frac{1}{2}\right\rangle$	$\left\|\frac{1}{2}\right\rangle$	$\left\|\frac{3}{2}\right\rangle$	$\left\|\frac{5}{2}\right\rangle$	$\left\|\frac{7}{2}\right\rangle$
0	0.022	-0.086	0	-0.056	-0.927	0	0.005	-0.361
0	-0.361	-0.005	0	0.927	-0.056	0	-0.086	-0.022
76.71	-0.911	-0.017	0	-0.333	-0.025	0	0.231	0.068
76.71	0.068	-0.231	0	0.025	-0.333	0	-0.017	0.911
81.76	0	0	0.218	0	0	0.976	0	0
81.76	0	0	-0.976	0	0	0.218	0	0
116.24	-0.181	-0.227	0	-0.158	0.038	0	-0.942	-0.044
116.24	0.044	-0.942	0	0.038	0.158	0	0.227	-0.181

The Landé g-factors were also calculated according to the relations given in Equation (4.4). In this definition, $g_{\parallel} = g_z$, wherein the z-axis lies along the [111] direction. The calculated values for the components of the g-tensor are $g_{\parallel} = 1.10$ and $g_{\perp} = 3.74$. The predicted values of $g_{\parallel}$ reported in other work by Cao *et al.*[17], Hodges *et al.*[12] and Bertin *et al.*[7] are higher than the value obtained in this study. The value of $g_{\parallel} = 1.79$ which was reported by Hodges *et al.*[12], is closest to the value obtained in this study.

$$\begin{cases} g_{\parallel} = 2g_J \left| \left\langle \phi^{\pm} \right| J_z \left| \phi^{\pm} \right\rangle \right|, \\ g_{\perp} = g_J \left| \left\langle \phi^{+} \right| J_+ \left| \phi^{-} \right\rangle \right| = g_J \left| \left\langle \phi^{-} \right| J_- \left| \phi^{+} \right\rangle \right| \end{cases} \tag{4.4}$$

Up for final discussion in this section are comparisons between the energy eigenvalues which were determined in this study and in the optical spectroscopy study by Malkin *et al.*[14]. It must be noted that the optical spectroscopy measurements however, did not detect the lowest lying CF excitation in $Yb_2Ti_2O_7$. The CF parameters which were determined in the study by Malkin *et al.*, estimated the position of the lowest lying CF excitation to be ~ 60meV. The parameters obtained in that study therefore, do not provide a proper description of the lowest lying excitation in $Yb_2Ti_2O_7$. The CF parameters obtained in this study therefore, provide a better description of the CF energy scheme of $Yb_2Ti_2O_7$.

4.5.2 Effect of Stuffing on the Crystal-Field Spectrum of $Yb_2Ti_2O_7$

The INS neutron scattering data sets which were obtained for the powder and CSC samples can be visualized in an alternate way, in order to directly compare the effects of stuffing on the CF spectrum of $Yb_2Ti_2O_7$. Since mass normalization is already accounted for, it is appropriate to perform direct subtractions between data sets obtained for the CSC and powder samples. Performing these direct subtractions will enable the detection of any small differences in the INS spectra due to sample stuffing.

$S(\mathbf{Q},\omega)$ energy contour maps are presented in Figure 4.3, wherein the data sets obtained from the powder sample were subtracted from the data sets obtained for the CSC sample. Figure 4.3 shows the difference in the two data sets obtained at T=5K and T=300K. The scale representing neutron scattering intensity was extended to the negative intensity range, in order to show any features in which the powder sample displays stronger scattering in comparison to the CSC sample. Excesses of scattering are mostly observed in the case of the CSC. Just above the elastic line however, there is more scattering emanating from the powder sample. At $\sim$ 80meV the black strip corresponds to the relatively higher intensity of the first and second CF excitations which were observed in the powder sample. Just above this feature near 90meV, there is a strong excess of scattering which is present due to the broadening of the CF levels, which is caused by the excess of Yb^{3+} ions present in the CSC sample. Since this effect is magnetic in nature, it is expected to exhibit a strong $|\mathbf{Q}|$ dependence which is similar to the $|\mathbf{Q}|$ dependence of the magnetic form factor. An energy integrated cut was therefore taken in the region E=[80,90]meV to extract the $|\mathbf{Q}|$ dependence of this feature. Figure 4.4 (b) shows the result of taking these energy integrated cuts on the T=5K and T=300K data sets which are presented in Figure 4.3. Indeed, the intensity of scattered neutrons decreases as a function of $|\mathbf{Q}|$ and the scattering is weaker at higher temperature.

The features near 40meV and 65meV spark some curiousity because of the enhancement sample differences at lower temperature. To further investigate these features, energy integrated cuts are taken in the range E=[35,45]meV and E = [60,70]meV as shown in Figure 4.5 and Figure 4.6, respectively. A clear enhancement of intensity is observed as temperature decreases in both cases. This feature can signal the magnetic nature of these small differences observed. In contrast to the 90meV feature discussed previously, these features do not exhibit a strong magnetic form-fact like, $|\mathbf{Q}|$ dependence. In addition, $|\mathbf{Q}|$ integrated cuts were also performed on the differences

between the CSC sample and the powder sample data sets. A $|\mathbf{Q}|$ integrated cut was performed in the range $|\mathbf{Q}| = [3, 4.2]\text{Å}^{-1}$. This low $|\mathbf{Q}|$ integration range is more sensitive to magnetic features, which are pronounced at lower $|\mathbf{Q}|$ positions. The resulting cuts performed on the T=5K and T=300K data sets are shown in Figure 4.7. As can be seen in the inset of Figure 4.7, there are two broad peaks which are observed in the T=5K data set, which are located near 45meV and 65meV. This indicates an excess of scattering in the CSC, which is enhanced as the temperature decreases. This is expected for the feature near 65meV because the presence of the excess Yb^{3+} ions tends to broaden the CF levels. As the CF levels are magnetic in nature, this effect should be enhanced at lower temperatures. The nature of the enhancement of the scattered intensity in the CSC at low temperatures at 45meV, is still open to question. What can be said with certainty however, is that the disorder induced by the excess of Yb^{3+} ions is responsible for this effect.

The energy integration range considered in the first cut fails to capture features at higher energy. Therefore, a second $|\mathbf{Q}|$ integrated cut was performed within a higher $|\mathbf{Q}|$ -range, $|\mathbf{Q}| = [4.48, 5.28]\text{Å}^{-1}$. The temperature dependence of the cuts obtained from the differences between the CSC and powder sample data sets are presented in Figure 4.8. The inset of Figure 4.8 indicates excesses of scattering from the CSC sample. This feature can be attributed to the broadening of the doublet near 80meV, which is induced due to the presence of excess Yb^{3+} ions. These differences between the CSC and powder samples are enhanced as temperature decreases. A similar effect is observed near the third excited CF doublet near 120meV.

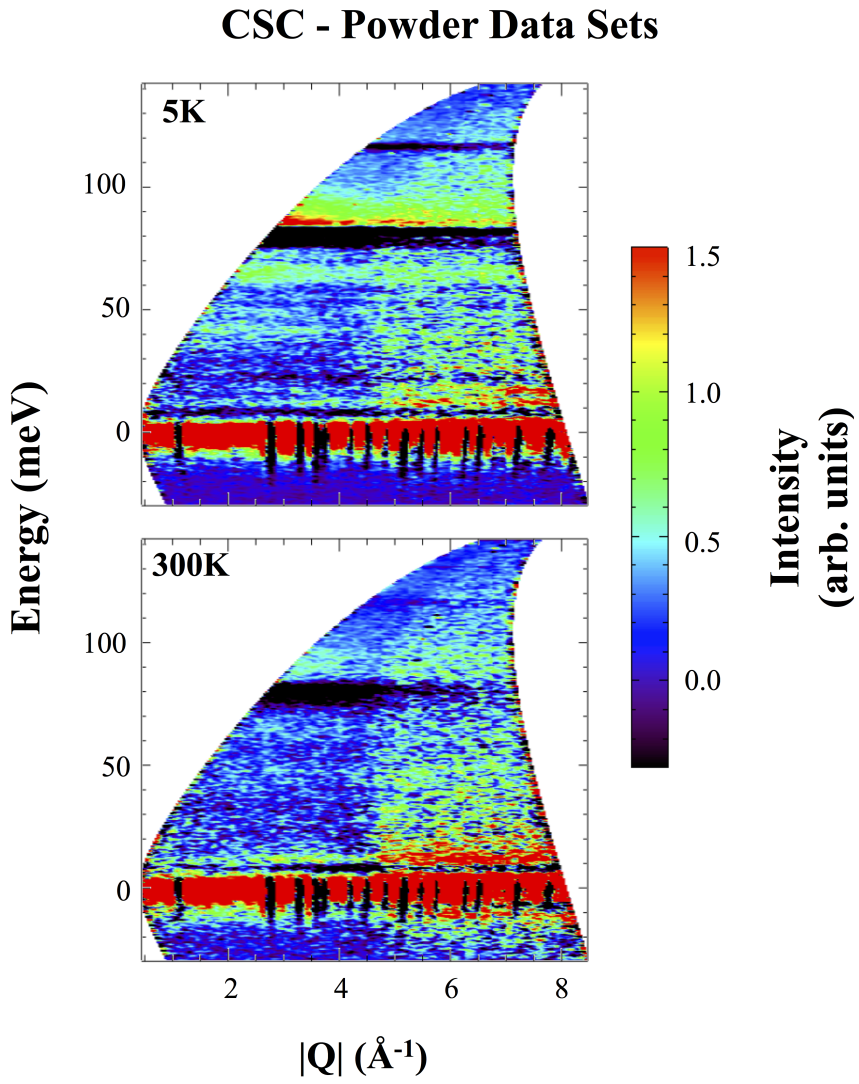

Figure 4.3: $S(\mathbf{Q},\omega)$ contour maps obtained at E_i=150meV showing the powder data sets subtracted from the CSC data sets at 5K and 300K.

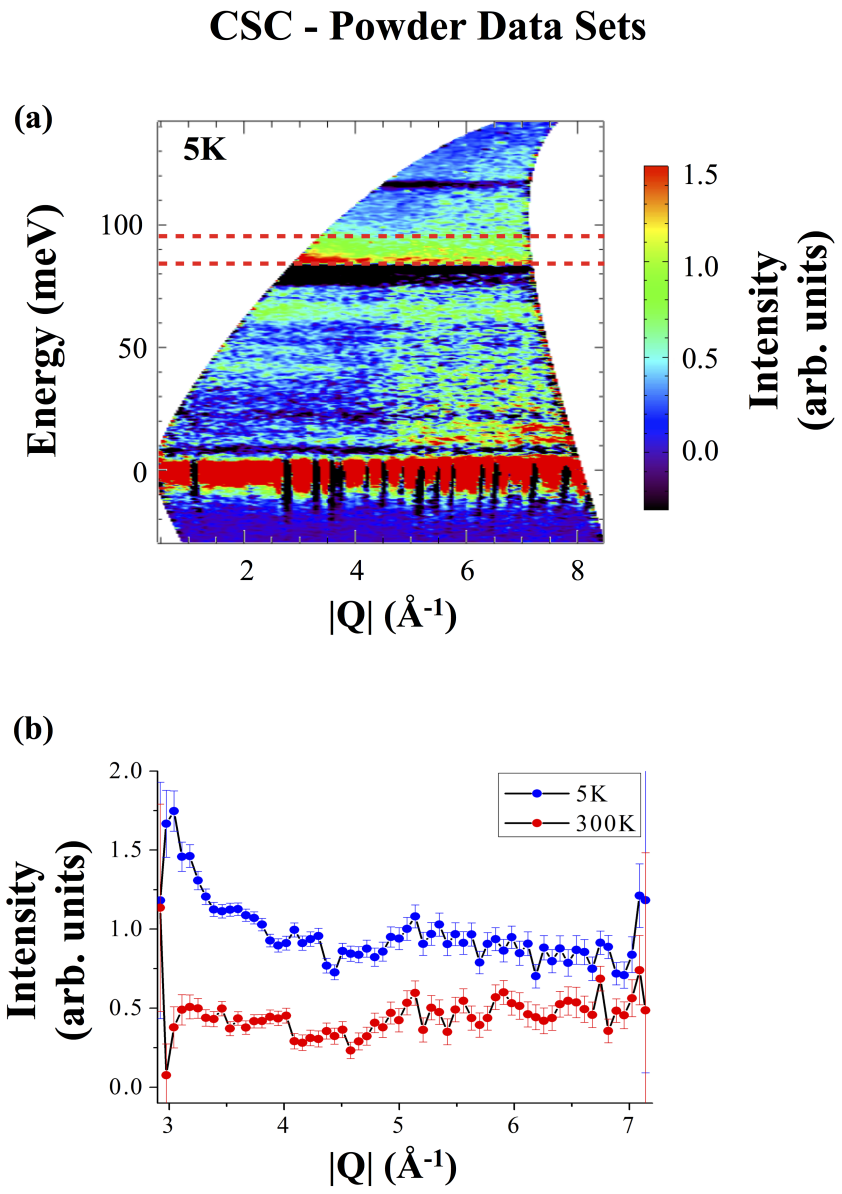

Figure 4.4: (a)$S(\mathbf{Q},\omega)$ contour map corresponding to the T=5K data set presented in Figure 4.3. The energy integration range of E=[84,94]meV is illustrated. (b) The resulting $|\mathbf{Q}|$-cuts taken with an energy integration range of E=[84,94]meV from the T=5K and T=300K data sets which are presented in Figure 4.3, are shown.

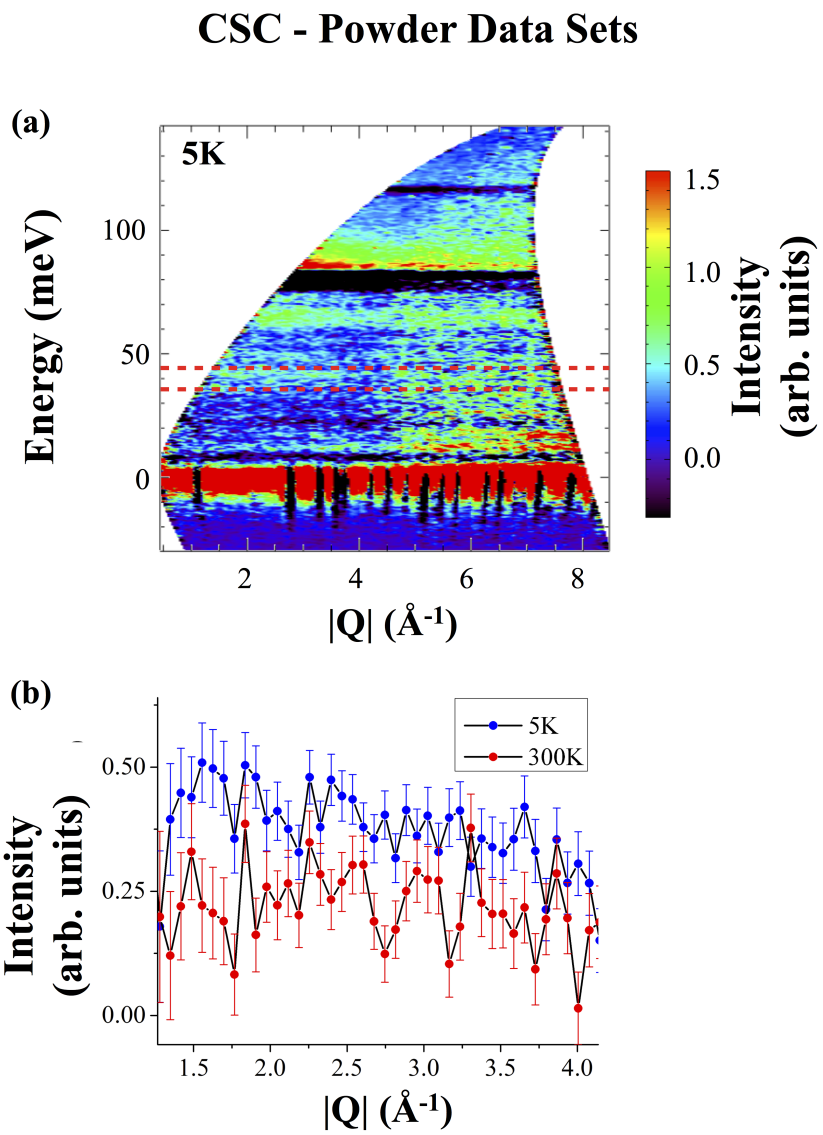

Figure 4.5: (a)$S(\mathbf{Q},\omega)$ contour map corresponding to the T=5K data set presented in Figure 4.3. The energy integration range of E=[35,45]meV is illustrated. (b) The resulting $|\mathbf{Q}|$-cuts taken with an energy integration range of E=[35,45]meV from the T=5K and T=300K data sets which are presented in Figure 4.3, are shown.

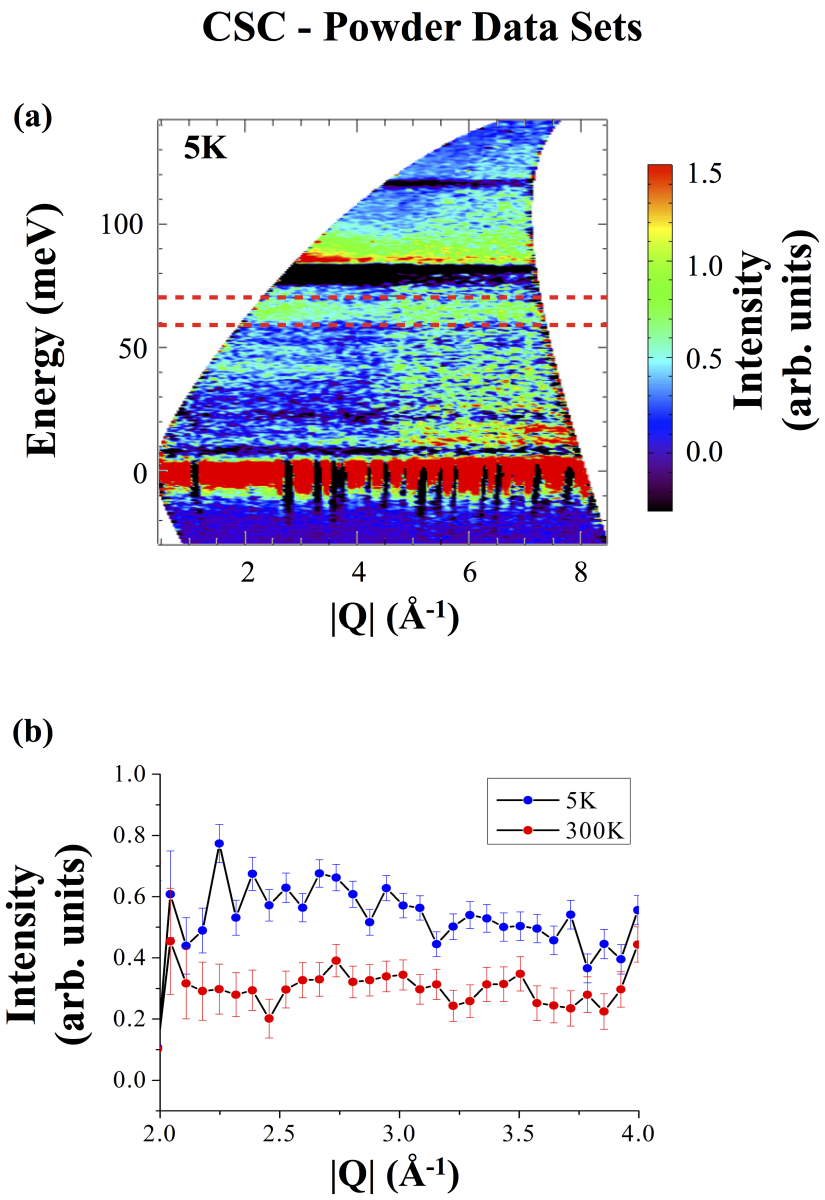

Figure 4.6: (a)$S(\mathbf{Q},\omega)$ contour map corresponding to the T=5K data set presented in Figure 4.3. The energy integration range of E=[60,70]meV is illustrated. (b) The resulting $|\mathbf{Q}|$-cuts taken with an energy integration range of E=[60,70]meV from the T=5K and T=300K data sets which are presented in Figure 4.3, are shown.

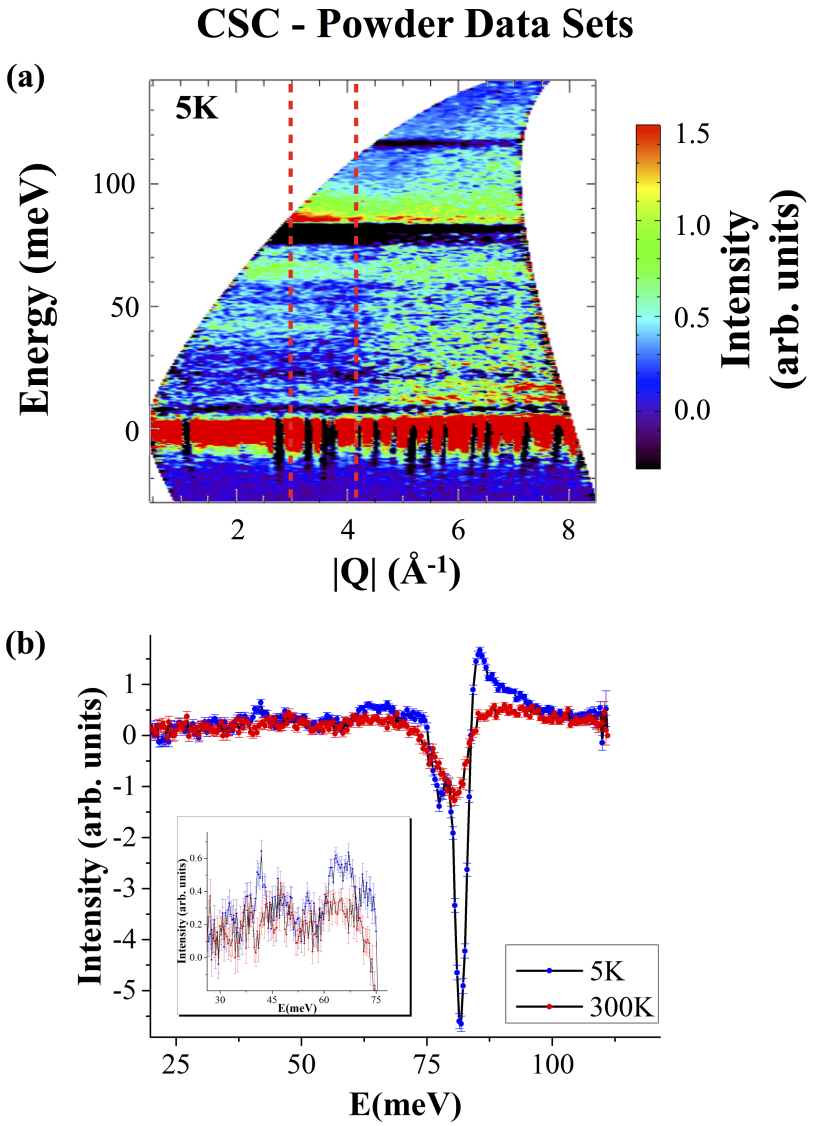

Figure 4.7: (a)$S(\mathbf{Q},\omega)$ contour map corresponding to the T=5K data set presented in Figure 4.3. The $|\mathbf{Q}|$ integration range of $|\mathbf{Q}| = [3, 4.2]\text{AA}^{-1}$ is illustrated. (b) The resulting energy cuts taken with an $|\mathbf{Q}|$ integration range of $|\mathbf{Q}| = [3, 4.2]\text{AA}^{-1}$ from the T=5K and T=300K data sets which are presented in Figure 4.3, are shown.

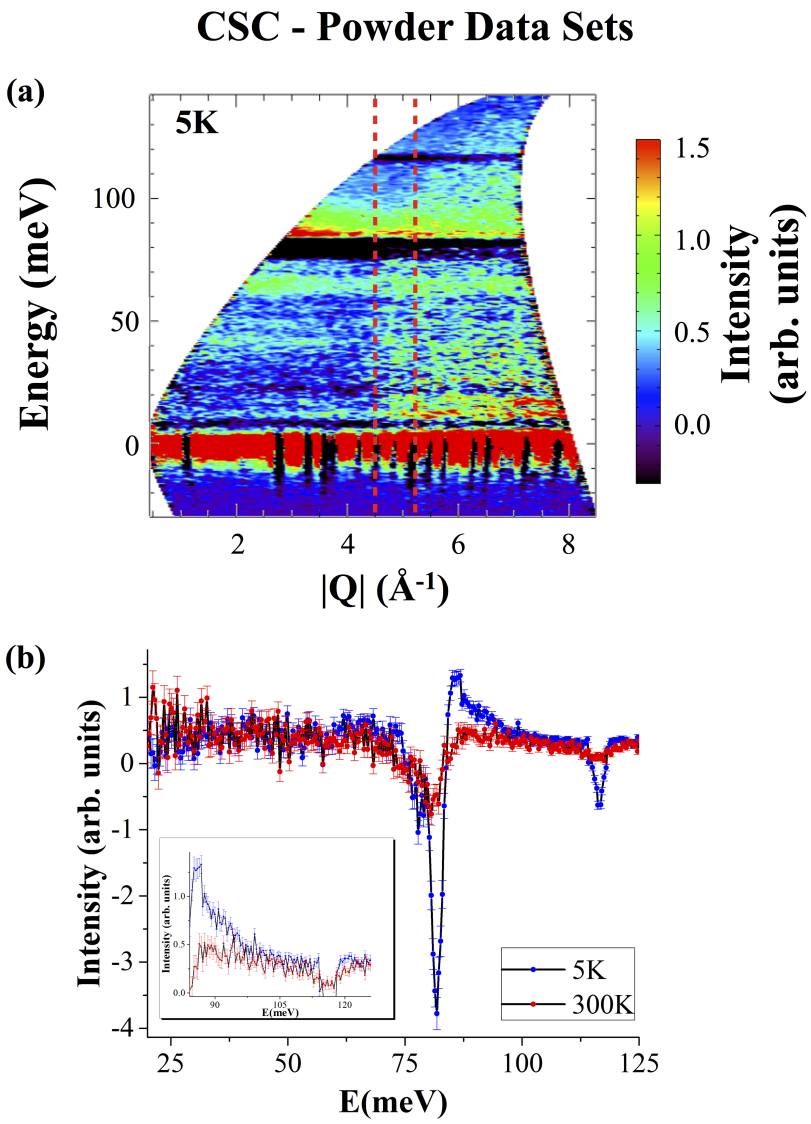

Figure 4.8: (a)$S(\mathbf{Q},\omega)$ contour map corresponding to the T=5K data set presented in Figure 4.3. The $|\mathbf{Q}|$ integration range of $|\mathbf{Q}| = [4.48, 5.28]\text{AA}^{-1}$ is illustrated. (b) The resulting energy cuts taken with an $|\mathbf{Q}|$ integration range of $|\mathbf{Q}| = [4.48, 5.28]\text{AA}^{-1}$ from the T=5K and T=300K data sets which are presented in Figure 4.3, are shown.

4.6 Conclusions

Figure 4.9 shows the crystal-field (CF) spectrum obtained for $Yb_2Ti_2O_7$ from inelastic neutron scattering (INS) measurements conducted at SEQUOIA at the Spallation Neutron Source. A set of unique CF parameters were obtained from fits to the transition intensities which were measured for $Yb_2Ti_2O_7$ at T=5K. These CF parameters are provided in Table 4.2. To our best knowledge, these are the only set of CF parameters which correctly describe the positions of CF excitations in $Yb_2Ti_2O_7$. The ground state wave function, $\phi^{\pm}$, of the Yb^{3+} ion was determined as shown below,

$$\begin{aligned}\left|\phi^{\pm}\right\rangle = \pm 0.022\left|\mp\frac{7}{2}\right\rangle - 0.086\left|\mp\frac{5}{2}\right\rangle - 0.056\left|\mp\frac{1}{2}\right\rangle \\ \mp 0.923\left|\pm\frac{1}{2}\right\rangle \pm 0.005\left|\pm\frac{5}{2}\right\rangle - 0.361\left|\pm\frac{7}{2}\right\rangle .\end{aligned} \tag{4.5}$$

Calculations of the components of the g-tensor yielded $g_{\parallel} = 1.10$ and $g_{\perp} = 3.74$. The data sets obtained at T=5K and T=300K for the CSC sample clearly showed the three crystal-field excitations associated with the *A*-site. The neutron scattering intensities associated with transitions occurring from the ground state to the higher lying CF levels corresponding could be well fit by the CF parameters obtained for the powder sample. The lifetimes, which were determined from the fits show a remarkable broadening effect which is induced due to the presence of a small excess ($\sim 2\%$) of Yb^{3+} ions.

In addition, direct subtractions between the data sets corresponding to the powder and CSC sample were performed at T=5K and T=300K. $|\mathbf{Q}|$ and energy integrated cuts revealed the presence of excess scattering from the CSC sample, near the positions of the CF energy eigenmodes and near 40meV. These features are all enhanced with decreasing temperature, suggesting the possibility of their magnetic origin. The features near the positions of the CF energy eigenmodes occur due to broadening of the CF levels which is induced due to the presence of the excess Yb^{3+} ions. The excess of scattering which is exhibited by the CSC at 40meV has not been yet explained. Although the nature of this excitation is not yet understood, one possible explanation is that it is a CF excitation that is associated with the excess of Yb^{3+} ions in $Yb_2Ti_2O_7$ at the *B*-site.

Future work involves future investigation of these samples at lower E_i , to better

resolve the lower energy features and to confirm the presence of these modes. Higher incident energies can also be chosen to search for the possibility of the existence of modes of higher energy associated with Yb^{3+} ions at the Ti^{4+} site.

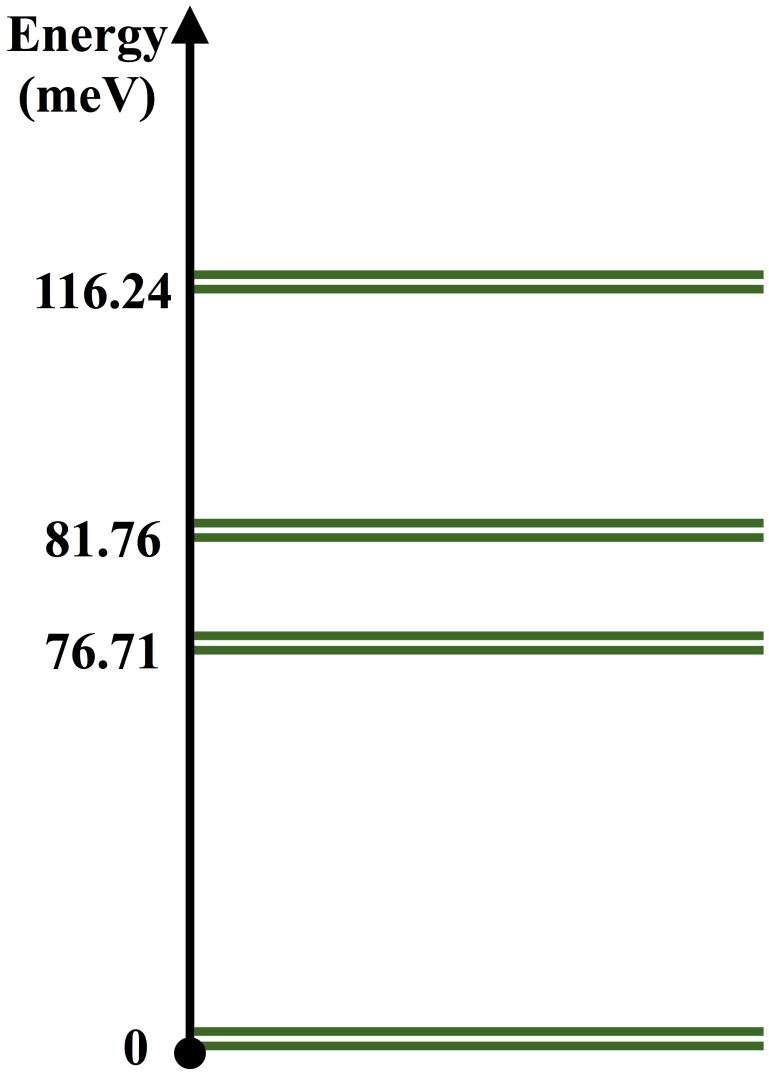

Figure 4.9: The crystal-field splitting scheme which was determined for $Yb_2Ti_2O_7$ from time-of-flight inelastic neutron scattering measurements conducted at SEQUOIA, is shown.

Bibliography

[1] L. Savary and L. Balents. *Phys. Rev. B*, 87(205130), 2013.

[2] K.A. Ross, L.R. Yaraskavitch, M. Laver, J.S. Gardner, J.A. Quilliam, S. Meng, J.B. Kycia, Th. Proffen, H.A. Dabkowska, and B.D. Gaulin. *Phys. Rev. B*, 84(174442), 2011.

[3] M.T. Hutchings. *Solid State Physics, Advances in Research and Applications*, volume 16. Academic Press, 1964.

[4] J. Jensen and A.R. Mackintosh. *Rare Earth Magnetism: Structures and Excitations*. Oxford, Clarendon, 1991.

[5] G.H. Dieke. *Spectra and Energy Levels of Rare Earth Ions in Crystals*. Interscience Publishers, 1969.

[6] J. Zhang, K. Fritsch, B.V. Bagheri, M.J.P. Gingras, G.E. Granroth, P. Jiramongkolchai, R.J. Cava, and B.D. Gaulin. *Phys. Rev. B*, 89(134410), 2013.

[7] A. Bertin, Y. Chapuis, P. Dalmas de Réotier, and A. Yaouanc. *J. Phys. Condens. Matter*, 24(256003), 2012.

[8] A.J. Princep, D. Prabhakaran, and A.T. Boothroyd. *Phys. Rev. B*, 88(104421), 2013.

[9] J.S. Gardner and G. Ehlers. *J. Phys. Condens. Matter*, 21(436004), 2009.

[10] I. Mirebeau, P. Bonville, and M. Hennion. *Phys. Rev. B*, 76(184436), 2007.

[11] M.P. Zinkin, M.J. Harris, Z. Tun, R.A. Cowley, and B.M. Wanklyn. *J. Phys.: Condens. Matter*, 8:193–197, 1996.

[12] J.A. Hodges, P. Bonville, A. Forget, M. Rams, K. Królas, and G. Dhalenne. *J. Phys.: Condens. Matter*, 13:9301–9310, 2001.

[13] S. Rosenkranz, A.P. Ramirez, A. Hayashi, R.J. Cava, R. Siddharthan, and B.S. Shastry. *J. Appl. Phys.*, 87(9), 2000.

[14] B.Z. Malkin, A.R. Zakirov, M.N. Popova, S.A. Klimin, E.P. Chukalina, E. Antic-Fidancev, Ph. Goldner, P. Aschehoug, and G. Dhalenne. *Phys. Rev. B*, 70(075112), 2004.

[15] A. Sengupta, J. Jana, and D. Ghosh. *J. Phys. Chem. Solids*, 60:331–336, 1999.

[16] R. Siddharthan, B.S. Shastry, A.P. Ramirez, A. Hayashi, R.J. Cava, and S. Rosenkranz. *Phys. Rev. Lett.*, 83(9), 1999.

[17] H. Cao, A. Gukasov, I. Mirebeau, C. Decorse, and G. Dhalenne. *Phys. Rev. Lett.*, 103(056402), 2009.

[18] B.Z. Malkin. *Spectroscopy of Solids Containing Rare Earth Ions*. North Holland, Amsterdam, 1987.

[19] P. Fulde and M. Loewenhaupt. *Spin Waves and Magnetic Excitations*. Elsevier, Amsterdam, 1988.

[20] H.A. Dabkowska and A.B. Dabkowski. *Springer Hanbdbook of Crystal Growth*. Springer, Berlin, 2010.

[21] S.M. Koohpayeh, D. Fort, and J.S. Abell. *Prog. Cryst. Growth Charac. Mater.*, 54(121), 2008.

[22] G. Balakrishnan, M. Paul, M.R. Lees, and A.T. Boothroyd. *Physica C: Supercond.*, 206(148), 1993.

[23] K.A. Ross, Th. Proffen, H.A. Dabkowska, J.A. Quilliam, L.R. Yaraskavitch, J.B. Kycia, and B.D. Gaulin. *Phys. Rev. B*, 86(174424), 2012.

Chapter 5

Spin-Orbit Driven Phenomena in the FCC Anti-Ferromagnet Ba_2YOsO_6

5.1 Background

In this chapter, time-of-flight (TOF) neutron scattering and triple-axis measurements which were conducted on the face-centred cubic (FCC) anti-ferromagnet Ba_2YOsO_6 are presented. The TOF measurements were conducted at the Spallation Neutron Source (SNS) at Oak Ridge National Laboratory, while triple-axis measurements were conducted at Canadian Neutron Beam Centre (CNBC) at Chalk River National Laboratories. The purpose of this study is to understand the role of strong spin-orbit effects on the low temperature behaviour of this system. As there is pre-existing work on compounds containing heavy 4d and 5d ions in the $A_2BB'O_6$ series, these results are part of a broader pursuit to understand the role of spin-orbit coupling in the low temperature behaviour of these FCC double perovskites. In particular, Ba_2YRuO_6 is the $4d^3$ analogue to the $5d^3$ system Ba_2YOsO_6. Both compounds are iso-structural and share similar lattice parameters. Therefore, any direct comparison made between these two compounds would arise from the difference between the magnetic properties of the ions. As both compounds are d^3 systems, the major difference between them lies in the size of the magnetic ion, Z. First, we shall briefly consider the low temperature properties already reported in Ba_2YRuO_6 in order to provide some inspiration for the study of Ba_2YOsO_6.

Ba_2YRuO_6 was previously investigated with the TOF inelastic neutron scattering,

neutron diffraction and ^{89}Y NMR techniques [1, 2]. In addition, dc susceptibility and heat capacity meaurements on this system were also reported in a study by Aharen *et al* [2]. The magnetic susceptibility measurements revealed two broad peaks at T = 37K and T = 47K, and a large, negative Curie-Weiss temperature of -522K was determined for this system [2]. Heat capacity measurements and neutron diffraction data taken at numerous temperatures gave evidence for an anti-ferromagnetic transition at $T_N = 36$K in Ba_2YRuO_6. In a later investigation by Carlo *et al.*, results from TOF inelastic neutron scattering measurements conducted on Ba_2YRuO_6 were reported. This study found evidence for the existence of two phases, with the development of an unexpected $\sim$ 5meV spin-gap below $T_N = 36$K and long-range order (LRO) below $T^* = 45$K [1]. In this same study, despite the large θ_{CW}, spin waves of relatively small bandwith $\sim$ 14meV were found.

This result is intriguing because a gap is not expected for Ba_2YRuO_6. In the absence of spin-orbit effects for an orbitally quenched $s = \frac{3}{2}$ spin-only moment, anisotropy is minimized and one should not expect the development of a gap. The question here is whether spin-orbit is the driving mechanism of this novel behaviour. This study on Ba_2YOsO_6 therefore seeks to address this hypothesis.

Ba_2YOsO_6 is a good choice for comparison with Ba_2YRuO_6 as the relatively larger size of the Os^{5+} ion would enhance spin-orbit effects, which grow as $\sim Z^4$. If an enhanced gap is measured in the 5d system, then we can arguably attribute this feature to spin-orbit effects. Is spin-orbit indeed, the driving factor in this unexpected low temperature behaviour? Our results suggest that spin-orbit effects are likely the origin of this behaviour and shall be presented in the following sections. Before proceeding to discuss the original inelastic neutron scattering measurements and triple-axis work done on Ba_2YOsO_6, some key background information on the sample provided by collaborators are summarized.

5.2 Sample Characterization

$Ba_4Y_2O_7$ was prepared from stoichiometric amounts of $BaCO_3$ and Y_2O_3 fired at 1000° C in air for 24 hours. The stoichiometric sample was then prepared by a solid state reaction according to Equation (5.1) at 1400° C for 1.5 hours in a Pt crubile, with one regrinding after 30 minutes.

$$Ba_4Y_2O_7 + 2Os\ (10\%\ \text{excess}) = \frac{5}{2}O_2 + 2Ba_2YOsO_6 \tag{5.1}$$

An analysis of the neutron powder diffraction data of this sample indicated the presence of a small amount ($\sim 5\%$ of the sample mass) of a weak ferromagnetic impurity phase which was identified as $Ba_{11}Os_4O_{24}$. Since this phase orders feromagnetically at 6.8K, this does not interfere with any results obtained for Ba_2YOsO_6. In addition, the lattice parameter was refined as $a = 8.3541$Å and no evidence was found for B/B' anti-site disorder.

However, magic spinning angle (MAS) NMR is a more sensitive probe which can be used to check for B/B' anti-site disorder as demonstrated in previous studies [2–4]. The levels of anti-site disorder were determined to be less than 0.5% since the signal due to any disorder was below the level of the noise in the measurement.

Magnetization measurements were performed between 2K and 300K and only one clear anomaly was observed in χ(T) at $T_N = 68$K. This is in contrast to the cases of Ba_2YRuO_6 and another related double perovskite, Sr_2YRuO_6, for which there are two reported transition temperatures [1, 2, 5]. The magnetization data obtained for Ba_2YOsO_6 was fitted to Curie-Weiss behaviour between 150 and 300K. This resulted in a very large, negative Curie-Weiss temperature, $\theta_{CW} = -772(4)$K, which is indicative of anti-ferromagnetic interactions. As defined in Chapter 1, the frustration index was determined to be $f = |\theta_{CW}|/T_N \sim 11$. The effective moment was also extracted and estimated to be $\mu_{eff} = 4.15\mu_B$.

Neutron diffraction measurements were conducted on Ba_2YOsO_6 between 75K and 3K. The results from this measurement revealed magnetic structural peaks consistent with a Type I anti-ferromagnetic FCC structure as was previously found for Ba_2YRuO_6 [2, 6]. The refined magnetic moment at the Os^{5+} site was found to be $1.65(6)\mu_B$ and is smaller than what is expected for the $s = \frac{3}{2}$ spin-only moment of $3\mu_B$.

5.3 Experiment Details

5.3.1 Time-of-flight Neutron Spectroscopy

Approximately 8g of a polycrystalline sample of Ba_2YOsO_6 was packed into a sample can. The aluminium sample can was of flat cell geometry with dimensions 50mm × 50mm × 1mm. The sample can was sealed with indium wire in a glove box containing He gas maintained at 2atm. An additional can with identical geometry and dimensions was used to obtain empty can data sets for background subtraction. Measurements were first conducted on the sample, and empty can measurements were made at the end of the experiment.

The sample was loaded into an Orange ^{4}He-flow cryostat, which permitted investigations between 1.5K and 300K. The first incident energy chosen was E_i=40meV. This setting was selected for its dynamic $(E, |\mathbf{Q}|)$ range, which was expected to cover the region within which the gap was predicted to appear. While signs of temperature dependent behaviour was observed with this initial setting, the dynamic $(E, |\mathbf{Q}|)$ range was limited and information at lower $|\mathbf{Q}|$ and at higher energy was required. Incident energies of E_i=120meV and E_i=200meV were consequently chosen to resolve these issues. The former setting clearly revealed the features of interest while the latter setting, in comparison, provided lower energy-resolution data. Table 5.1 shows the chopper settings corresponding to the T_0 chopper, Fermi chopper 1 (FC_1) and Fermi chopper 2 (FC_2), which were utilized in order to produce neutrons of different initial energies. Measurements were made on the sample at a variety of temperatures between 100K and the lowest achievable temperature of 1.5K. Empty can data sets were also obtained at 100K and 1.5K for the two settings, E_i=120meV and E_i=40meV.

Table 5.1: Chopper settings for the experiment conducted on Ba_2YOsO_6

E_i (meV)	T_0(Hz)	FC_1(Hz)	FC_2(Hz)
40	90	180	60
120	180	300	60
200	120	360	180

5.3.2 Triple-axis Measurements

The data obtained from the measurements conducted at the N5 spectrometer were utilized for a careful determination of the critical exponent associated with the magnetic transition between the paramagnetic regime above T_N and the long-range ordered anti-ferromagnetic state below T_N. The following section provides an outline of the experiment conducted at N5 in order to obtain the information necessary for the determination of the critical exponent.

From the results which were previously obtained from SEQUOIA, the [100] and [110] magnetic Bragg peaks were found to develop below $\sim$ 70K at the positions $|\mathbf{Q}| = 0.75\text{Å}^{-1}$ and $|\mathbf{Q}| = 1.06\text{Å}^{-1}$, respectively. In this triple-axis experiment, the intensity of elastic scattering emanating from the [100] magnetic Bragg peak was measured as a function of temperature. This is equivalent to a measurement of the magnetic order parameter, and results obtained from these measurements can be utilized to extract the critical exponent, β. The intensity of neutrons scattered from a magnetic Bragg position at a temperature T is related to the critical exponent β by Equation (5.2).

$$I(T) = A\left(\frac{T_c - T}{T_c}\right)^{2\beta} + I_b \tag{5.2}$$

In this equation, A refers to the amplitude of the order parameter scattering, T_C is the critical (or Néel) temperature and I_b is the background contribution to the measured scattering intensity. The sample temperature T, is controlled in the experiment and I_b is estimated from the measured scattering intensity between 80K and 90K (i.e. well above the transition temperature). $I(T)$ is obtained by subtracting I_b from the measured neutron scattering intensity. The other parameters are determined by fitting the data set to Equation (5.2). The following discussion outlines the set-up of the experiment and procedure.

The 8g polycrystalline sample of Ba_2YOsO_6 that was measured on SEQUOIA was loaded into a flat aluminium cell of dimensions 50mm $\times$ 50mm $\times$ 2mm. The sample was sealed in He atmosphere with the use of indium wire, which was pre-soaked in a 10% solution of hydrochloric acid. This additional step removes the oxide layer which is formed when indium is regularly exposed to air, enhancing the bond between the indium wire and the aluminium cell. The sample was loaded into a 10K displex and the

sample axis was adjusted so that scattering from the position, $|\mathbf{Q}| = 0.745\text{Å}^{-1}$, was measured at the detector. Neutrons with wavelength $\lambda_i = 2.37\text{Å}$ were selected with the use of a pyrolytic graphite monochromator crystal. As this is a measurement of the intensity of scattering emanating from a magnetic Bragg peak, the final wavelength of the neutrons measured at the detector were also set to $\lambda_f = 2.37\text{Å}$ with the use of a pyrolytic graphite analyzer crystal. The collimation settings before and after the monochromator were set to 0° and 0.6°, respectively and the collimation settings before and after the analyzer were set to 0.55° and 2.4°, respectively. These collimation settings were used in order to obtain an energy resolution of ±1meV, providing good discrimination between elastic and inelastic scattering. A 2" pyrolytic graphite filter was used in the scattered side in order to avoid contamination from higher order neutrons. The 32-wire ^{3}He detector was centered on the [100] position and only the centre 12 wires were enabled. The measurements were taken in the following steps outlined below.

1. Before commencing the fine order parameter measurement, scans along $|\mathbf{Q}|$ in steps of 0.005Å^{-1} were made at a variety of temperatures between 6K and 85K. At each temperature, the [100] magnetic Bragg peak was fitted to ensure that there was no temperature dependence of the peak position.
2. The time taken for the sample to achieve a temperature stability of ±0.01K between changes in temperature of 0.2K was determined.
3. The elastic scattering intensity was measured as a function of temperature in 0.2K steps from 71K to 65K. Additional points were obtained at lower temperatures down to base temperature ($\sim$ 6K) in 5K steps.
4. To ensure reproducibility of the elastic scattering intensity versus temperature curve obtained in step 3, a sequence was set up to track the elastic scattering intensity as a function of temperature on warming from base temperature to 90K. These data points were made to interleave those obtained in step 3.

As this experiment involves frequent temperature changes, the interpretation of the data obtained from these measurements relies on a correct determination of the sample temperature. In order for the sample temperature to be accurately known, this measurement necessitates good temperature control and an awareness of the thermal gradients across the sample cell. The remainder of this discussion provides an outline of the determination of the sample temperature in this experiment. The sample

temperature was monitored with the use of three temperature sensors. Two of the sensors were placed on either end of the sample can and the third was located on the wall of the cryostat. To ensure good temperature stability at each measured temperature, data was obtained in ~ 4 minute sets over a period of ~ 1 hour. This permits careful tracking of sample temperature variations over time. The sample temperature was monitored primarily with the two temperature sensors located directly on the sample can. Once the temperatures recorded by each of the two sensors varied by no more than ± 0.01K over a ~ 16 minute period, the average of these two temperatures was used as the sample temperature. The temperature difference across the top and bottom of the 50mm sample can varied at most by 0.09K over the sample temperature range 65K to 70K.

5.4 Results and Discussion

To begin with, the elastic neutron scattering results shall be discussed. Figure 5.1 shows the results obtained from the measurements conducted at SEQUOIA at the setting, E_i=40meV. These curves were obtained by integrating $S(|\mathbf{Q}|, \omega)$ over the energy range E = ±1meV, at a variety of temperatures. Structural Bragg peaks are temperature independent so as long as there is no structural distortion which changes the symmetry of the crystal structure. As the crystallographic symmetry of Ba_2YOsO_6 is maintained down to 2K, these peaks can be identified as magnetic Bragg peaks which develop below 70K. These two magnetic Bragg peaks correspond to the [100] and [110] peaks, and occur at $|\mathbf{Q}| = 0.75\text{Å}^{-1}$ and $|\mathbf{Q}| = 1.06\text{Å}^{-1}$, respectively. These magnetic Bragg peaks are consistent with neutron diffraction measurements conducted by co-workers, who conducted measurements at the C2 spectrometer at the CNBC. The powder neutron diffraction pattern obtained from their measurements conducted on Ba_2YOsO_6 was identified with three-dimensional long-range order consistent with type-I anti-ferromagnetic ordering of the moments on the FCC lattice.

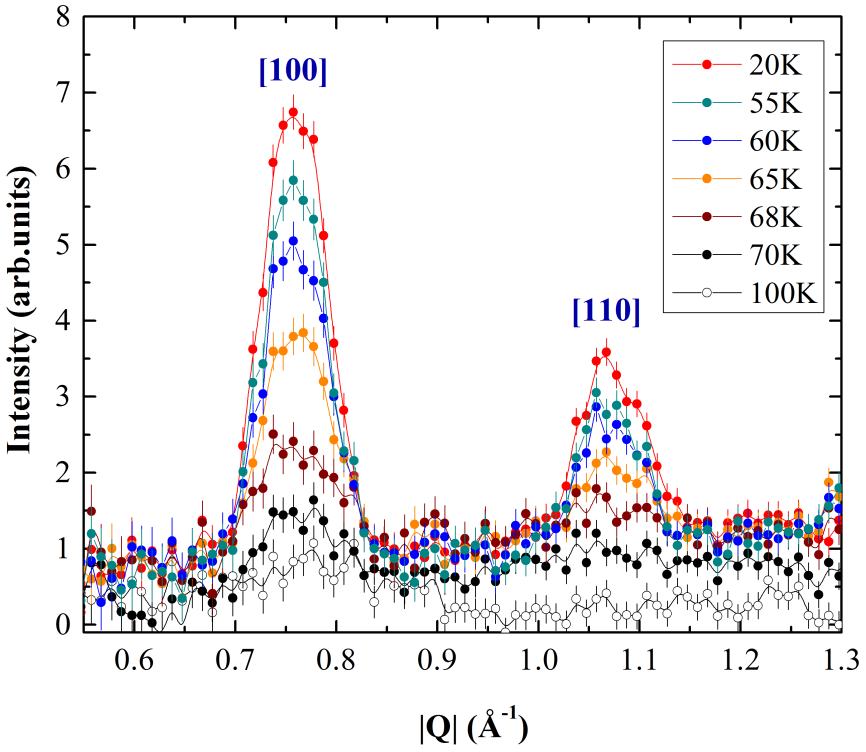

Figure 5.1: Temperature dependence of $|\mathbf{Q}|$ cuts obtained from the E_i=40meV data sets by integrating the scattering intensity within the energy range E = ±1meV.

A simple follow up experiment involves the measurement of the peak elastic scattering intensity at either of these magnetic Bragg peak positions as a function of temperature. From this measurement, the critical exponent β which describes the universality class of this system can be extracted. As previously outlined in Section 5.3.2, these measurements were conducted on Ba_2YOsO_6 at the [100] magnetic Bragg peak. Figure 5.2 shows the results obtained from these measurements made at the N5 spectrometer. While magnetization and Fisher heat capacity results reflect one transition temperature, the results from these triple-axis measurements provide evidence for the occurrence of a second, first order transition at a temperature $T_{C,2} = 67.5K$. This discontinuity, which is reproducible on both warming and cooling cyles, can be seen more clearly in a log-log plot of the data which is shown in Figure 5.3. If a fit is performed on the data set within the temperature range, $59.4 < T < 67.4K$, the data is not well described by the order parameter relation in Equation (5.2). As a result, the fit of the order parameter data was conducted in two separate temperature regimes corresponding to the ranges $59.4K < T < 67.4K$ and $67.5K < T < 69.2K$. The fits were performed according to the standard power-law function given by Equation (5.2) in these two temperature ranges. The background scattering intensity $I_b = 241$ was determined from an average of the scattering intensity measured in the temperature range $80K < T < 90K$. This avoids the region near to T_N where critical fluctuations are expected to contribute to the order parameter scattering intensity. The critical values corresponding to the two temperature ranges above and below $T_{C,2}$ were found to be $\beta_2 = 0.327(9)$ for $T < T_{C,2}$ and $\beta_1 = 0.30(3)$ for $T_{C,2} < T < T_{C,1}$. The significance here, is that the phase transition observed in Ba_2YOsO_6 cannot be described by a simple power-law form because of the presence of the discontinuity which occurs at $T_{C,2} = 67.5K$. The occurrence of this discontinuity is interpreted in terms of the existence of two separate phases which are separated by $T_{C,2} = 67.5K$. The critical values which were obtained from the fits to these two phase regions are those which are expected for the three-dimensional universality class.

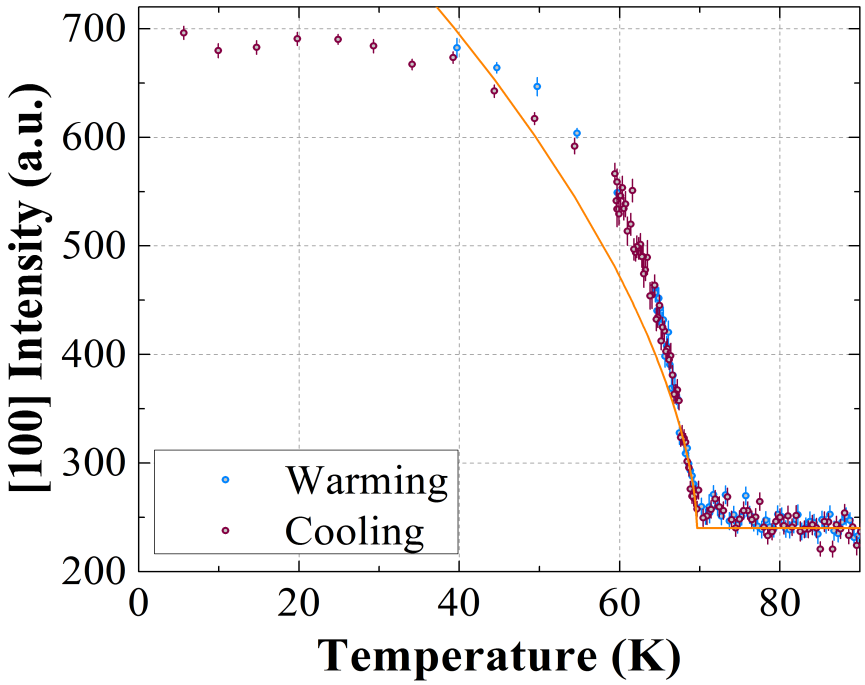

Figure 5.2: Evolution of the elastic scattering intensity from the [100] magnetic Bragg position in Ba_2YOsO_6 as a function of temperature.

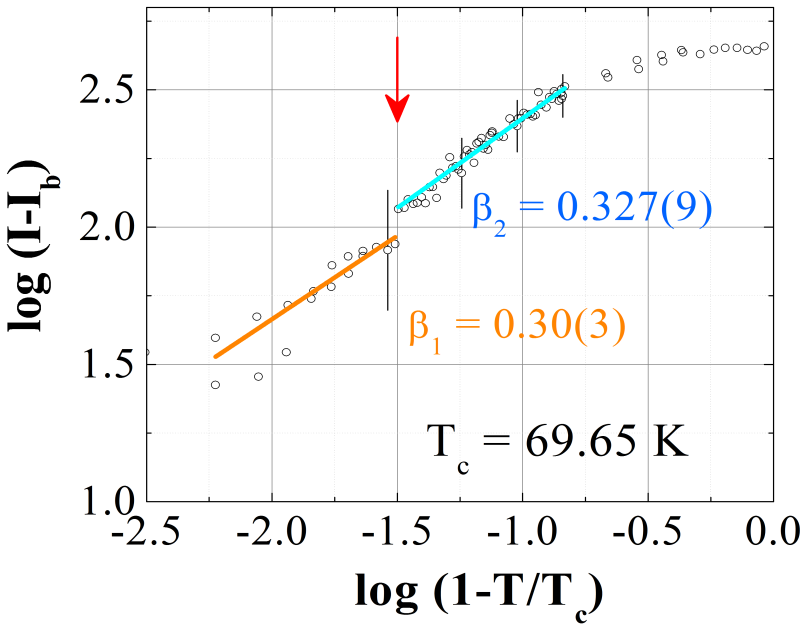

Figure 5.3: Log-log plot of the data presented in Figure 5.2.

Details on the development of the spin gap in this system can now be considered from the perspective of the inelastic neutron scattering results which were obtained from SEQUOIA. In Figure 5.4, $S(|\mathbf{Q}|, \omega)$ contour maps obtained from the E_i=40meV data sets are shown at a variety of temperatures. Diagrams (c)-(f) which represent the data sets obtained at T = 70K, 65K, 55K and 1.5K, respectively, are on the same intensity scale. Diagrams (a)-(b) show the T = 70K and 100K data sets on a different intensity scale, by virtue of the elevated scattering intensity observed at higher temperature. As can seen in Figure 5.4 (c), at T = 70K the system is in the paramagnetic regime and the quasi-elastic scattering is localized near the [100] Bragg position. As the temperature decreases below T_N, a gap of $\sim$ 17meV opens and is fully formed at 1.5K. This gap separates the elastic scattering from the inelastic magnetic scattering. The bandwidth of the inelastic magnetic scattering presumably arises from the dispersion of the spin-waves which are formed in the ordered state below T_N.

In order to properly quantify the details of the gap which forms below T_N, energy cuts obtained from the E_i=120meV data sets are compared at different temperatures, as shown in Figure 5.5 (a). The energy cuts are obtained by integrating $S(|\mathbf{Q}|, \omega)$ within the range $|\mathbf{Q}| = [0.5, 1.5]\text{Å}^{-1}$, which covers the position of the [100] magnetic Bragg position. Therefore, the evolution of the inelastic scattering within the gapped region defined by, 7 < E < 12meV, can be easily tracked as a function of temperature. Upon cooling from 70K, the scattering within the gapped region decreases and is transferred to higher energy, contributing to the gapped and dispersive, inelastic spin excitation. The 1.5K energy cut was fit with two Gaussians and a linear background in order to determine the size of the gap and bandwidth of the spin excitations. The two Gaussians were centred on the elastic position and the inelastic excitation, and the linear background was used to account for any excess background scattering from phonons, for example. The centre position and the full-width-half-maximum of the Gaussian centred on the inelastic excitation correspond to the size of the gap and the bandwith of spin excitations, respectively. From the fit, the inelastic excitation is characterized by a gap of size $\Delta = 18(2)$meV and a bandwidth of 15(5)meV.

The $|\mathbf{Q}|$ cuts shown in Figure 5.5 (b) were obtained from the E_i=40meV data sets by integrating $S(|\mathbf{Q}|, \omega)$ in the range (E = [6, 8]meV). In these $|\mathbf{Q}|$ cuts, the T=1.5K data set was utilized as a background since weak scattering is expected within the gap at this temperature. Consequently, the evolution of the scattering intensity within the spin gap can also be followed as a function of temperature. It can be seen directly

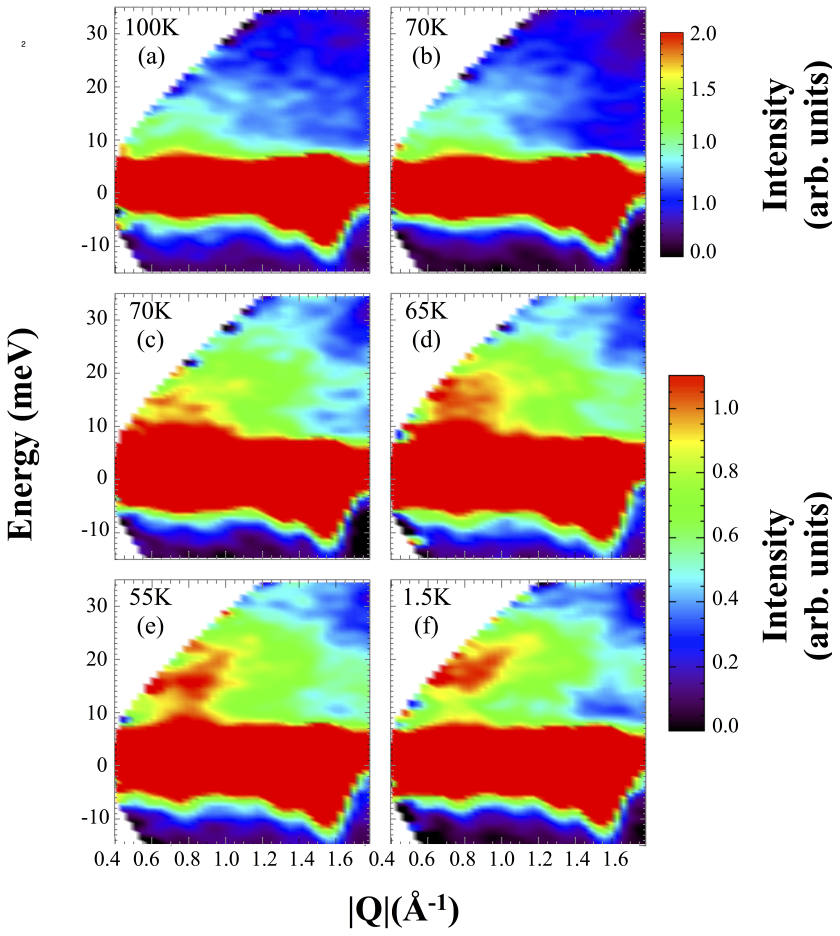

Figure 5.4: Temperature dependence of $S(\mathbf{Q}, \omega)$ contour maps obtained at E_i=40meV on Ba_2YOsO_6 .

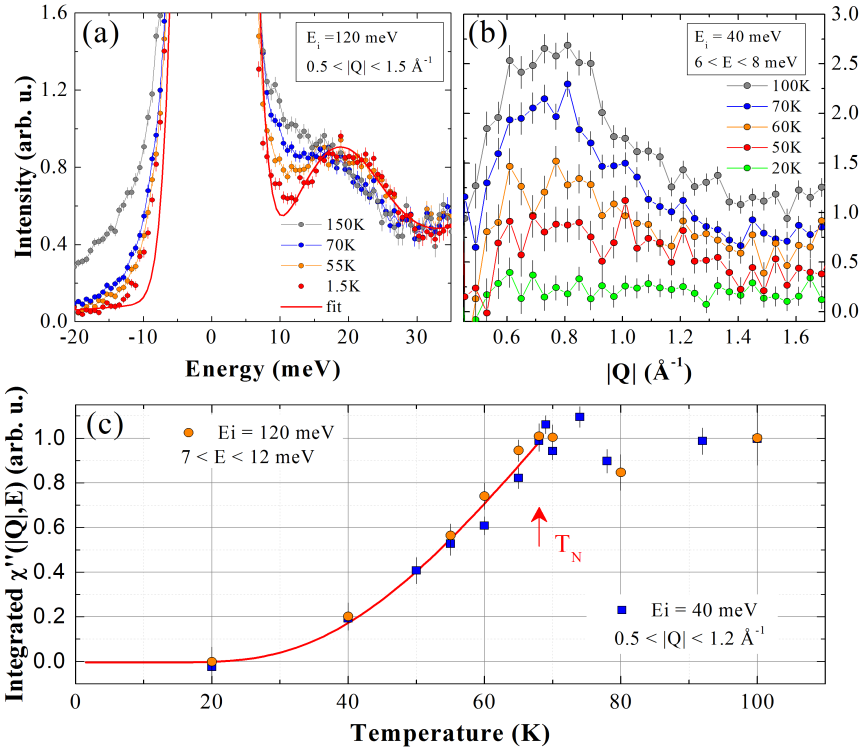

Figure 5.5: (a) Temperature dependence of $|\mathbf{Q}|$ integrated cuts performed on the E_i=120meV data sets in the range $|\mathbf{Q}|$=[0.5,1.5]Å^{-1}. (b) Temperature dependence of energy integrated cuts performed on the E_i=40meV data sets in the range E=[6,8]meV. (c) Temperature dependence of full integrated intensities obtained from the E_i= 40meV and 120meV data sets.

that the energy integrated scattering intensity within the gap decreases as a function of temperature near the [100] magnetic Bragg position. This directly shows that the gap develops below T_N by the transfer of scattering intensity from the quasi-elastic region to the inelastic spin excitation. Utilizing this information, an analysis can be done from the point of view of the dynamic susceptibility $\chi''(\mathbf{Q}, \mathrm{E})$. It is defined as a function of the dynamic structure factor $\Delta \mathrm{S}(\mathbf{Q}, \mathrm{E})$ and a temperature weight factor as given by Equation (5.3).

$$\Delta S(\boldsymbol{Q}, E) = \frac{\chi''(\boldsymbol{Q}, E)}{1 - \exp\{-\frac{E}{k_B T}\}} \tag{5.3}$$

$\chi''(\mathbf{Q}, \mathrm{E})$ can therefore be determined from the energy and $|\mathbf{Q}|$ integrated cuts by utilizing the relation given in Equation (5.3). By integrating the energy cuts in the range $\mathrm{E} = [7, 12]$meV, and the $|\mathbf{Q}|$ cuts in the range $|\mathbf{Q}| = [0.5, 1.5]\text{Å}^{-1}$, the temperature dependence of the integrated intensities can be directly compared as shown in Figure 5.5 (c). As expected, the integrated intensity rapidly increases in the temperature range $20\mathrm{K} < \mathrm{T} < \mathrm{T_N}$ and plateaus above $\mathrm{T_N}$. Since these two results were obtained at different E_i settings and are consistent, the evolution of the scattering intensity is related to the development of a long-range ordered anti-ferromagnetic state in Ba_2YOsO_6 below T_N.

5.5 Conclusions

Magnetization and Fisher heat capacity results show evidence for a single transition temperature in Ba_2YOsO_6 . However, triple-axis measurements performed at the N5 spectrometer provide evidence for the occurrence of two transitions to two states resembling a Type I FCC anti-ferromagnetic ordering. Evidence for a second, weak, first-order transition was found to occur at $T_{C,2} = 67.5K$.

A gap was also found to occur in Ba_2YOsO_6 as has been reported in the 4d analogue, Ba_2YRuO_6 [1]. This effect is attributed to strong spin-orbit effects in the two systems, which tend to induce some anistropy. A spin gap of size $\sim 17meV$ is observed for Ba_2YOsO_6 and is larger than the gap size which was reported in the case of Ba_2YRuO_6 ($\sim 3.4meV$). The gap size in the former case is roughly 3.4 times the size of the gap which was reported for Ba_2YRuO_6 [1]. The ratio between these gap sizes is approximately, the ratio between the free-ion spin-orbit coupling constants, $\frac{\lambda_{Os}}{\lambda_{Ru}} = \frac{186}{55} \sim 3.3$. This could then suggest that spin-orbit coupling is indeed responsible for the development of a spin gap in each of these systems. The cubic symmetry seems to be another key ingredient in the observation of this phenomenon. In another study conducted by Aczel *et al.*, two quasi FFC double perovskites $La_2NaB'O_6(B' = Ru, Os)$ were studied [7]. Significantly, it was found that the ruthenate develops a gap, while the osmate does not fully develop a gap. In the case of these two compounds, it appears that the lack of cubic symmetry suppresses the development of the gap in La_2NaOsO_6. However, the full details of the dynamics in these systems are not yet fully understood.

Bibliography

[1] J.P. Carlo, J.P. Clancy, K. Fritsch, C.A. Marjerrison, G.E. Granroth, J.E. Greedan, H.A. Dabkowska, and B.D. Gaulin. *Phys. Rev. B*, 88(024418), 2013.

[2] T. Aharen, J.E. Greedan, F. Ning, T. Imai, V.K. Michaelis, S. Kroeker, H. Zhou, C.R. Wiebe, and L.M.D. Cranswick. *Phys. Rev. B*, 80(134423), 2009.

[3] T. Aharen, J.E. Greedan, C.A Bridges, A.A. Aczel, J. Rodriguez, G. MacDougall, G.M. Luke, T. Imai, V.K. Michaelis, S. Kroeker, H. Zhou, C.R. Wiebe, and L.M.D. Cranswick. *Phys. Rev. B*, 81(224409), 2010.

[4] T. Aharen, J.E. Greedan, C.A Bridges, A.A. Aczel, J. Rodriguez, G. MacDougall, G.M. Luke, V.K. Michaelis, S. Kroeker, C.R. Wiebe, H. Zhou, and L.M.D. Cranswick. *Phys. Rev. B*, 81(064436), 2010.

[5] E. Granado, J.W. Lynn, R.F. Jardim, and M.S. Torikachvili. *Phys. Rev. Lett.*, 110(017202), 2013.

[6] P.D. Battle and C.W. Jones. *J. Solid State Chem.*, 78:108–116, 1989.

[7] A.A. Aczel, P.J. Baker, D.E. Bugaris, J. Yeon, H.-C. zur Loye, T. Guidi, and D.T. Adroja. *Phys. Rev. Lett.*, 112:117603, 2014.

Chapter 6

Conclusions

In this thesis, results from neutron scattering measurements conducted on the two frustrated magnets, Ba_2YOsO_6 and $Yb_2Ti_2O_7$, were presented. The novel behaviour, reported in the former system is attributed to the interplay of frustration and strong spin-orbit effects. The magnetic ground state of $Yb_2Ti_2O_7$ however, has remained an enigma, with previous studies incompatibly describing the low temperature properties of this system. The crystal-field (CF) investigation performed on two samples of $Yb_2Ti_{2-x}Yb_xO_{7-\frac{x}{2}}$ (x=0 and 0.046) are intended to address the effect of sample variability on the nature of the magnetic ground state observed in $Yb_2Ti_2O_7$.

In Chapter 4, results from the measurement of the crystal-field (CF) spectrum of a powder sample and crushed single-crystal (CSC) sample of $Yb_2Ti_{2-x}Yb_xO_{7-\frac{x}{2}}$, characterized by x=0 and x=0.046, respectively, were presented. The three doublet excitations expected in $Yb_2Ti_2O_7$ were clearly visible from the measured INS spectra of the two samples. The measurements conducted on the powder sample permitted the unambiguous determination of the ground state wave function of the Yb^{3+} ion in $Yb_2Ti_2O_7$, the components of the g-tensor and the CF parameters which describe the CF Hamiltonian, $\mathcal{H}_{CF}$. This is the first time that the CF parameters of $Yb_2Ti_2O_7$ were determined from a direct measurement of the CF levels with the use of the inelastic neutron scattering (INS) technique. To our best knowledge, the parameters determined from this study are best suited, from the available literature, to describing the CF spectrum measured for $Yb_2Ti_2O_7$. In addition, the spectra obtained for the powder and CSC samples were compared to determine how strongly sample variations which result from single-growth processes affect the low temperature properties of $Yb_2Ti_2O_7$. One surprising result was that the CF associated with the *A*-site Yb^{3+} ions are significantly

broadened due to a small ($\sim$2%) excess of Yb^{3+} ions in $Yb_2Ti_2O_7$. Another intriguing feature that was observed in the CSC sample was the presence of an excitation mode at $\sim$ 40meV, which is enhanced with decreasing temperature. The origin of this excitation is not yet understood but one preliminary guess is that this feature is a CF excitation of the Yb^{3+} ions on the B-site.

Chapter 5 was focussed on elastic and inelastic neutron scattering measurements which were conducted on the $5d^3$ double perovskite, Ba_2YOsO_6. The INS measurements which were conducted at SEQUOIA, at the Spallation Neutron Source, showed the development of a gap below $T_N \sim 70K$, which is associated with the development of a long-range ordered state. Significantly, a gap is not expected for an orbitally quenched $s = \frac{3}{2}$ spin-only moment because anisotropy is minimized. This result has been attributed to strong spin-orbit effects, which arise from the presence of the heavy magnetic 5d Os^{5+} ion. Elastic, triple-axis measurements which were conducted at the N5 spectrometer, at the Canadian Neutron Beam Centre, on Ba_2YOsO_6 were also reported. These measurements were performed in order to determine the critical exponent which is associated with the magnetic transition which occurs at $\sim$ 70K. These results provided evidence for the existence of a continuous transition at $T_N = 69.4K$ and a discontinuous transition at $T_{C,2} = 67.5K$. The results from subsequent analysis are interpreted in terms of the development of two, three-dimensional long-range ordered phases in Ba_2YOsO_6.